UCLA
UCLA Electronic Theses and Dissertations

Title
Multi-Scale Modeling and Simulations for Materials Phenomena

Permalink
https://escholarship.org/uc/item/9386x608

Author
Huang, Shu

Publication Date
2022

Peer reviewed|Thesis/dissertation

UNIVERSITY OF CALIFORNIA

Los Angeles

Multi-Scale Modeling and Simulations

for Materials Phenomena

A dissertation submitted in partial satisfaction

of the requirements for the degree

Doctor of Philosophy in Materials Science And Engineering

by

Shu Huang

2022

ABSTRACT OF THE DISSERTATION

Multi-Scale Modeling and Simulations

for Materials Phenomena

by

Shu Huang

Doctor of Philosophy in Materials Science And Engineering

University of California, Los Angeles, 2022

Professor Jaime Marian, Chair

Multi-scale modeling has been growing rapidly from the descriptive to predictive functions and employing modeling and simulations has become a crucial mission of science that helps to deliver an uninterrupted growth of the modern society. Here we integrated modeling works on different levels of scale regarding four different material behaviors, with each illustrated in a chapter. They are ordered as atomic scale modeling, oxidation kinetics modeling for tungsten, reaction rates for 1D motion particles(verified with Kinetic Monte Carlo) and modeling work on the non-monotonic strain response of nanoporous multiferroic composites with Finite Element Method.

We used Density Functional Theory(DFT) to obtain different kinds of intrinsic material parameters based on the calculations of the electronic configuration of a system, part of which is then used in the oxidation model for pure tungsten.

In the oxidation numerical model, we predict oxide scale growth on tungsten surfaces under exposure to oxygen at high temperatures. The model captures the formation of four thermodynamically-compatible oxide sublayers, WO_2, $WO_{2.72}$, $WO_{2.9}$, and WO_3, on top

of the metal substrate. Oxide layer growth is simulated by tracking the oxide/oxide and oxide/metal interfaces using a sharp-interface *Stefan* model coupled to diffusion kinetics. We simulate oxide growth at temperatures of 600°C and above, where we find deviation from classical parabolic growth in several cases. A comparison of the model predictions with an extensive experimental data set, shows reasonable agreement at most temperatures.

Our development of reaction rate for 1d motion particle was initiated due to the asymmetry in diffusion dimensionality between self-interstitial atom (SIA) clusters and vacancies is a fundamental feature of irradiation damage in crystals. While SIA clusters perform one-dimensional motion along mostly rectilinear trajectories, a complete set of kinetic coefficients, including coagulation reaction rates and sink strengths, does not exist for 1D-moving objects. We derive analytical expressions for these coefficients from continuum diffusion theory particularized to 1D motion and carry out kinetic Monte Carlo simulations of numerical replicas of the geometry of diffusing particles and sinks to validate the proposed solutions. Our simulations, which are conducted entirely independently from the analytical derivations, reveal excellent agreement with the proposed expressions, adding confidence to their validity. We compare the 1D and 3D cases and discuss their relevance for kinetic codes for damage accumulation calculations.

In the work that uses Finite Element Method (FEM) to study the non-monotonic strain response of nanoporous multiferroic composites under electric field control, we simulate and analyze the mechanical response of a class of multiferroic materials consisting of a templated porous nanostructure made out of cobalt ferrite (CFO) partially filled by atomic layer deposition (ALD) with a ferroelectric phase of lead zirconate titanate (PZT). Our numerical results show that the non-monotonic mechanical response's causes e.g. The increase of the strain due to a reduced system stiffness; And a larger mass fraction of PZT due to decreased porosity. A nonlinear piezoelectric response for PZT leads to an improved agreement with the experimental data, consistent with *ex* situ poling of the nanostructure prior to magnetic measurements.

The dissertation of Shu Huang is approved.

Mathieu Bauchy

Amartya Sankar Banerjee

Ali Mosleh

Jaime Marian, Committee Chair

University of California, Los Angeles

2022

Dedicated to my parents,

Wenyu Wang and Weiguo Huang,

for their unconditional support and love.

TABLE OF CONTENTS

LIST OF FIGURES

x

LIST OF TABLES

ACKNOWLEDGMENTS

I would like to thank my advisor, my fellows and the professors who provided help.

It is a wonderful luck to work with my advisor Professor Jaime Marian all these past years. You pass on knowledge selfless and cultivate a student like me in all possible ways, which has been such a blessing for me. You established high standard of persistence, intelligence, kindness and caring for people, and will leave me a life-long influence.

Thanks to my friends who provided support during the hardest time and enabled me to look at the bright side of everything; I take the friendship as valuable sediments which thickened my life.

Thanks to my committee members, Professor Ali Mosleh, Professor Mathieu Bauchy and Professor Amartya Banerjee. Your encouragement and thoughtful feedback always lights up the direction ahead.

VITA

2016   M.S. (Materials Engineering), University of Southern California.

2014   B.S. (Applied Physics), Hefei University of Technology.

PUBLICATIONS

Huang, S., & Marian, J. (2019). Rates of diffusion controlled reactions for one-dimensionally-moving species in 3D space. *Philosophical Magazine*, 99(20), 2562-2583.

Huang, S., Karaba, C. T., Patel, S. K., Neal, A., Tolbert, S. H., & Marian, J. (2022). Simulating the non-monotonic strain response of nanoporous multiferroic composites under electric field control. *Applied Physics Letters*, 120(21), 213501.

Nathaniel, J. E., El-Atwani, O., Huang, S., Marian, J., Leff, A. C., Baldwin, J. K., ... & Taheri, M. L. (2022). Implications of Microstructure in Helium-Implanted Nanocrystalline Metals. *Materials*, 15(12), 4092.

Zhao, Y., Zhu, P., Huang, S. et al (2020). Molecular interaction regulates the performance and longevity of defect passivation for metal halide perovskite solar cells. *Journal of the American Chemical Society*, 142(47), 20071-20079.

Jacobs, M., Zhou, X., Olivera, E., Sheil, R., Huang, S., ... & Marian, J. (2021). Room

temperature rectification in tapered-channel thermal diodes through nanoscale confinement-induced liquid-solid phase change. *Journal of Applied Physics*, 129(7), 075103.

Zhao, Y., Zhu, P., Wang, M., Huang, S. et al (2020). A polymerization?assisted grain growth strategy for efficient and stable perovskite solar cells. *Advanced Materials*, 32(17), 1907769.

CHAPTER 1

Background

1.1   Multiscale Material Modeling

Our daily life is presented by all materials based phenomena that can span a broad order of length and time scale levels. Materials science which integrates physics and chemistry, describes and explains different materials phenomena, in which multi-scale modeling methods are developed to acquire material properties at different level of scale through simulations and calculations. On each level, a material system is described by particular approaches, and the different scales can be seen in Figure 3.2.3 [3]. As the field of multi-scale material modeling is growing rapidly with continuously increasing computing power and maturer use of numerical methods for materials science, the description, understanding and prediction made to a material system with modeling and simulations has become a vital scientific task that protects the welfare of the currently on-going society.

The approaches to study material behaviors bridging across nano-scale to continuum-scale and examples can be at various scales in an ascending order like: quantum mechanical models (electrons structure calculation, e.g. DFT), molecular dynamics models (calculation about individual atoms or molecules), rate/field theory, kinetic models, continuum models (Finite Element Method, etc.), device models and so on. Each scale will best describe a corresponding a situation with a specific window of length and time. Multi-scale modeling has shown its indispensable importance in materials engineering since it integrates computational power and allows the prediction of material properties or behavior with the most
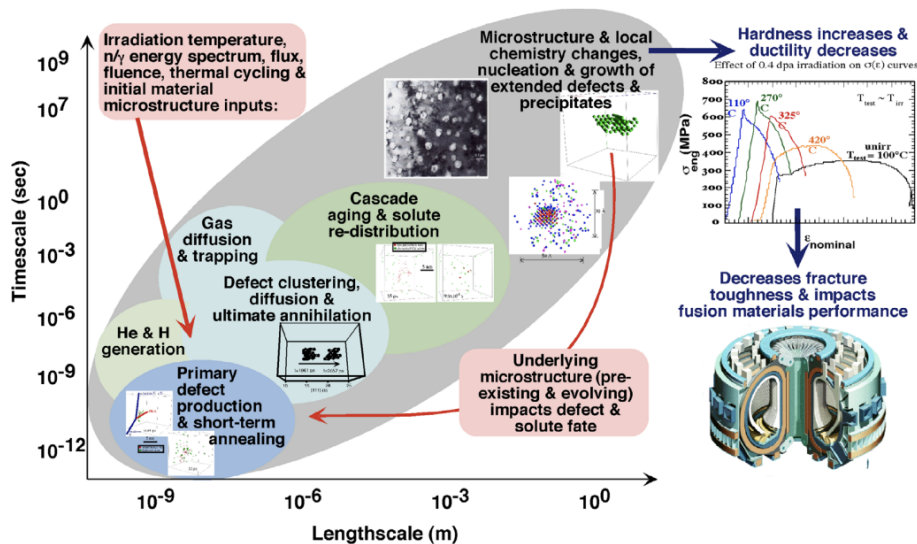
Figure 1.1: Schematic diagram showing the multi-scale nature of microstructural evolution in fusion structural materials.[3]

import mechanism seized while the cost is reduced tremendous compared with experimental approaches.

This thesis addressed material topics from atomic to centimeter scale begin with atomic scale *ab inito* calculations in Chapter 2; Chapter 3 demonstrates the kinetic model which is used to mimic the oxidation process for pure tungsten with 5 different phases integrated. Chapter 4 talks about the development of the analytical expression of 1d motion defect and Kinetic Monte Carlo simulations as the proof. Lastly Chapter 5 introduced a study on the non-monotonic strain response of nanoporous multiferroic composites under electric field control of the using Finite Element Method(FEM). We introduced the minimum scale model which is *ab initio* calculations on atomic scale in Chapter 2. While this regime can cover many-body electronic structure theory, density functional theory(DFT), quantum chemistry and so on, what we used here is DFT method. It's based on the first principle of physics and provide approaches to fetch properties that are related to the stoichiometric attributes of a material, which could be the fundamental bricks of a system. In this Chapter we focused on

the calculation of the diffusion properties of an oxygen vacancy in a WO_2 system, which are then put to use in the kinetic model for the oxidation process of pure tungsten described in Chapter 3.

To study the oxidation process of tungsten, we present a numerical model to predict oxide scale growth on tungsten surfaces under exposure to oxygen at high temperatures. The model captures the formation of four thermodynamically-compatible oxide sublayers, WO_2, $WO_{2.72}$, $WO_{2.9}$, and WO_3, on top of the metal substrate. Oxide layer growth is simulated by tracking the oxide/oxide and oxide/metal interfaces using a sharp-interface *Stefan* model coupled to diffusion kinetics. The model is parameterized using selected experimental measurements and electronic structure calculations of the diffusivities of all the oxide subphases involved. We simulate oxide growth at temperatures of 600°C and above, extracting the power law growth exponents in each case, which we find to deviate from classical parabolic growth in several cases. We conduct a comparison of the model predictions with an extensive experimental data set, with reasonable agreement at most temperatures.

Among various research works to study the mechanism of material phenomena, we are especially interested in the damage and failure of nuclear materials for its irreplaceable utility to provide energy to mankind, for which investigations have been conducted[1, 2, 4, 5, 6]. We particularly are interested in the of first wall materials behaviors, the oxidation of tungsten , which is the candidate of plasma facing material, has been articulated in Chapter 3, and the 1D motion pattern of defects in the first wall materials can seen Chapter 4, Our development of reaction rate for 1d motion particle was initiated due to the asymmetry in diffusion dimensionality between self-interstitial atom (SIA) clusters and vacancies which is a fundamental feature of irradiation damage in crystals, leading to a defect buildup imbalance that manifests itself as measurable dimensional and mechanical property changes. It is well known that, while vacancies and mobile vacancy clusters diffuse in a three-dimensional (3D) fashion, SIA clusters perform one-dimensional motion along mostly rectilinear trajectories. Despite this, a complete set of kinetic coefficients, including coagulation reaction rates

3

and sink strengths, does not exist for 1D-moving objects. We derive analytical expressions for these coefficients from continuum diffusion theory particularized to 1D motion. Moreover, we carry out kinetic Monte Carlo simulations of numerical replicas of the geometry of diffusing particles and sinks to validate the proposed solutions. The FEM(Finite Element Method) work on the non-monotonic strain response of nanoporous multiferroic composites under electric field control, we simulate and analyze the mechanical response of a class of multiferroic materials consisting of a templated porous nanostructure made out of cobalt ferrite (CFO) partially filled by atomic layer deposition (ALD) with a ferroelectric phase of lead zirconate titanate (PZT). We apply finite element modeling to the smallest repeatable unit of the nanoporous template and find that this non-monotonic mechanical response is caused by the interplay between two driving forces: First, increased porosity works towards increasing the strain due to a reduced system stiffness. Second, decreased porosity involves a larger mass fraction of PZT, which drives the electro-mechanical response of the structure, thus leading to a larger strain.

1.2 References

[1] Asghar Aryanfar, John Thomas, Anton Van der Ven, Donghua Xu, Mostafa Youssef, Jing Yang, Bilge Yildiz, and Jaime Marian. Integrated computational modeling of water side corrosion in zirconium metal clad under nominal lwr operating conditions. *Jom*, 68 (11):2900–2911, 2016.

[2] Kevin G Field, Mingren Shen, Caleb P Massey, Kenneth C Littrell, and Dane D Morgan. Rapid characterization methods for accelerated innovation for nuclear fuel cladding. *Microscopy and Microanalysis*, 26(S2):868–869, 2020.

[3] J Marian, CS Becquart, C Domain, SL Dudarev, MR Gilbert, RJ Kurtz, DR Mason, K Nordlund, AE Sand, LL Snead, et al. Recent advances in computational materials modeling of tungsten as plasma-facing material for fusion energy applications. *Nucl. Fusion*, 57(9):092008, 2017.

[4] Michael Reyes, Asghar Aryanfar, Sun Woong Baek, and Jaime Marian. Multilayer interface tracking model of zirconium clad oxidation. *Journal of Nuclear Materials*, 509: 550–565, 2018.

[5] Mingren Shen, Guanzhao Li, Dongxia Wu, Yudai Yaguchi, Jack C Haley, Kevin G Field, and Dane Morgan. A deep learning based automatic defect analysis framework for in-situ tem ion irradiations. *Computational Materials Science*, 197:110560, 2021.

[6] BD Wirth, GR Odette, J Marian, L Ventelon, JA Young-Vandersall, and LA Zepeda-Ruiz. Multiscale modeling of radiation damage in fe-based alloys in the fusion environment. *Journal of nuclear materials*, 329:103–111, 2004.

CHAPTER 2

Atomic Scale Modelling

2.1   Model for DFT calculation

Schrödinger′s wave function is extremely promising, as it contains all of the information available to describe a system.

$$\hat{H}\Psi = E\Psi \tag{2.1}$$

In a system of a specific configuration of atoms, the Hamiltonian would contain the kinetic energy from electrons, nuclei, and potential energy from the interaction of electrons to electrons, nuclei to nuclei, and electrons to nuclei:

$$\hat{H} = -\frac{\hbar^2}{2m}\sum_i^n \nabla_i^2 - \frac{\hbar^2}{2M}\sum_i^N \nabla_A^2 - \sum_i^n \sum_j^N \frac{Z_j e^2}{|R_j - r_i|} + \frac{1}{2}\sum_i^n \sum_{\substack{j \\ j \neq i}}^N \frac{e^2}{|r_j - r_i|} + \frac{1}{2}\sum_i^M \sum_{\substack{j \\ j \neq i}}^N \frac{Z_i Z_j}{|R_j - R_i|} \tag{2.2}$$

Born - Oppenheimer (B-O) approximation proved that the mass of a nuclear M is at least 3 orders heavier than the mass of an electron m, the motion of nuclei is negligible, and the interaction of nuclei to nuclei will be a constant. So both of them can be dropped, thus we get Equation2.3. Born is the one who gave now-standard interpretation of the probability density function for $\psi^*\psi$ in the Schrösdinger equation, for which he was awarded the Nobel Prize in 1954. $\psi^*\psi$ is the probability of finding an electron at the corresponding position. And Oppenheimer is known as "father of the atomic bomb".

$$\hat{H} = -\frac{\hbar^2}{2m} \sum_i^n \nabla_i^2 - \sum_i^n \sum_j^N \frac{Z_j e^2}{|R_j - r_i|} + \frac{1}{2} \sum_i^n \sum_{\substack{j \\ j \neq i}}^N \frac{e^2}{|r_j - r_i|} \tag{2.3}$$

While many body problem is prohibitively hard to solve, we want to avoid this. We now think about using electron density instead of these point electrons. The Hartree-Fock Approximation gives: the i_{th} electron is treated as a single electron moving in the mean field created by all the other electrons, as shown in Equation 2.5, and a product of single-electron wave functions like this is called Hartree product.

$$\Psi(\boldsymbol{r_1}, ... \boldsymbol{r_N},) = \psi(\boldsymbol{r_1}), \psi(\boldsymbol{r_2}), ... \psi(\boldsymbol{r_N}) \tag{2.4}$$

Hence the electron density can be

$$n(\boldsymbol{r}) = 2 \sum_i \psi(\boldsymbol{r})^* \psi(\boldsymbol{r}) \tag{2.5}$$

which sums over all the probabilities that an electron in the individual electron wave function $\psi_i(\boldsymbol{r})$, the factor 2 comes from "electron spin". Two theories then finally help to produce the ultimate form of DFT equation:

- Theory 1: The ground-state energy is a unique functional of electron density, by Hohenberg and Kohn (1964).

- Theory 2: The electron density that minimizes the energy of the overall functional is true ground state electron density, by Kohn and Sham (1965)

Instead of finding out the wave function, we can just deal with the density, and the 1st theorem here tells people the density contains information as much as the wave function. And the expression for DFT is given as:

$$E[\{\psi_i\}] = -\frac{\hbar^2}{2m} \sum_i^n \int \psi_i^* \nabla_i^2 \psi_i d^3 r$$
$$+ \int V_{ext}(r) n(r) d^3 r + \frac{1}{2} \int \frac{n(r)n(r')}{|r - r'|} d^3 r d^3 r' + E_{xc}[n(r)]$$

where electron density is $n(r) = s \sum_i^n |\psi_i(r)|^2$, $\psi_i(r)$ is the wave function of electron i, $V_{ext}(r)$ is the potential electrons feel from nuclei and $E_{xc}[n(r)]$ is the exchange-correlation energy which can be LDA(local density approximation) or GGA(general gradient approximation) depending on the choice.

2.2 Electronic structure calculations for Oxygen Vancancy

2.2.1 DFT+U method

The use of the DFT+U technique is necessary to reach a correct description of the electronic configuration of tungsten, which is critical to calculate formation energies and migration energy barriers [10]. Tungsten is a transition metal with electron configuration $[Xe]4f^{14}5d^46s^2$, i.e., a partially filled d orbital that requires special DFT treatments [8].

When applying a one-electron method with an orbital-independent potential to transition metal compounds, one has as a result a partially filled d band with metallic type electronic structure and itinerant d electrons. This is definitely the wrong model for late-transition-metal oxides and rare-earth metal compounds where d (f) electrons are well localized and there is a sizable energy separation between occupied and unoccupied sub-bands (the lower Hubbard band and upper Hubbard band in a model Hamiltonian approach [1]). LDA/GGA functionals describe poorly the electronic properties of these localized orbitals and that is where DFT+U technique comes in. DFT+U accounts for electron-electron interactions in strongly correlated materials because the self-interaction error is dominant in d and f states.

DFT+U is based on Hubbard model, which solves the energy of electron correlation introduced or Coulomb repulsion between electrons at the same atomic orbitals [3]. The Hubbard model explains the transition between the insulation and conduction features of the systems with strong on-site repulsion using the following Hamiltonian:

$$H_{\text{H}ub} = t \sum_{\langle i,j \rangle,\ \sigma} c^\dagger_{i,\sigma} c_{j,\sigma} + U \sum_i n_{i\uparrow} n_{i\downarrow} \tag{2.6}$$

The Hubbard Hamiltonian has two components, namely, the hopping integral t and the electron repulsion strength U. $c_{i,\sigma}^{\dagger}$ and $c_{j,\sigma}$ are the creation and annihilation operators of electron state at sites i and j and spin σ, respectively. The sum runs over all $\langle i,j \rangle$ nearest electron pairs, i and j. $n_i = n_{i\uparrow} + n_{i\downarrow}$ is the total density operator at site i.

The Hubbard model allows us to write the total energy of the system as a standard DFT energy plus a term representing the strong correlation of the electronic states in d (and f) orbitals.

$$E_{\mathrm{D}FT} + U[n] = E_{\mathrm{D}FT}[n] + E_{\mathrm{H}ub}[n_i^{\sigma}] - E_{\mathrm{dc}}[n_i^{\sigma}] \tag{2.7}$$

where $U[n]$ is the correction induced by DFT+U method, $E_{\mathrm{H}ub}[n_i^{\sigma}]$ is the Hubbard functional that describes the correlated states, and n_i^{σ} is the occupation number of the localized orbitals with the spin of σ and site i. The term of $E_{\mathrm{dc}}[n_i^{\sigma}]$ is a 'double counting' term, which is included because when we additively append the Hubbard term $E_{\mathrm{H}ub}[n_i^{\sigma}]$, the energy contribution of the related orbitals has already been counted in the DFT term. In our calculations we use a Coulomb interaction parameter of `LDAUU`=1.82 eV for pure metal W [2] because it does not affect the distribution of electrons for the attempt frequency calculations. However, we have also repeated the calculations with a value of `LDAUU`=6.2 eV used for WO_3 [4] and found only a change of 5% in the migration energy barriers.

2.3   DFT calculations of O diffusivity in WO_2

Tungsten is a transition metal with partially-filled d orbitals that requires special DFT treatments. Here we use the DFT+U technique with the parameterization for W used by Feng et al. [2]. The generalized gradient approximation (GGA) and Perdew-Burke-Ernzerhof (PBE) was applied to build the pseudopotential of the system and the frozen-core convention was implemented with the projector-augmented wave (PAW) method. The DFT simulations are performed with a cutoff energy of 600 eV and a k-point sampling of 2×2×4. The

convergence criterion for the energy relaxation of the atomic positions was set to be 10^{-5} eV. Defect energies were calculated in a WO_2 supercell containing 36 atoms under constant volume.

2.3.1 Formation energy, E_f^V

The calculations are based on supercells of $W_N O_{2N}$ lattices, where N is the number of W atoms. A vacancy is created by removing an O atom from a lattice position and placing it at infinity, i.e.:

$$E_f^V = E_{W_N O_{2N-1}} + \mu_O - E_{W_N O_{2N}}, \tag{2.8}$$

where $E_{W_N O_{2N-1}}$ and $E_{W_N O_{2N}}$ are the energy of the supercells with and without a vacancy, and μ_O is the chemical potential of an isolated oxygen atom. Under low oxygen partial pressures, μ_O satisfies:

$$\mu_O = \mu_{O_2} + \frac{1}{2} E_{WO_2}^f \tag{2.9}$$

where μ_{O_2} is the chemical potential of bimolecular oxygen and $E_{WO_2}^f$ is the formation energy of tungsten dioxide. For its part, $E_{WO_2}^f$ is given by:

$$E_{WO_2}^f = \mu_{WO_2} - \mu_{O_2} - \mu_W$$

where the r.h.s. of the equation contains the chemical potentials (energy per molecule) of the perfect WO_2 crystal, bimolecular oxygen, and pure (metal) W. After carrying out the pertinent DFT calculations, we arrive at values of $\mu_O = -7.65$ eV and $E_f^V = 2.49$ eV. It must be kept in mind, however, that measurable concentrations of vacancies have been detected in tungsten oxide under ambient conditions [9, 11], which suggests that they exist in natural concentrations so as to naturally enable oxygen transport by a vacancy mechanism. This will the assumed mode of oxygen migration in WO_2.

2.3.2 Migration energy: E_m^V

Migration energies are obtained using the *n*udged elastic band (NEB) method [12]. In the WO$_2$ crystal structure (monoclinic), there are three non-equivalent oxygen lattice positions, shown in Figure 2.1a and labeled as V_{O_1}, V_{O_2}, and V_{O_3}. The NEB paths for the $V_{O_1} \longleftrightarrow V_{O_2}$ and $V_{O_2} \longleftrightarrow V_{O_3}$ migration trajectories are shown in Fig. 2.1. The resulting energy barriers are summarized in the following table:

Path	E_m^V [eV]
$V_{O_1} \longrightarrow V_{O_2}$	2.19
$V_{O_2} \longrightarrow V_{O_1}$	1.86
$V_{O_2} \longleftrightarrow V_{O_3}$	1.96

By way of comparison, an energy of 2.46 eV has been calculated for the $V_{O_1} \longrightarrow V_{O_2}$ path [5]. While all of these oxygen vacancy exchanges are viable diffusive transitions, here we take the $V_{O_1} \longrightarrow V_{O_2}$ as representative of all vacancy jumps and proceed to calculate the attempt frequency for that path.

2.3.3 Attempt frequency: ν_0

ν_0 can be obtained by resorting to harmonic transition state theory as [6, 7]:

$$\nu_0 = \frac{\prod_i^{3N} \omega_i^{eq}}{\prod_i^{3N-1} \omega_i^{sp}} \tag{2.10}$$

where ω_i^{eq} and ω_i^{sp} are, respectively, the normal frequencies of vibration of the system at the equilibrium position (e.g., V_{O_1}) and saddle point of the migration path. In each case, the normal frequencies can be obtained by diagonalizing the *d*ynamical matrix, $\boldsymbol{D}$, generated at the equilibrium and saddle point positions, which amounts to solving the eigenvalue problem defined by:

$$\boldsymbol{D}\boldsymbol{\epsilon} = \boldsymbol{\lambda}\boldsymbol{\epsilon}$$
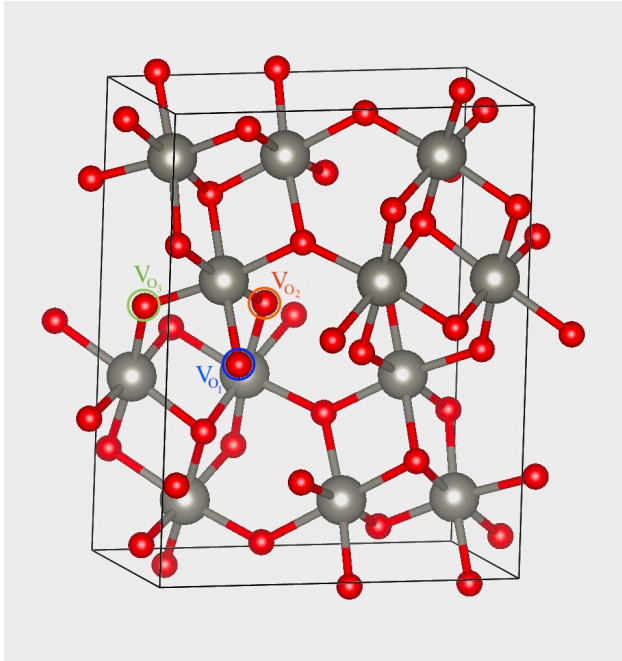
(a) WO$_2$ supercell
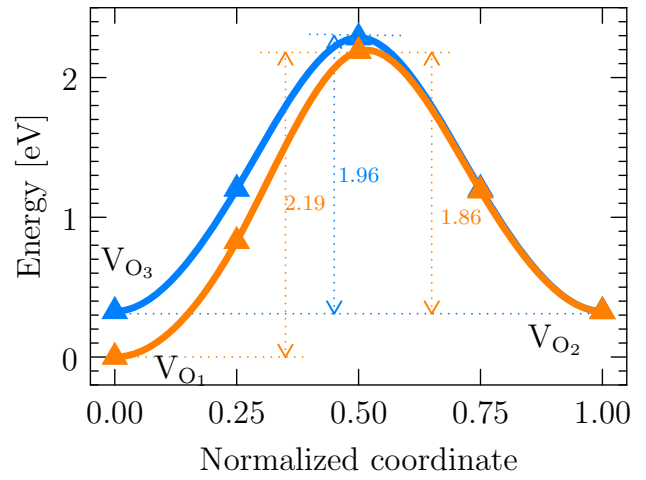
(b) NEB calculations

Figure 2.1: (a) WO$_2$ supercell employed in the calculations. Red spheres symbolize O atoms, blue spheres W atoms. The three oxygen vacancy sites considered are marked and labeled. (b) Oxygen vacancy migration energy paths for the $V_{O_1}\longleftrightarrow V_{O_2}$ and $V_{O_2}\longleftrightarrow V_{O_3}$ trajectories.

where ϵ is the eigenvector matrix and λ is a diagonal matrix containing all the eigenvalues of the system from which the eigenfrequencies can be calculated as $\omega_k = \sqrt{\lambda_{kk}}$. At the saddle point, one of the normal modes of vibration is undefined (imaginary eigenvalue) and eliminated from the product in the denominator of eq. 2.10, hence the $3N - 1$ limit of the product.

The results for the $V_{O_1} \longrightarrow V_{O_2}$ path give a value of $\nu_0 = 243.2$ THz, which, when inserted in eq. 3.11, results in $D_0 = 3.087 \times 10^{-5}$ m^2·s^{-1}. With this, the final expression for the oxygen diffusivity in WO$_2$ becomes:

$$D_4(T) = 3.087 \times 10^{-5} \exp\left(-\frac{1.9}{kT}\right) \ [\text{m}^2 \cdot \text{s}^{-1}] \tag{2.11}$$

These results are added to Table 3.2 to be used in the kinetic model simulations.

2.4   References

[1] Vladimir I Anisimov, Ferdi Aryasetiawan, and AI Lichtenstein. First-principles calculations of the electronic structure and spectra of strongly correlated systems: the lda+ u method. *Journal of Physics: Condensed Matter*, 9(4):767, 1997.

[2] Qingguo Feng. Electron correlation effect versus spin–orbit coupling for tungsten and impurities. *Journal of Physics: Condensed Matter*, 32(44):445603, 2020.

[3] John Hubbard. Electron correlations in narrow energy bands. *Proceedings of the Royal Society of London. Series A. Mathematical and Physical Sciences*, 276(1365):238–257, 1963.

[4] Oscar Hurtado-Aular, Rafael Añez, and Aníbal Sierraalta. Dft+ u study of the electronic structure changes of wo3 monoclinic and hexagonal surfaces upon cu, ag, and au adsorption. applications for co adsorption. *Surface Science*, 714:121907, 2021.

[5] C Linderalv. Structural and thermodynamical properties of tungsten oxides from first-principles calculations. Master's thesis, Chalmers University of Technology, 2016.

[6] J Marian, BD Wirth, A Caro, B Sadigh, GR Odette, JM Perlado, and T Diaz de la Rubia. Dynamics of self-interstitial cluster migration in pure α-fe and fe-cu alloys. *Physical Review B*, 65(14):144102, 2002.

[7] J Marian, BD Wirth, GR Odette, and JM Perlado. Cu diffusion in α-fe: determination of solute diffusivities using atomic-scale simulations. *Computational materials science*, 31(3-4):347–367, 2004.

[8] A Seidl. G ? rling, a.; vogl, p.; majewski, ja; levy, m. *Phys. Rev. B*, 53:3764, 1996.

[9] Zhenguang Shen, Zengying Zhao, Jian Wen, Jingwen Qian, Zhijian Peng, and Xiuli Fu. Role of oxygen vacancies in the electrical properties of wo3- x nano/microrods with identical morphology. *Journal of Nanomaterials*, 2018, 2018.

[10] Sarah A Tolba, Kareem M Gameel, Basant A Ali, Hossam A Almossalami, and Nageh K Allam. The dft+ u: Approaches, accuracy, and applications. *Density Functional Calculations-Recent Progresses of Theory and Application*, pages 3–30, 2018.

[11] Xinping Zhang, Fawei Tang, Meng Wang, Wangbin Zhan, Huaxin Hu, Yurong Li, Richard H Friend, and Xiaoyan Song. Femtosecond visualization of oxygen vacancies in metal oxides. *Science advances*, 6(10):eaax9427, 2020.

[12] Yue Zhao, Lucile Dezerald, and Jaime Marian. Electronic structure calculations of oxygen atom transport energetics in the presence of screw dislocations in tungsten. *Metals*, 9(2):252, 2019.

CHAPTER 3

Kinetic Model of W's Oxidation

3.1 Introduction

Corrosion of metallic structural materials is an extraordinarily broad phenomenon with implications in many areas of engineering [35, 39, 52]. In fusion energy devices, where tungsten (W) is the preferred candidate material for plasma-facing applications, the reaction chamber is designed to operate under nominal ($\approx 10^{-8}$ Torr) vacuum conditions [4, 10, 46]. However, under accident scenarios leading to a loss of cooling (LOCA) with simultaneous air ingress (due to loss of structural integrity of the vacuum chamber), W oxidizes rapidly, forming an unstable radioactive oxide that can break off mechanically and/or by sublimation, presenting a potentially-severe environmental hazard [18, 38, 43]. This has prompted the development of advanced tungsten alloys with enhanced oxidation resistance to eliminate the harmful release of toxic tungsten oxide into the environment in case of a LOCA event [5, 11, 27]. Good understanding of W oxidation rates is also needed to support the planning of execution of maintenance and decommissioning, where atmospheric control may be required to prevent the hazardous oxidation or the temperature may need careful control to restrict oxidation to more benign phases [8, 29]. As well, considerable interest in tungsten oxides stems from it use as a highly efficient hydrogen oxidation electrocatalyst [23].

While much progress has been made to understand the mechanisms of W oxidation in high temperature conditions [14, 34, 41], the inherent complexities associated with the co-existence of several different tungsten oxide phases make this topic one still under vigorous

16

investigation. Under nominal conditions, W oxide structures experiences a series of transformations where temperature, stresses, and environmental conditions all play key roles in the evolution of the oxide scale. Cifuentes *et al.* [7] have provided an excellent description of the overall oxidation process at high temperature, which is summarized as follows: "At 600°C, a protective $WO_{2.72}$ layer forms. This layer cracks at a prescribed thickness, leading to a rapid increase in mass gain resulting from fast oxygen transport through percolation pathways. The arrival of oxygen at the $WO_{2.72}$/metal interface turns the oxide into a coarse non-protective columnar $WO_{2.9}$ layer. The relative abundance of vacancies in $WO_{2.9}$ favors oxygen transport into the alloy, leading to rapid growth. Above 700°C, growth stresses in the scale are released through local cracking. At this stage, $WO_{2.9}$ becomes progressively transformed into WO_3 when the oxygen partial pressure increases across the scale thickness". As well, Lassner and Schubert [23] confirm that above 500°C the native $WO_{2.72}$ oxide layer cracks, and above 600°C turns into WO_3. WO_3 is permeable to oxygen, and its formation rate depends on the oxygen ion transport to the WO_3/$WO_{2.72}$ interface. So long as the $WO_{2.72}$ layer thickness stays below its critical value, the growth is parabolic, while –after it cracks– the growth turns to linear.

The fact that WO_{3-x} phases form below their equilibrium temperature threshold is likely related to the existence of compressive tangential stresses with a high Pilling-Bedworth ratio [37]. These stresses stabilize the oxide layer during the incipient growth phase but they build up with layer thickness, which ultimately results in loss of protection and cracking [16, 17]. The process described by Cifuentes *et al.* and Lassner and Schubert does not involve the WO_2 phase. This could be caused by failure to achieve steady state during the length of time attained in experiments, or an inability to detect the WO_2 layer. Coexistence of WO_2 and WO_3 has been detected, however, under certain conditions [48]. The next stage of the oxidation process occurs when the WO_3 has covered the surface of the thin dark film. Being porous, not particularly adhesive and having a Pilling-Bedworth ratio of 3.35, this oxide creates high stresses causing the oxide layer to crack and thus exposing new surface

to the oxygen. At this point, the non-protective nature of the WO_3 layer results in a linear oxidation rate.

Under loss-of-coolant or loss-of-vacuum conditions, air ingress and decay heat can push the temperatures in the tungsten between 1200 and 1500°C for several weeks [28]. At these temperatures, oxidation of pure W is almost immediate, and direct sublimation of WO_3 is then the main concern. The favored allotrope of WO_3 in this situation is the tetragonal (α) structure, with the rest of tungsten oxide phases becoming marginally stable and not observed [30].

Understandably, the multi-parametric nature and microstructural complexity of tungsten oxidation presents a difficult challenge for developing predictive material models and design guidelines. Recently, Nagy and Humphry-Baker have provided an oxidation mechanism map from an extensive compilation of experimental data [33]. These maps are an excellent visual tool to quickly determine the expected oxidation behavior of tungsten slabs as a function of temperature and time. However, unlike for oxidation of nuclear materials [37], there is a lack of fundamental models operating at relevant scales to simulate oxide scale growth under a variety of conditions. In this work, we present a kinetic model of oxide interface evolution based on oxygen transport across a series of layers representing different oxide stoichiometries. The model is informed by equilibrium phase diagrams by furnishing the appropriate oxide phases at each thermodynamic condition. The model is parameterized with a combination of experimental and calculated material properties and physical constants. In particular, we carry out density functional theory (DFT) calculations of oxygen vacancy formation and migration energy barriers, as well as the attempt frequency in WO_2 to define the oxygen diffusivity in the corresponding layer.

The paper is organized as follows. First, a review of the physical-chemistry of W oxidation and a detailed description of the methods developed here are provided in Sec. 3.2. The results of the paper are presented in Sec. 3.3, including DFT calculations of diffusion parameters in WO_2 and simulations furnished by the model under several different scenarios. We provide

18

a discussion of our findings in Sec. 5.4, and finish with the main conclusions of the paper in Sec. 3.5.

3.2 Methods

3.2.1 Preliminary considerations

Under high oxygen partial pressure conditions, the WO_3 layer grows by the transfer of mass from the metal represented by the reaction:

$$W^{6+} + 3O^{2-} \rightarrow WO_3 \tag{3.1}$$

This reaction is enabled by the reduction of molecular oxygen[1] on the environment side:

$$O_2 + 2e^- \rightarrow 2O^{2-} \tag{3.2}$$

which receives electrons from the oxidation of metal tungsten within the metal substrate:

$$W \rightarrow W^{6+} + 6e^- \tag{3.3}$$

The formation of WO_{3-x} phases follows the same sequence as above but with other oxidation states of tungsten as the starting point, such as +2, +3, +4, or +5.

On the basis of these considerations, in the most general case the oxidation of metallic tungsten will evolve into a structure characterized by five distinct layers. These layers represent different tungsten-oxygen structures ranging from WO_3 on the environment side (where O radicals are produced) to the W-O metallic solid solutions (where the metal is reduced). In between, three more oxide phases are expected to form, namely, $WO_{2.9}$, $WO_{2.72}$, and WO_2. More details about the structure and properties of the different oxide compounds can be found in 3.6.1. As shown in Fig. 3.1a, $WO_{2.9}$ should only exist above 484°C, while $WO_{2.72}$ is expected to appear only above 585°C. WO_3 and WO_2 exist as equilibrium phases

---

[1]In aqueous conditions, the equivalent process is: $H_2O \rightarrow O^{2-} + 2H^+$
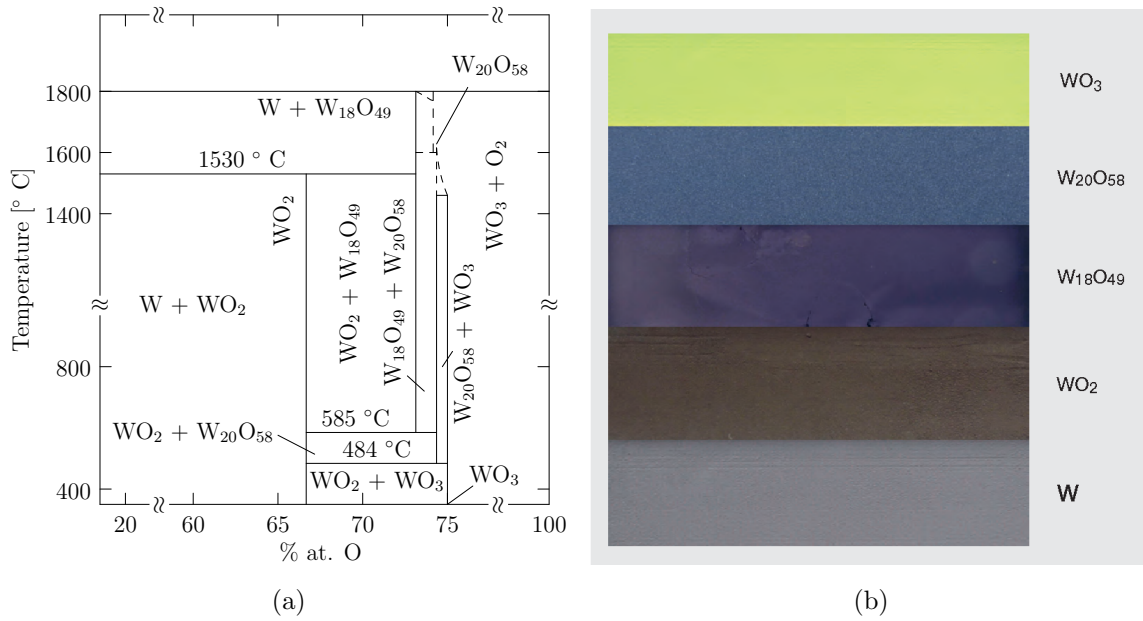
Figure 3.1: (a) W-O phase diagram, adapted from ref. [12]. (b) Colors of the tungsten oxides: yellow WO_3, blue $WO_{2.9}$, violet $WO_{2.72}$, chocolate-brown for WO_2, and gray for the W metal. From ref. [50].

in the entire temperature range. All these oxides appear as strong line compounds in the phase diagram, suggesting that the should form with near perfect stoichiometry.

3.2.2 Diffusion kinetics

The model starts with the adsorption of oxygen radicals at the surface of the material. Adsorption is a thermally activated process that sets the rate of oxygen atom ingress in the solid:

$$\dot{c}_0 = c_0 \nu_{\mathrm{ads}} = c_0 \nu_{\mathrm{ads}}^0 \exp\left(-\frac{E_{\mathrm{ads}}}{kT}\right) \tag{3.4}$$

where c_0 is the concentration of oxygen radicals in solution on the environment side, ν_{ads}^0 is an oxygen pick-up rate, E_{ads} is the adsorption activation energy, k is Boltzmann's constant, and T the absolute temperature. The value of c_0 is environment-dependent, but as a reference the oxygen concentration in air under standard ambient conditions is 5.64×10^{24} m^{-3} [1]. The activation barrier for adsorption depends on the structure of the surface, and ranges between 0.1 and 1.0 eV [13, 32, 42]. For lack of better data, here we take $\nu_{\mathrm{ads}}^0 = 10^{12}$ Hz and $E_{\mathrm{ads}} = 1.0$ eV. Note that the model can be solved using both $\dot{c}_0$ or c_0 as boundary conditions on the environmental side.

The model of oxide growth can then be formulated by considering the motion of four interfaces, each characterized by its own evolution equation. Together, the motions of these interfaces determinate the rate of oxidation of the underlying metal substrate. Note that this means that the oxide grows *into* the metal, which is the correct physical assumption due to mass conservation. As well, here we ignore the relative volumetric expansion of the oxide layers relative to the initial metal phase. The evolution equations can be written assuming a sharp-interface model (known as a *Stefan* model) in one dimension:

$$\dot{s}_i(x) = \frac{\Delta J_i|_{s_i}}{n_i \rho_{\mathrm{W}}} \tag{3.5}$$

where the subindex i refers to a specific interface, x is the depth coordinate, $\Delta J_i|_{s_i}$ is the net flux of (free) oxygen exiting the interface towards the interior, n_i is the O-to-W atomic

ratio, and ρ_W is the atomic density of tungsten. The above equation describes the rate of advance of a specific interface on the basis of the oxygen flux differential on both sides of the interface. In essence, an interface must move to maintain mass continuity dynamically. The full derivation of eq. 3.5 is contained in 3.7. To determine $\Delta J_i|_{s_i}$, one must solve a diffusion equation in each oxide sublayer to first determine the free oxygen concentration profile and then obtain the flux using Fick's first law:

$$\Delta J_i|_{s_i} = J_i|_{s_i+} - J_i|_{s_i-} = D_i \frac{\partial c}{\partial x}\bigg|_{s_i+} - D_{i-1} \frac{\partial c}{\partial x}\bigg|_{s_i-} \tag{3.6}$$

$$\frac{\partial c}{\partial t} = D_i \frac{\partial^2 c}{\partial x^2} \tag{3.7}$$

Equation 3.7 is subjected to two concentration boundary conditions, one for each interface bounding each oxide sublayer. At the inner edge of the layer (i.e., at $x = s_i$), $c = 0$ always. At the outer edge of the layer ($x = s_{i-1}$), $c = \rho_W (n_{i-1} - n_i)$. The exceptions to this are the outermost and innermost layers (which are both fixed, i.e., $\dot{s}_0 = \dot{s}_5 = 0$), where $c = c_0$ and $J_5 = 0$, respectively. The specific values for each sublayer are given in Table 3.1.

Table 3.1: Details for the formulation of the Stefan model of multilayer interface evolution.

Layer	Compound	n	Outer interface	Inner interface	Outer boundary condition $[\rho_W]$	Inner boundary condition $[\rho_W]$
1	WO_3	3.0	s_0	s_1	$c = c_0$	$c = 0$
2	$WO_{2.90}$	2.90	s_1	s_2	$c = 0.1$	$c = 0$
3	$WO_{2.72}$	2.72	s_2	s_3	$c = 0.18$	$c = 0$
4	WO_2	2.0	s_3	s_4	$c = 0.72$	$c = 0$
5	W-O metal	-	s_4	s_5	$c = 2.0$	$J = 0$

3.2.3 Multilayer structure

Note that here we are assuming that all the oxygen above the stoichiometric concentration in each layer is insoluble in that layer, while according to the phase diagram some of it starts to precipitate as the next phase richer in oxygen. However, here we treat this as having a minor effect on the kinetics. As well, a delayed formation of a WO_x phase can take place even when the oxygen concentration is lower than $x\rho_W$. In that case, as eq. 3.4 indicates, building up the oxygen concentration up to the required value for each stoichiometric oxide phase to form, takes an amount of time given by $\Delta t = x/\dot{c}_0$. The assumption made in this work is that this time does not compute towards the total oxide layer formation time. The equations to be solved for each layer, with the appropriate numerical notation and boundary conditions to be used are given below. To indicate the boundary conditions on the right-hand side of a given interface i (with respect to the frame of reference on Figure 3.2), the suffix 's_i+' ('s_i-' to refer to the left side).

Layer 1:

Material	WO$_3$
Governing equations	$\dot{s}_1(x) = \frac{\Delta J_1\|_{s_1}}{3.0\rho_W}$ $\Delta J_1\|_{s_1} = D_2\frac{\partial c}{\partial x}\Big\|_{s_1+} - D_1\frac{\partial c}{\partial x}\Big\|_{s_1-}$ $\frac{\partial c}{\partial t} = D_1\frac{\partial^2 c}{\partial x^2}$
Boundary conditions	$c(0) = c_0 - 3\rho_W, \ \ c(s_1) = 0$ (as well : $\dot{c}(0) = \dot{c}_0$)

23
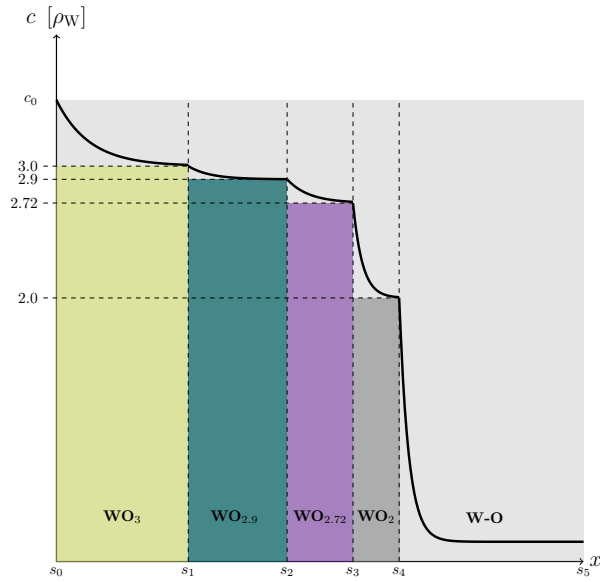
Figure 3.2: Schematic representation of the multilayer system in steady state. The absorbed oxygen is partitioned into 'chemical' oxygen, which is immobilized in the oxide structures themselves, and 'free' oxygen, which diffuses through each layer and is represented by a concentration profile shown as a thick black line. Note that the width of each layer is arbitrary in the figure.

Layer 2:

Material	WO$_{2.9}$
Governing equations	$\dot{s}_2(x) = \dfrac{\Delta J_2\vert_{s_2}}{2.9\rho_{\mathrm{W}}}$ $\Delta J_2\vert_{s_2} = D_3 \dfrac{\partial c}{\partial x}\bigg\vert_{s_2+} - D_2 \dfrac{\partial c}{\partial x}\bigg\vert_{s_2-}$ $\dfrac{\partial c}{\partial t} = D_2 \dfrac{\partial^2 c}{\partial x^2}$
Boundary conditions	$c(s_1) = 0.1\rho_{\mathrm{W}}, \ \ c(s_2) = 0$

Layer 3:

Material	WO$_{2.72}$
Governing equations	$\dot{s}_3(x) = \dfrac{\Delta J_3\vert_{s_2}}{2.72\rho_{\mathrm{W}}}$ $\Delta J_3\vert_{s_3} = D_4 \dfrac{\partial c}{\partial x}\bigg\vert_{s_3+} - D_3 \dfrac{\partial c}{\partial x}\bigg\vert_{s_3-}$ $\dfrac{\partial c}{\partial t} = D_3 \dfrac{\partial^2 c}{\partial x^2}$
Boundary conditions	$c(s_2) = 0.18\rho_{\mathrm{W}}, \ \ c(s_3) = 0$

Layer 4:

Material	WO$_2$
Governing equations	$\dot{s}_4(x) = \frac{\Delta J_4\|_{s_3}}{2.0\rho_{\text{W}}}$ $\Delta J_4\|_{s_4} = D_5 \frac{\partial c}{\partial x}\Big\|_{s_4+} - D_4 \frac{\partial c}{\partial x}\Big\|_{s_4-}$ $\frac{\partial c}{\partial t} = D_4 \frac{\partial^2 c}{\partial x^2}$
Boundary conditions	$c(s_3) = 0.72\rho_{\text{W}}, \ c(s_4) = 0$

Layer 5:

Material	W-O (metal)
Governing equations	$\frac{\partial c}{\partial t} = D_5 \frac{\partial^2 c}{\partial x^2}$
Boundary conditions	$c(s_4) = 2.0\rho_{\text{W}}, \ J(s_5) = 0$

When a given layer cracks, a modification to the above formulation must be adopted. When a layer i bounded by oxygen concentrations of c_{i-1} and c_i fragments after it reaches a critical width, w_i^*, it opens up percolation pathways that equalize the free oxygen concentration across it [3], i.e., $c_{i-1} = c_i$. When such a situation arises, the layer in question stops growing and simply acts as an oxygen bridge between its two adjacent layers. During the simulations that will be presented below, a provision is introduced in the model to switch to this mode of oxygen transport once w_i^* is reached.

3.2.4 Discretized multilayer equations

Here we adopt a first-order finite difference scheme to solve the diffusion equations (Fick's 1st and 2nd laws) given in the previous sections. A one-dimensional central finite difference approach results in the following discretized form:

$$c_i^{n+1} = c_i^n + \delta t D \left(\frac{c_{i+1}^n - 2c_i^n + c_{i-1}^n}{\delta x^2} \right) \tag{3.8}$$

$$J_i^n = -D \frac{c_{i+1}^n - c_{i-1}^n}{2\delta x} \approx -D \frac{c_i^n - c_{i-1}^n}{\delta x} \tag{3.9}$$

where δt and δx are the time and space increments, and the subindices n and i refer to temporal and spatial steps. Both equations above are subjected to the Neumann stability condition $\delta t < \delta x^2 / D$.

Application of the boundary conditions leads to:

$$c_i^0 = 0, \ c_0^n = c_0, \ c_{s_5}^n = c_{s_5 - \delta x}^n$$

While the total oxygen concentration (stoichiometric plus free) is continuous at each interface, each diffusion equation in each layer is solved only for the free oxygen concentration. This results in jumps in the concentration depending on whether one looks at the interface from the left or from the right in Fig. 3.2. With the coordinate x arriving at each interface, one has:

$$c_{s_1}^n = c_{s_2}^n = c_{s_3}^n = c_{s_4}^n = 0$$

and with x leaving each interface:

$$c_{s_1}^n = 0.10, \ c_{s_2}^n = 0.18, \ c_{s_3}^n = 0.72, \ c_{s_4}^n = 2.00$$

all in units of ρ_W.

3.2.5 Material parameters and DFT calculations

The above model is fully defined when the external parameters, T and c_0, and the material properties, ρ_W and the diffusivities, are specified. Here, T and c_0 are prescribed, and the

value of ρ_W is known. That leaves the diffusivities D_i $(i = 1, 5)$ as the remaining material constants to determine.

The general expression for the diffusion coefficient is the standard Arrhenius form:

$$D(T) = D_0 \exp\left(-\frac{E_a}{kT}\right) \tag{3.10}$$

where D_0 is the diffusion pre-factor and E_a is the activation energy. That means that five separate pre-factors and five activation energies must be determined for each oxide layer. In all cases, TEM experiments have revealed that the oxide always grows into the tungsten metallic matrix, confirming that oxide growth is controlled by oxygen anion diffusion from the environment side inwards [45].

In any case, the first thing to ascertain is whether oxygen is transported by a vacancy mechanism (through exchanges with empty oxygen sublattice sites) or as interstitial atoms in an otherwise fully-occupied lattice. On first inspection of Fig. 3.1a, the line compound structure of all the oxide sublayers considered here (in Fig. 3.2) suggests that oxygen atoms will diffuse as free interstitials in all cases. However, there is sufficient consensus about the abundance of oxygen vacancies, both thermal and chemical (i.e., due to natural stoichiometric deviations) in all oxide phases [21, 22, 31, 49], and so here we assume going forward that all oxygen transport within the oxide laters takes place via a vacancy mechanism. Next, we select oxygen diffusion properties for each layer shown in Sec. 3.2.3, either from literature sources or –if unavailable– by carrying out DFT calculations using the methodology described in 2.2.1.

3.2.5.1   WO$_3$ layer

Sikka and Rosa [41] studied oxidation of pure W in the 568-908°C interval and measured an oxygen diffusivity of $D(T) = 6.83 \times 10^{-6} \exp\left(-1.3/kT\right)$ [cm^2·s^{-1}]. Such experiments are conducted under the assumption that tungsten trioxide is under some slight deviation, represented by x (not to be confused with the spatial coordinate), from stoichiometry. i.e., in

WO_{3-x}. The measured activation energy of 1.3 eV is indeed suggestive of a vacancy mechanism if one takes the activation energy as being the sum of the oxygen vacancy formation and migration energies. DFT calculations of oxygen vacancy formation energies consistently yield values of $\approx$1.5 eV [22, 25], while for the migration energy alone, energies between 0.4 and 0.9 eV are obtained [6, 25].

With this, we take the values measured by Sikka and Rosa [41] for $D_1(T)$.

3.2.5.2 WO$_2$ layer

In contrast to WO$_3$, no data are available for oxygen diffusion in WO$_2$ and we proceed to calculate O diffusivity in layer 4. Here too, a vacancy mechanism is assumed. The starting point for the calculations is an expanded expression for the diffusivity:

$$D_4(T) = zc_V(T)\ell^2\nu(T) \tag{3.11}$$

where z is a geometric factor, ℓ is the jump distance,

$$c_V(T) = \exp\left(-\frac{E_f^V}{kT}\right)$$

is the thermal vacancy concentration (E_f^V is the oxygen vacancy formation energy), and

$$\nu(T) = \nu_0 \exp\left(-\frac{E_m^V}{kT}\right)$$

is the jump frequency with E_m^V the oxygen vacancy migration energy. Equations 3.10 and 3.11 imply that $D_0 = z\ell^2\nu_0$ and $E_a = E_m^V + E_f^V$. The factor z, which includes the number of jump sites n_p and the dimension of diffusion d, is $n_p/2d = 5/3$, and the jump distance ℓ is 2.76 Å for the oxygen sub-lattice in WO$_2$ [20, 47]. In this work, E_f^V, E_m^V, and ν_0 were obtained using DFT calculations as reported in 2.3. The final expression for $D_4(T)$ is given in eq. 2.11.

3.2.6 WO$_{2.9}$ and WO$_{2.72}$ layers

No data whatsoever exist for the diffusivity of oxygen in the WO$_{2.9}$ and WO$_{2.72}$ layers. In their analysis of oxidation kinetics data, Nagy and Humphry-Baker identified three bands of oxygen partial pressure, low (0.1 atm), medium (0.2 atm), and high (3.4~13.6 atm). They extracted effective activation energies of 1.22, 1.40, and 1.94 eV for each one [33]. By mapping O partial pressures to oxygen/metal ratio, these can loosely be ascribed to diffusion in WO$_{2.72}$, WO$_{2.9}$, and WO$_3$, respectively. Indeed, these energies are not inconsistent with the values of 1.3 and 1.5 eV measured and calculated for oxygen diffusion in WO$_3$ [22, 41]. We thus select 1.22 and 1.40 eV as the activation energies for WO$_{2.72}$, WO$_{2.9}$. In terms of the prefactor, for lack of a more suitable option, here we take that in D_1 to be the same in D_2 and D_3.

3.2.6.1 Metallic W

The solubility of oxygen in W is very low [23] and O atoms are found primarily in interstitial positions. Specifically, interstitial oxygen is seen to diffuse in the W lattice throughout tetrahedral positions with a migration energy of 0.15 eV [53]. The diffusion pre-factor has been obtained by Alkhamees *et al.* [2] to be 7.6×10^{-8} m^2·s^{-1}, i.e.:

$$D_5(T) = 7.6 \times 10^{-8} \exp\left(-\frac{0.15}{kT}\right) \quad [\text{m}^2 \cdot \text{s}^{-1}] \tag{3.12}$$

Table 3.2 lists all the diffusivities used in the multilayer model.

3.2.7 Critical fragmentation widths

As indicated at the end of Sec. 3.2.3, fragmentation of an oxide scale occurs due to the large epitaxial misfit between the metal substrate and the oxide phase. These creates residual stresses (known as Pilling-Bedworth stresses) that put the oxide under compression, building up as the layer grows. At a critical thickness threshold, which we term w^*, the layer fragments

Table 3.2: Compilation of diffusivity parameters used in the multilayer tracking model developed in this work.

Diffusivity	Material	D_0 [m^2·s^{-1}]	E_m^V [eV]
D_1	WO$_3$		1.3
D_2	WO$_{2.9}$	6.8×10^{-6}	1.40
D_3	WO$_{2.72}$		1.22
D_4	WO$_2$	3.1×10^{-5}	1.90
D_5	W metal	7.6×10^{-8}	0.15

generally creating a network of cracks through which oxygen can flow unimpeded [3]. At this stage, oxygen transport ceases to be the rate limiting step in oxide layer growth, which is subsequently seen to scale linearly with time. Linear growth can also coexist with parabolic (diffusive) growth. Indeed, the presence of exponents between 0.5 and 1.0 in oxidation experiments is suggestive of the coexistence of cracked layers and protective layers [7, 33].

By its own definition, these stresses set in only between the oxide phase immediately in contact with the metallic base. As such, in a multilayer setting as the present one, one would expect only one single layer to undergo cracking at any give time. A compilation of data relating temperature, critical width w^*, and oxide phase is provided in Table 3.4 (3.6.2). These are based on measurements performed by Gulbransen and Andrew [14] and analyzed by Nagy and Humphry-Baker [33]. As the table shows, the WO$_2$ phase is common to all oxidation conditions, consistent with the expectation that it should be the layer immediately adjacent to the metal substrate[2] On the basis of these data, in the forthcoming simulations, we assume that in impoverished oxygen atmospheres, a WO$_2$ layer forms and grows up to a temperature-dependent thickness given by the listed values of w^*.

---

[2]However, care should exercised in utilizing these data, as they were obtained in depleted oxygen conditions where WO$_2$ and WO$_{2.72}$ phases would be favored.

3.3 Results

3.3.1 Oxide growth simulations as a function of temperature

Next, we present results of the oxide layer growth as a function of temperature. We consider three temperature regions, (i) at or below 600°C (873 K), (ii) between 600 and 800°C (873 to 1073 K), and (iii) at or above 800°C. We initialize the model with the temperature value and a boundary oxygen concentration, c_0, that favors the formation of the oxide phases listed in Table 3.4. We set δt and δx to 1 ns and 1 nm, respectively, which are sufficiently small to always guarantee the numerical stability of the finite-difference solution procedure. In all cases, we show results for the first 30 s of evolution, when the thickness of all oxide layers involved is well below the fragmentation threshold (second column of Table 3.4). As such, the results presented below correspond to the regime when the oxide maintains its protective structure, which can thus be assumed until its thickness reaches the critical width at each temperature.

We give the results in each case as a pair of plots, one showing the depth profiles of all the sublayers involved color-coded by the time instant for which they are displayed, and the other showing the position of the different interfaces as a function of time. c is always given in units of ρ_W. The depth profiles are always color-coded by the scale used in Fig. 3.1b to facilitate the identification of each oxide type.

3.3.1.1 Kinetic model simulations at $600°C$

The results at this temperature are shown in Figure 3.3. As indicated in Table 3.4, only $WO_{2.72}$ and WO_2 form at this temperature. Figure 3.3a reveals a very thin WO_2 layer behind $WO_{2.72}$, also captured in Fig. 3.3a. A power law fit to the s_4-t graph yields $s_4(t) = 3.747t^{0.407}$, indicating a substantial deviation from pure parabolic growth law.

32
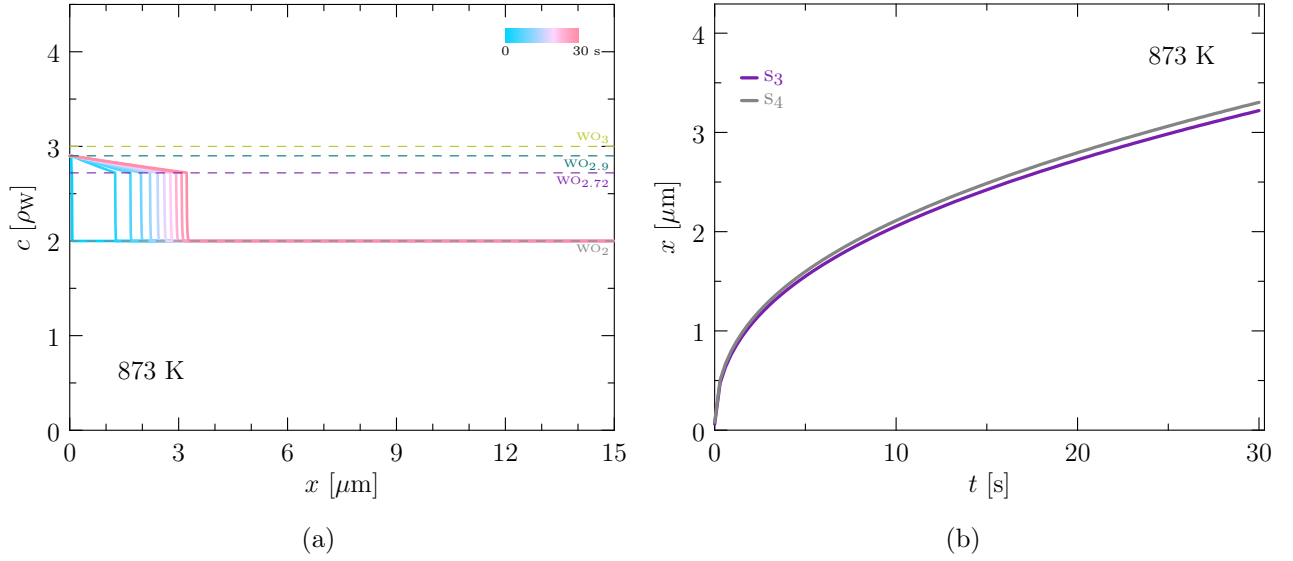
Figure 3.3: (a) Depth-time profiles of the oxide layer structure at 873 K. (b) Time evolution of the $WO_{2.72}/WO_2$ (s_3) and WO_2/metal (s_4) interfaces during the first 30 s of exposure.

3.3.1.2 Kinetic model simulations at $600 < T < 800°C$

The slow growth of the WO_2 layer carries over to the simulations at 650 and 700°C (923 and 973 K). At 650°C, however, all oxide sublayers are present, Figs. 3.4a and 3.4b, with WO_3 also displaying slow growth kinetics. At 700°C, Figs. 3.4c and 3.4d, the evolution is qualitative similar to that at 600°C given in the previous subsection. In this case, the growth law exponents at 650 and 700°C are 0.41 and 0.44.

3.3.1.3 Kinetic model simulations at and above 800°C

Figure 3.5 shows the corresponding graphs at 800 and 1000°C. At these temperatures, again according to the observed phases in the experiments listed in Table 3.4, only the WO_2 phase forms. Interestingly, at 800°C the growth kinetics is quite slow, with the power law fit being $s_4(t) = 1.852t^{0.454}$ (in microns). By contrast, at 1000°C the temperature is sufficiently high to overcome the diffusion barrier of oxygen in WO_2, giving rise to faster kinetics compared

33
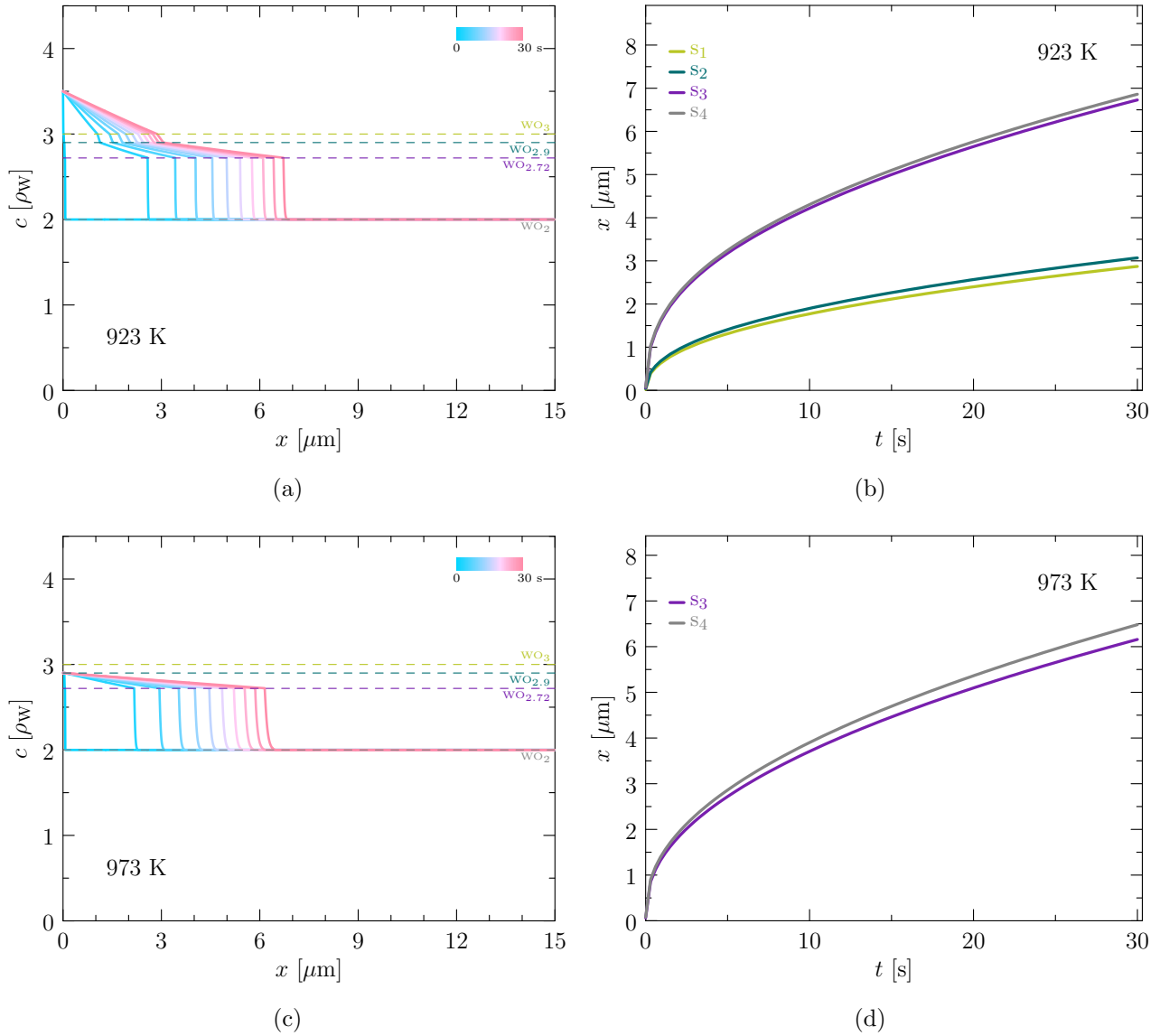
Figure 3.4: Depth-time profiles of the oxide layer structure at 923 (a) and 973 K (c). Corresponding time evolution of the different oxide interfaces interfaces during the first 3 s of exposure, (b) and (d).

to the previous scenarios. As such, the fitted expression in this case is $s_4(t) = 7.812t^{0.490}$. As revealed by the value of the power exponents, having one layer only forming part of the oxide significantly approximates the kinetics to the pure parabolic case.
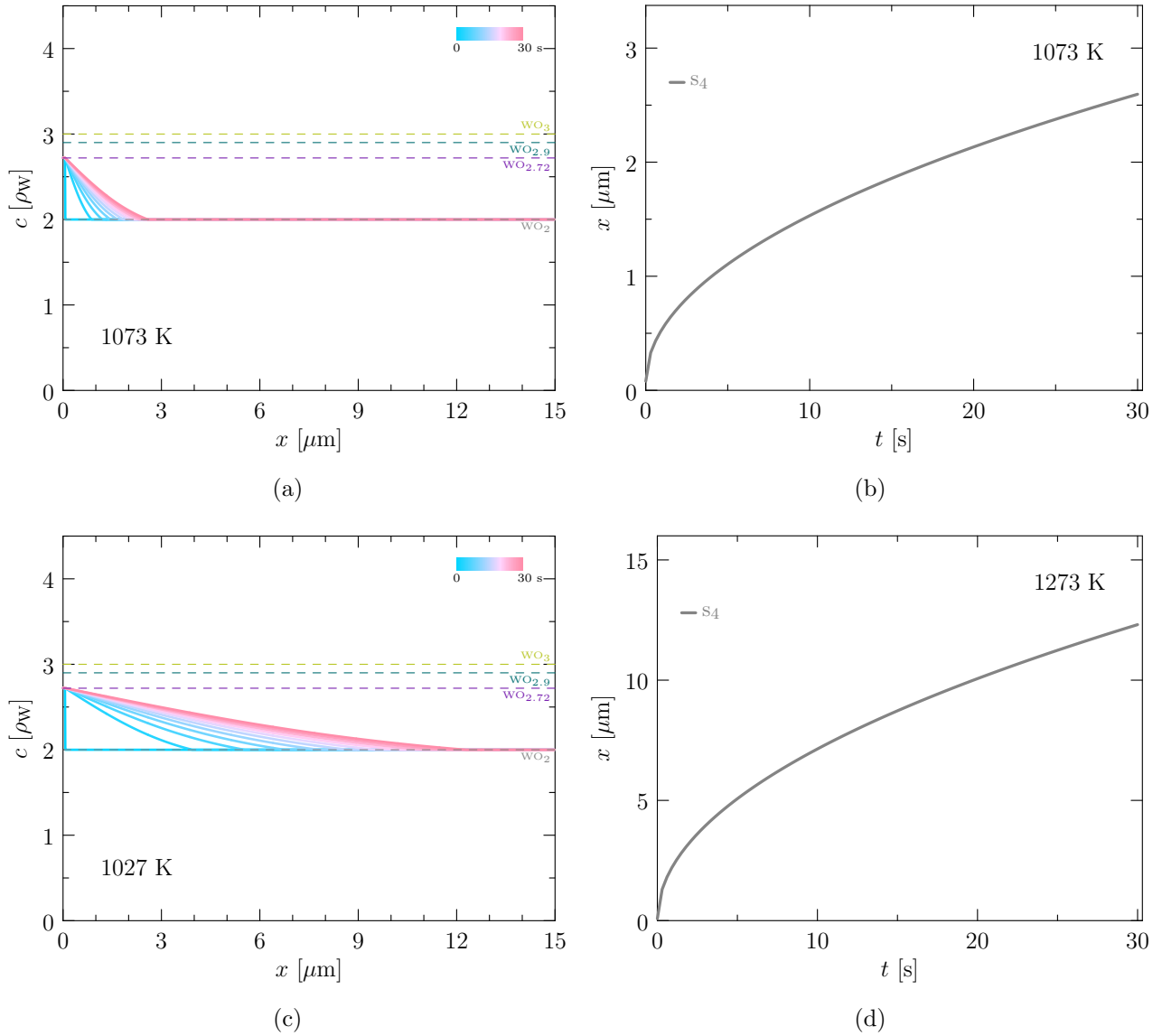
Figure 3.5: Depth-time profiles of the oxide layer structure at 1073 (a) and 1273 K (c). Corresponding time evolution of the different oxide interfaces interfaces during the first 3 s of exposure, (b) and (d).

All the fitting coefficients are compiled for each temperature in Table 3.3. It is worth mentioning that the power law exponents obtained here are similar to those measured in *SMART* W-based alloys [19, 27].

Table 3.3: Power law fitting coefficients $s_i(t) = at^b$ for all the temperatures considered in this work. Sublayer thickness given in units of microns.

T [K]	number of sublayers	a	b	k_p [mg^2 cm^{-4} min^{-1}]
873	2	3.747	0.407	4.28
923	4	7.930	0.413	20.31
973	2	6.435	0.441	16.69
1073	1	1.852	0.454	3.85
1273	1	7.812	0.490	34.20

3.4 Discussion

3.4.1 Main feature of the numerical model

The model presented here is formulated as a Stefan interface tracking approach where different oxide/oxide and oxide/metal interfaces evolve in time driven by discontinuities in oxygen fluxes across each one of them. These fluxes emerge in each oxide sublayer from the diffusion of free oxygen (i.e., not chemically immobilized) as a function of temperature. As such, it is crucial to have accurate oxygen diffusivities for the different oxide layers. These can be inferred from mass gain experiments, by assuming parabolic growth laws governed by pure diffusion. Unfortunately, most experimental works do not discriminate among the different oxide subphases, which has prompted the use of computational techniques to calculate the diffusivity in specific WO compounds [24, 26]. Even then, the computational data is scarce and does not address many of the gaps in our understanding of oxygen diffusion in tungsten oxide. For example, it is not clear whether oxygen diffusion primarily takes place by an interstitial or a vacancy mechanism in each of the different oxide phases. Here, we have applied electronic structure calculations to quantify the migration parameters of oxygen atoms in WO$_2$ by a vacancy mechanism, which was lacking in the literature.

From this point of view, this work is a first attempt at embedding the thermodynamic and kinetic complexity of tungsten oxide growth into a comprehensive mesoscale kinetic model that captures the more important features of the oxidation process. Below we provide further discussion about how the model has been designed, implemented, and validated.

3.4.2 Physical model validity

In this work, the simulated oxide structures are inspired by empirical observations of the outermost oxide layer during environmental exposure of pure W [7, 14, 15, 41] (see 3.6.2). Of note is the apparent absence of tungsten trioxide in oxidized samples. Indeed, WO_3 is not customarily seen to form as a standalone layer in the majority of experimental works scrutinized in this work. Instead, WO_3 forms only after lower order oxides have grown and cracked, allowing for fast oxygen transport pathways that stimulate the formation of the trioxide. For example, in a recent work Cifuentes et al. [7] note that, at 600°C, the oxidation was initially controlled by the development of a continuous $WO_{2.72}$ layer, which grows until it starts cracking leading to linear kinetics. At 700 and 800°, after cracking of the $WO_{2.72}$ layer, $WO_{2.92}$ is progressively seen to form, eventually turning into WO_3 in the course of the oxidation. Other times, $WO_{2.92}$ volatilization after cracking exposes tungsten to the exposed surface, leading to the formation of a yellow external WO_3 layer [7]. This evidence points to a mechanism of formation of WO_3 by which its formation takes place only after the $WO_{2.72}$ (and WO_2, discussed further below) layer has fragmented and lost its protective abilities.

The lack of stated observation of WO_2 in many of these experiments may be due to its intrinsic small thickness. Indeed, our calculations suggest that oxygen transport through tungsten dioxide is slow (mostly owing to a migration energy of almost 2.0 eV, Table 3.2), making WO_2 a true protective layer. Only above 1000°C is WO_2 seen to form at high rates, although at such temperatures all oxide layers start becoming structurally unstable due to sublimation. Based on this presumed behavior, our interpretation of the kinetics of oxide growth is that: (i) the free oxygen concentration under nominal conditions is generally never

37

sufficiently high to form WO_3 directly; (ii) the most common oxide sublayers are $WO_{2.72}$ and WO_2; (iii) these layers will grow in a protective fashion until a critical thickness is reached, at which point cracking occurs and the oxygen-rich phases $WO_{2.92}$ and WO_3 begin to form; (iv) whenever multiple oxide sublayers form in succession, deviations from the standard parabolic growth law are clearly seen. In our case, fracture and fragmentation is not a part of the current model, and we control the formation of the different oxides simply by regulating the amount of available oxygen, c_0, on the environment side of the exposed metal. c_0 is in fact the only parameter of our model that is 'adjusted' to reproduce certain observations.

3.4.3 Comparison to experimental measurements

A useful exercise is to compare the growth kinetics simulated in this work to available experimental data. As is customary in most works, oxide scale growth is measured in terms of tungsten mass gain assuming parabolic growth. Consequently, the mass gain constant is obtained from first to the data expressed linearly in time.

$$(\Delta m)^2 = [(n\rho_W)s_4(t)]^2 = k_p t$$

where Δm is the mass gain, $n\rho_W$ is the amount of oxygen gained when a WO_n oxide forms (expressed as a mass density), and k_p is the parabolic kinetic constant. Next, we fit all the sublayer evolutions shown in Figs. 3.3-3.5 to ideal parabolic growth expressions and plot the simulated values of k_p in Figure 3.6 along with a set of experimental measurements. The numerical values of k_p extracted from the simulations are also given in Table 3.3. The results show that, while the simulated values generally overestimate the experimental measurements, they lie within the broader range of the data at some temperatures. Given the figurative 'distance' between how the model was developed and how experiments are performed, we consider these differences reasonable.
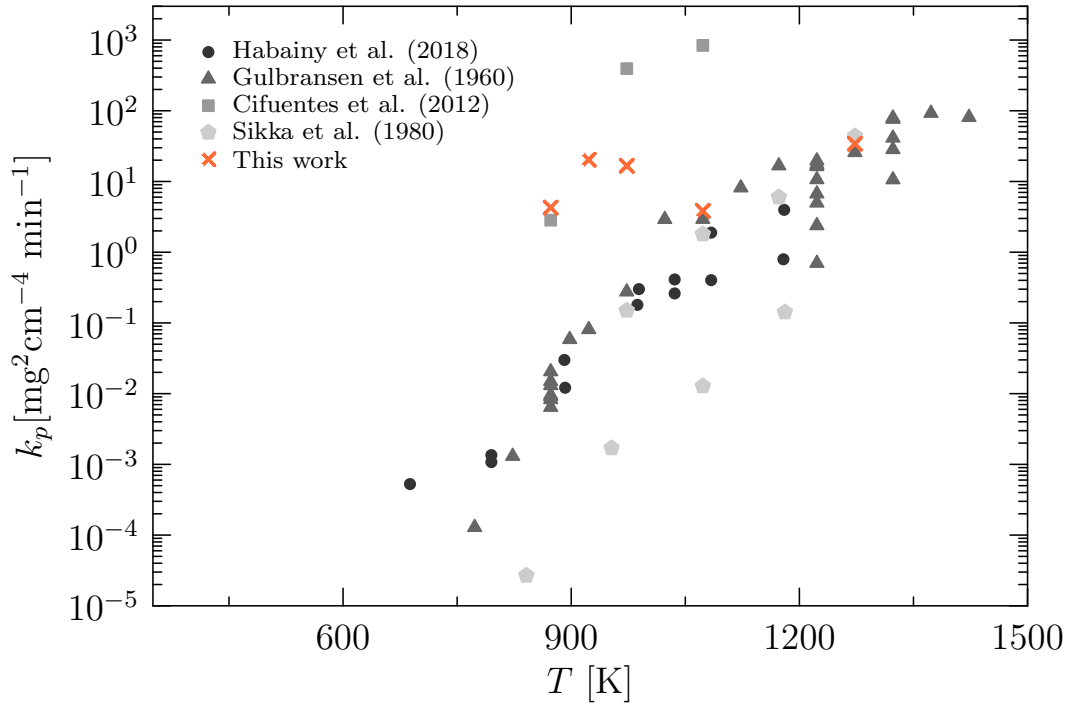
Figure 3.6: Parabolic growth constant as a function of temperature from a set of experimental data and as obtained in this work. Experimental data from Habainy et al. (2018) [15], Gulbransen et al. (1960) [14], Cifuentes et al. (2012) [7], and Sikka et al. (1980) [41].

3.5 Conclusions

We finalize with our main conclusions:

1. We have developed an interface-tracking model to simulate the kinetic evolution of multiple tungsten oxide layers. The model is consistent with the observed equilibrium oxide phases in the W-O phase diagram, and uses the diffusivities as the only material constants. The model is solved in space and time by adopting a finite-difference approach in one dimension with length and time increments of 1 nm and 1 ns, respectively.

2. We have parameterized the model using diffusivities both from experimental and computational sources. Due to the lack of available information for the diffusivity of oxygen

in WO_2, we have carried out a series of DFT calculations to calculate the migration energy and diffusion pre-factor of oxygen in WO_2 by a vacancy mechanism.

3. We consider only the protective growth stage of the oxide, before the critical fragmentation thickness is reached and the oxide layers begin to fail. This stage is believed to be captured by so-called 'parabolic' growth behavior, while after cracking growth is generally characterized by linear time kinetics.

4. The time evolution of the oxide scale matches parabolic growth only at high temperatures and when only one oxide sublayer is involved. Whenever multiple layers are at play, measurable deviations from parabolic growth can be appreciated.

5. The calculated values for the mass gain proportionality constant are in reasonable agreement with experimental measurements from several independent data sources. This adds validity to the model, particularly since the model is not fitted to experimental results *a posteriori.*

3.6   Summary of properties and evolution of tungsten oxides

3.6.1   Brief description of tungsten oxide phases

During oxidation of W, several different oxides may form. WO_3 is the most stable oxide, and at ambient temperature and pressure it displays a monoclinic structure consisting of a network of WO_6 octahedra (γ-WO_3). Above 330°C, WO_3 is seen to transform into an orthorhombic structure (β-WO_3), and tetragonal above 740°C (α-WO_3) [9]. WO_2 has a monoclinic structure in ambient conditions, and an orthorhombic structure at high temperatures and pressures. The crystal structure of monoclinic WO_2 also consists of WO_6 octahedra but with the difference that the octahedra in WO_2 are edge-shared while they are corner-shared in WO_3 [26]. Between WO_3 and WO_2, the stoichiometric oxides $W_{18}O_{49}$ ($WO_{2.9}$), $W_{24}O_{68}$ ($WO_{2.72}$) have been reported at temperatures of 485°C and above [12, 51].

The intermediate phases $W_{18}O_{49}$ and $W_{24}O_{68}$ form due to the thermal stabilization of distorted arrangements of the WO_6 octahedra [36, 40, 44]. As the amount of chemical oxygen decreases, the usual corner-sharing arrangement of octahedra is partially replaced by groups of edge-sharing octahedra, which form pockets of shear planes. This is due to the tendency lattice to eliminate single oxygen vacancies by a crystallographic shear process [40, 44]. When these shears become coordinated, new stoichiometric lattices can form, e.g., $WO_{2.9}$ and $WO_{2.72}$. However, as revealed by the W-O phase diagram shown in Figure 3.1a [12], these phases have very narrow stability ranges close to the theoretical stoichiometry values. Interestingly, each phase is characterized by a distinctive color, as shown in Figure 3.1b, associated with the optical diffraction of the different octahedral arrangements.

3.6.2 Extraction of parabolic-to-linear transition thicknesses from tabulated experimental observations

To extract the critical scale thicknesses at which a transition from parabolic (protective layer) to linear (loss of protective layer) growth, we resort to the tabulated data given by Gulbransen *et al.* [14] in a series of oxidation experiments at several temperatures and different oxygen atmospheres. The data are listed in Table 3.4 (units from the original paper have been updated to more current usage). The presumed phase is inferred from the observed color and the oxygen concentration (high O concentrations favoring WO_3 and low ones favoring WO_2). The oxide scale thickness at which a deviation from parabolic growth is observed is marked as the value of w^* to be used in the simulations.

3.7 Derivation of the Stefan equation

Mass conservation dictates that a discontinuity in the first derivative of the concentration at an interface, i.e., different arriving and exiting oxygen ion fluxes, must be compensated by a moving interface. The rationale for such motion is provided by the conservation of the

Table 3.4: Transition oxide layer thickness calculated as a function of temperature at an O_2 partial pressure of 0.1 atm (adapted from ref. [14]). The observed color and presumed oxide phase are also included. The presumed phase is inferred from the observed color and the oxygen concentration (high O concentrations favoring WO_3 and low ones favoring WO_2). The mass density of metallic W is 19.3 g·cm^{-3}, which amounts to an atomic concentration of 6.3×10^{28} per m^3

T [°C]	w^* [μm]	observed surface color	presumed oxide
600	52	blue black	$WO_{2.72}/WO_2$
625	77	black with yellow spots	WO_3/WO_2
650	100	blue black with yellow covering	$WO_3/WO_{2.72}/WO_2$
700	155	blue black	$WO_{2.72}/WO_2$
750	181	black	WO_2
800	207	black	WO_2
850	310	black	WO_2
900	310	blue black	$WO_{2.72}/WO_2$
950	340	black	WO_2
1000	360	black	WO_2
1050	360	black	WO_2
1100	390	yellow black	WO_3/WO_2

total oxygen concentration at the interface, which includes chemical oxygen (in the form of stoichiometric oxide phases) and free oxygen (free to diffuse through the crystal structure). At a given interface with a total area A, the amount of oxygen ions arriving per unit time from the left (negative side of the interface):

$$J_{int}^- A$$

The amount of oxygen ions exiting that same interface is:

$$J_{int}^+ A$$

When both fluxes are equal, the interface is in equilibrium and does not move. However, if the the exiting flux is larger than the arriving flux, the interface must move lest there is a depletion in the total oxygen content. Such a gap must be filled by taking some of the exiting (free) oxygen and immobilizing it as chemical oxygen, i.e., growing the oxide layer. For a specific oxide phase with an oxygen-to-metal ratio of n, the number of oxygen ions needed to grow that phase by a thickness s is:

$$(sA)(n\rho_W)$$

with the term (sA) indicating the volume of the new phase, and the term $(n\rho_W)$ indicating the number of oxygen ions per unit volume needed to create the oxide phase. The rate form of the above expression is trivially:

$$\dot{s}An\rho_W$$

such that the excess flux exiting the interface is immobilized as stoichiometric oxygen. The balance equation is:

$$J_{int}^- A = J_{int}^+ A - \dot{s}An\rho_W \tag{3.13}$$

which, after rearranging and eliminating the variable A becomes:

$$\dot{s} = \frac{J_{int}^+ - J_{int}^-}{n\rho_W} \tag{3.14}$$

3.8 References

[1] https://www.engineeringtoolbox.com/molecular-mass-air-d_679.html.

[2] Abdullah Alkhamees, Yue-Lin Liu, Hong-Bo Zhou, Shuo Jin, Ying Zhang, and Guang-Hong Lu. First-principles investigation on dissolution and diffusion of oxygen in tungsten. *Journal of Nuclear Materials*, 393(3):508–512, 2009.

[3] Asghar Aryanfar, William Goddard III, and Jaime Marian. Constriction percolation model for coupled diffusion-reaction corrosion of zirconium in pwr. *Corrosion Science*, 158:108058, 2019.

[4] R Aymar, P Barabaschi, and Y Shimomura. The iter design. *Plasma physics and controlled fusion*, 44(5):519, 2002.

[5] A Calvo, K Schlueter, E Tejado, G Pintsuk, N Ordás, I Iturriza, R Neu, JY Pastor, and C García-Rosales. Self-passivating tungsten alloys of the system w-cr-y for high temperature applications. *International Journal of Refractory Metals and Hard Materials*, 73:29–37, 2018.

[6] Juan Chen. Calculations of vacancy diffusivity in wo3. 2020.

[7] Sandra C Cifuentes, MA Monge, and P Pérez. On the oxidation mechanism of pure tungsten in the temperature range 600–800 c. *Corrosion Science*, 57:114–121, 2012.

[8] L EL-GUEBALY, C Latgé, F Dacquait, A AERTS, A BARON-WIECHEC, A BO-JANOWSKA, I CRISTESCU, U FISCHER, S FUKADA, M GARCIA, et al. Overview of coolant characteristics under irradiation: Radiation-chemistry, radiolysis, activation, and their consequences on operation, maintenance, and decommissioning. *IAEA TEC-DOC SERIES*, page 26, 2020.

[9] A Faudoa-Arzate, A Arteaga-Durán, RJ Saenz-Hernández, ME Botello-Zubiate, PR Realyvazquez-Guevara, and JA Matutes-Aquino. Hrtem microstructural characterization of β-wo3 thin films deposited by reactive rf magnetron sputtering. *Materials*, 10(2):200, 2017.

[10] G Federici, R Kemp, D Ward, C Bachmann, T Franke, S Gonzalez, C Lowry, M Gadomska, J Harman, B Meszaros, et al. Overview of eu demo design and r&d activities. *Fusion Engineering and Design*, 89(7-8):882–889, 2014.

[11] Tao Fu, Kunkun Cui, Yingyi Zhang, Jie Wang, Fuqiang Shen, Laihao Yu, Junmao Qie, et al. Oxidation protection of tungsten alloys for nuclear fusion applications: A comprehensive review. *Journal of Alloys and Compounds*, 884:161057, 2021.

[12] Michael Gasik. *Handbook of ferroalloys: theory and technology.* Butterworth-Heinemann, 2013.

[13] Robert Gomer and JK Hulm. Adsorption and diffusion of oxygen on tungsten. *The Journal of Chemical Physics*, 27(6):1363–1376, 1957.

[14] EA Gulbransen and KF Andrew. Kinetics of the oxidation of pure tungsten from 500 to 1300 c. *Journal of the Electrochemical Society*, 107(7):619, 1960.

[15] Jemila Habainy, Srinivasan Iyengar, Kumar Babu Surreddi, Yongjoong Lee, and Yong Dai. Formation of oxide layers on tungsten at low oxygen partial pressures. *Journal of Nuclear Materials*, 506:26–34, 2018.

[16] T Hirai, G Pintsuk, J Linke, and M Batilliot. Cracking failure study of iter-reference tungsten grade under single pulse thermal shock loads at elevated temperatures. *Journal of Nuclear Materials*, 390:751–754, 2009.

[17] Takeshi Hirai, S Panayotis, V Barabash, Claude Amzallag, F Escourbiac, A Durocher,

Mario Merola, Jochen Linke, Th Loewenhoff, Gerald Pintsuk, et al. Use of tungsten material for the iter divertor. *Nuclear Materials and Energy*, 9:616–622, 2016.

[18] F Klein, T Wegener, A Litnovsky, M Rasinski, XY Tan, J Gonzalez-Julian, J Schmitz, M Bram, JW Coenen, and Ch Linsmeier. Oxidation resistance of bulk plasma-facing tungsten alloys. *Nuclear materials and energy*, 15:226–231, 2018.

[19] Felix Klein, Andrey Litnovsky, Tobias Wegener, Xiaoyue Tan, Jesus Gonzalez-Julian, Marcin Rasinski, Janina Schmitz, Christian Linsmeier, Martin Bram, and Jan Willem Coenen. Sublimation of advanced tungsten alloys under demo relevant accidental conditions. *Fusion engineering and design*, 146:1198–1202, 2019.

[20] LT Kong and Laurent J Lewis. Transition state theory of the preexponential factors for self-diffusion on cu, ag, and ni surfaces. *Physical Review B*, 74(7):073412, 2006.

[21] C Lambert-Mauriat and V Oison. Density-functional study of oxygen vacancies in monoclinic tungsten oxide. *Journal of Physics: Condensed Matter*, 18(31):7361, 2006.

[22] Caroline Lambert-Mauriat, Vincent Oison, Lama Saadi, and Khalifa Aguir. Ab initio study of oxygen point defects on tungsten trioxide surface. *Surface science*, 606(1-2): 40–45, 2012.

[23] Erik Lassner and Wolf-Dieter Schubert. Important aspects of tungsten chemistry. In *Tungsten*, pages 85–132. Springer, 1999.

[24] Hung M. Le, Nam H. Vu, and Bach-Thang Phan. Migrations of oxygen vacancy in tungsten oxide (wo3): A density functional theory study. *Computational Materials Science*, 90:171–176, 2014.

[25] Hung M Le, Nam H Vu, and Bach-Thang Phan. Migrations of oxygen vacancy in tungsten oxide (wo3): A density functional theory study. *Computational materials science*, 90:171–176, 2014.

[26] C Linderalv. Structural and thermodynamical properties of tungsten oxides from first-principles calculations. Master's thesis, Chalmers University of Technology, 2016.

[27] A Litnovsky, T Wegener, F Klein, Ch Linsmeier, M Rasinski, A Kreter, X Tan, J Schmitz, JW Coenen, Y Mao, et al. New oxidation-resistant tungsten alloys for use in the nuclear fusion reactors. *Physica Scripta*, 2017(T170):014012, 2017.

[28] D Maisonnier, I Cook, Sardain Pierre, Boccaccini Lorenzo, Bogusch Edgar, Broden Karin, Forrest Robin, Giancarli Luciano, Hermsmeyer Stephan, Nardi Claudio, et al. The european power plant conceptual study. *Fusion Engineering and Design*, 75:1173–1179, 2005.

[29] David Maisonnier, Iau Cook, Sardain Pierre, Boccaccini Lorenzo, Giancarli Luciano, Norajitra Prachai, Pizzuto Aldo, PPCS Team, et al. Demo and fusion power plant conceptual studies in europe. *Fusion Engineering and Design*, 81(8-14):1123–1130, 2006.

[30] Cezarina C Mardare and Achim W Hassel. Review on the versatility of tungsten oxide coatings. *physica status solidi (a)*, 216(12):1900047, 2019.

[31] Mathias Mews, Lars Korte, and Bernd Rech. Oxygen vacancies in tungsten oxide and their influence on tungsten oxide/silicon heterojunction solar cells. *Solar Energy Materials and Solar Cells*, 158:77–83, 2016.

[32] RG Musket. Room-temperature adsorption of oxygen on tungsten surfaces: A review. *Journal of the Less Common Metals*, 22(2):175–191, 1970.

[33] Dóra Nagy and Samuel A Humphry-Baker. An oxidation mechanism map for tungsten. *Scripta Materialia*, 209:114373, 2022.

[34] Christopher Nilsson and Jemila Habainy. Oxidation of pure tungsten in the temperature interval 400 to 900 c. *Diploma work*, 2013.

[35] NA North, Ian Donald MacLeod, and C Pearson. *Corrosion of metals*. Butterworth-Heinemann, 1987.

[36] R Pickering and RJD Tilley. An electron microscope study of tungsten oxides in the composition range wo$_{2.9}$-wo$_{2.72}$. *Journal of Solid State Chemistry*, 16(3-4):247–255, 1976.

[37] Michael Reyes, Asghar Aryanfar, Sun Woong Baek, and Jaime Marian. Multilayer interface tracking model of zirconium clad oxidation. *Journal of Nuclear Materials*, 509:550–565, 2018.

[38] M Rieth, Sergei L Dudarev, SM Gonzalez De Vicente, J Aktaa, T Ahlgren, S Antusch, DEJ Armstrong, M Balden, Nadine Baluc, M-F Barthe, et al. Recent progress in research on tungsten materials for nuclear fusion applications in europe. *Journal of Nuclear Materials*, 432(1-3):482–500, 2013.

[39] John Christopher Scully. *Fundamentals of corrosion*. Pergamon Press Inc., Elmsford, NY, 1975.

[40] Alexander Shengelaya, Fabio La Mattina, and Kazimierz Conder. Unconventional transport properties of reduced tungsten oxide wo2. 9. *Condensed Matter*, 5(4):63, 2020.

[41] VK Sikka and CJ Rosa. The oxidation kinetics of tungsten and the determination of oxygen diffusion coefficient in tungsten trioxide. *Corrosion Science*, 20(11-12):1201–1219, 1980.

[42] JH Singleton. Adsorption of oxygen on tungsten at temperatures from 300° to 850° k. *The Journal of Chemical Physics*, 47(1):73–82, 1967.

[43] GR Smolik, SJ Piet, and RM Neilson Jr. Predictions of radioactive tungsten release for hypothetical iter accidents. *Fusion Technology*, 19(3P2B):1398–1402, 1991.

[44] RJD Tilley. The crystal chemistry of the higher tungsten oxides. *The chemistry of non-sag tungsten*, pages 93–109, 1995.

[45] Maanas Togaru, Rajat Sainju, Lichun Zhang, Weilin Jiang, and Yuanyuan Zhu. Direct observation of tungsten oxidation studied by in situ environmental tem. *Materials Characterization*, 174:111016, 2021.

[46] K Tomabechi, JR Gilleland, Yu A Sokolov, R Toschi, ITER Team, et al. Iter conceptual design. *Nuclear Fusion*, 31(6):1135, 1991.

[47] DR Uhlmann, H Kent Bowen, and WD Kingery. Introduction to ceramics, 1976.

[48] Haitao Wang, Yibin Xu, Masahiro Goto, Yoshihisa Tanaka, Masayoshi Yamazaki, Akira Kasahara, and Masahiro Tosa. Thermal conductivity measurement of tungsten oxide nanoscale thin films. *Materials transactions*, 47(8):1894–1897, 2006.

[49] Wennie Wang, Anderson Janotti, and Chris G Van de Walle. Role of oxygen vacancies in crystalline wo 3. *Journal of Materials Chemistry C*, 4(27):6641–6648, 2016.

[50] Matthias Weil and Wolf-Dieter Schubert. The beautiful colours of tungsten oxides. *International Tungsten Industry Association: London, UK*, pages 1–9, 2013.

[51] HA Wriedt. The ow (oxygen-tungsten) system. *Bulletin of Alloy phase diagrams*, 10 (4):368–384, 1989.

[52] David John Young. *High temperature oxidation and corrosion of metals*, volume 1. Elsevier, 2008.

[53] Yue Zhao, Lucile Dezerald, and Jaime Marian. Electronic structure calculations of oxygen atom transport energetics in the presence of screw dislocations in tungsten. *Metals*, 9(2):252, 2019.

CHAPTER 4

Reaction Rates for 1D-motion Particles

4.1   Introduction

Accurately accounting for the fate of irradiation species, such as vacancies, self-interstitial atoms (SIA) and clusters thereof, is of extraordinary importance to predict damage accumulation and its derivative effects, such as hardening, swelling, and/or creep. One of the fundamental pillars that the theory of irradiation damage rests on is defect diffusion[15, 24, 35], as it controls how defects migrate, react, and reach defect sinks, which over long time scales results in microstructural evolution. While a complete theory of irradiation damage is still lacking, it is now recognized that physical models such as the *production* [44] and *dislocation* bias models [10, 21] are crucial in order to understand many aspects of irradiation damage in crystalline materials. From this understanding, a picture has emerged whereby it is well accepted that (i) self-interstitial clusters are produced directly within displacement cascades [41] and (ii) these clusters diffuse athermally in a one-dimensional fashion, with long unidirectional random walks punctuated by sporadic changes in direction that become less frequent as the clusters grow larger [2, 12, 28, 38, 45]. In particular, molecular dynamics simulations of displacement cascades in atomistic systems have played a key role in establishing several of these features with certainty [1].

Knowledge of the character of the diffusivity (as well as of its magnitude) enters kinetic transport models derived from the Becker-Döring formalism based on classical nucleation theory [5, 31, 40]. These models, which in their simplest form have come to be known as

mean field rate theory models, make use of kinetic coefficients where this information is input [3, 4, 16, 17, 25, 27, 29, 30, 39]. However, despite several decades after the formulation of the production and dislocation bias models and the role played by fast 1D-moving species such as SIA clusters, most of these methods continue to rely on three-dimensional descriptions of these kinetic coefficients based on diffusion theory. In particular, the existence of 3D and 1D moving species requires that kinetic coefficients be derived for all possible combination reactions, *i.e.* 3D+3D, 3D+1D, 1D+1D. Of these, the 3D+3D case is of course described by the venerable solution for the rate of *coagulation* of two populations in steady state by Smoluchowski [37]. Solutions for the reaction rate of particles in 1D were also proposed going back to the 1970s [2, 18, 19, 20, 22], but we must differentiate between these and solutions for one-dimensionally moving particles in 3D space (as considered, e.g., in refs. [13]). Recent efforts aimed at providing solutions for 3D+1D and 1D+1D cases rely on approximations that, while reasonable in many situations, require monitoring the kinetic state of a system to ascertain their validity. For example, Kohnert and Wirth [26] adopt the adiabatic approximation for the 3D+1D case, whereby 3D-moving species diffusing much slower than their 1D counterparts are treated as stationary species to compute the effective reaction rate. The 1D+1D case was discarded altogether as having too low a reaction cross section to be quantitatively relevant[1]. Dunn *et* al. have also resorted to a stationary approach to derive coefficients for the reaction rates in the 3D+1D and 1D+1D cases [14].

The other element needed to close the system of kinetic equations of an irradiated system is the definition of the sink strengths that describe the defect absorption propensity of several microstructural features. These may include voids, precipitates, dislocations, free surfaces, and/or grain boundaries. The standard solutions used for 3D species are based on the work by Brailsford, Bullough, and co-workers [7, 8, 9], while Borodin [6] has generalized them to anisotropic diffusion and one-dimensional defect transport. In this paper, we provide closed-form solutions to the rate coefficients for 1D+1D reactions (understood to take place

---

[1]We will show later that this is not necessarily the case in certain particle concentration regimes.

in a three-dimensional setting) and sink strengths of 1D diffusers for intrinsic and extrinsic spherical sinks (precipitates and grain boundaries), line sinks (dislocations) and surface sinks (thin films). Our objective is to employ these in kinetic models of damage evolution to account for the effect of dimensionality in irradiation species transport, as others have recently attempted to do [14, 26]. Our approach is to derive analytical expressions for each coefficients using the correct geometric setting and verify these numerically using equivalent kinetic Monte Carlo (kMC) simulations. We obtain these coefficients under stationary conditions such that they can be inserted into rate theory formulations in a straightforward manner.

Our paper is organized as follows. First we briefly describe the method utilized to arrive at the analytical solutions and the kMC simulation setup. In Sec. 4.2 we derive the expressions for the reaction rates of two one-dimensionally moving objects in 3D, and describe the numerical verification approach. We then in Sec. 4.3 derive the sink strengths for 1D-moving species for the standard cases enumerated above. We finalize with a brief discussion and the conclusions.

The mathematical problem to solve here is (i) the calculation of the rate of coagulation between two one-dimensionally moving objects in 3D, and (ii) the rate of absorption of one-dimensionally moving particles by sinks. To that end, we consider a continuum medium with an initial particle concentration of C_∞ as represented in Figure 4.1a. kMC simulations are carried out replicating the corresponding geometry and boundary conditions in each case by following these general guidelines, represented in flowchart format in Figure 4.1b.

i Consider a material volume V and two particles of sizes R_1 and R_2 moving one-dimensionally along random directions with diffusivity coefficients D_1 and D_2. To the extent that it is possible the finite volume is always chosen to be cubic, with side length L, or spherical, with diameter d.

ii The number of particles of each type in the simulation is always limited to one, such
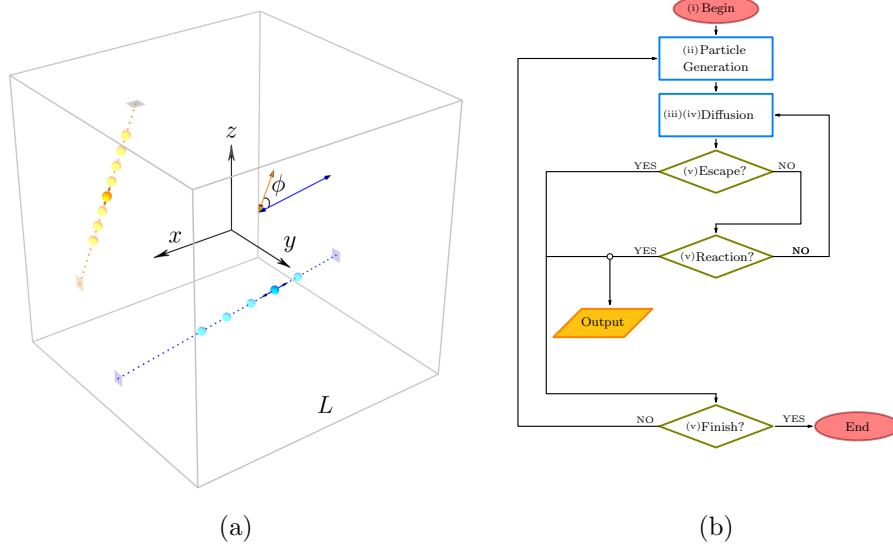
Figure 4.1: KMC simulations of two 1D-diffusing particles. (a) Simulation box used in the kMC simulations. Each particle's trajectory is highlighted using dashed lines. ϕ is the angle formed by the two diffusion directions. (b) Flow chart of the kMC procedure with matching step designators as given in the text.

the the corresponding particle concentration is always the inverse of the cell volume, i.e. $C = L^{-3}$ or $C = \frac{3}{4\pi} R^{-3}$.

iii Each particle is made to move along a randomly generated one dimensional trajectory, by sampling the polar and azimuth angles independently from a uniform angular distribution in the intervals $[0, \pi]$ and $[0, 2\pi]$, respectively.

iv A potential move along each trajectory is generated by randomly choosing a direction and considering a displacement of $\delta l = b$, where b is the first nearest neighbor distance. The jump rate of the particle is $r_{1D} = \frac{D}{2\delta l^2}$, where D is the corresponding particle diffusivity. A move is randomly selected with the appropriate probability and time is advanced as $\delta t = -\frac{\ln \xi}{2r_{1D}}$, where ξ is a uniform random number in the $(0, 1]$ interval.

v This process is repeated until the two particles are within a distance $(R_1 + R_2)$ of one another inside the simulation volume, or when one of the particles exits the simulation volume. In either case, the simulation is terminated and a new pair of particles are introduced in the kMC cell. The aggregate time, however, is not reset to zero: time is advanced regardless of the outcome of the two-particle simulation.

In all cases shown in this paper we use $D = 2.45 \times 10^{-7}$ cm^2·s^{-1} as a realistic atom diffusivity at low temperatures in metals [23]. R_1 and R_2 are 0.15 nm, while $b = 0.3$ nm.

4.2 Reaction rates of one-dimensionally-migrating species

4.2.1 Reaction rate for one-dimensionally moving particles following parallel trajectories

It is helpful to first study the two extreme cases of parallel and perpendicular trajectories. We first consider two particles moving along parallel directions with diffusivity coefficients D_1 and D_2. In such case, one can resort to relative motion and fix one of the particles at the
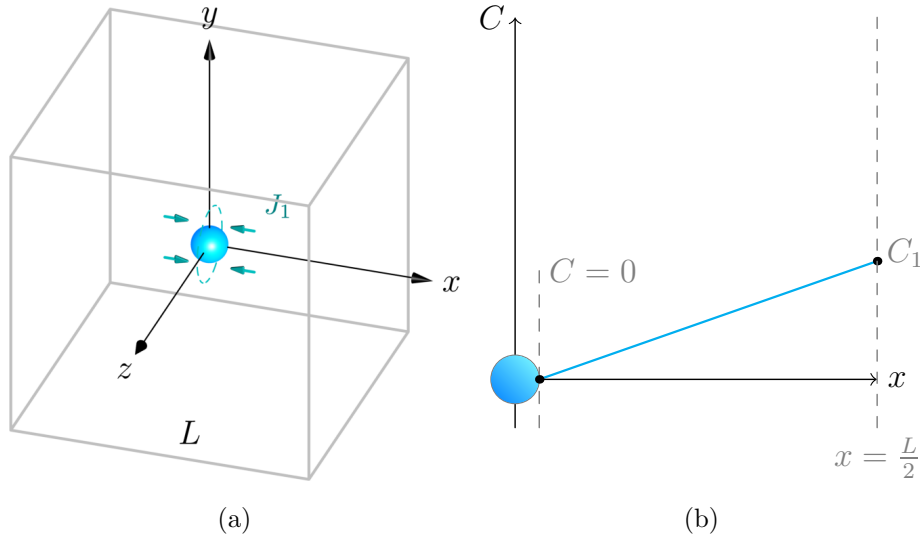
Figure 4.2: Model for particles with parallel trajectories. (a) Particle 2 is fixed at the origin of sample box while particle 1 diffuses along the x axis. (b) Concentration profile of particle 1 in the box.

origin while the other moves with diffusivity $(D_1 + D_2)$ in one dimension. In such case, the problem reduces to finding the steady state concentration in a cubic representative volume element with volume $V = L^3$, as shown in Figure 4.2.

The steady state solution of the concentration of moving particles is obtained by solving Fick's second law under stationary conditions:

$$(D_1 + D_2)\frac{\partial^2 C_1}{\partial x^2} = 0. \tag{4.1}$$

The solution to this equation is a linear profile $C_1 = ax + b$ where the constants a and b are obtained by considering the boundary conditions:

$$\text{At } x = R, C_1 = 0$$
$$\text{At } x = \tfrac{L}{2}, C_1 = C_\infty$$

which results in:F

$$C_1(x) = \frac{C_\infty}{\frac{L}{2} - R}(x - R) \tag{4.2}$$

55

This results in a particle flux equal to:

$$J_1 = -(D_1 + D_2)\frac{dC_1(x)}{dx} = -(D_1 + D_2)\frac{C_\infty}{\frac{L}{2} - R} \tag{4.3}$$

From this, one can calculate the particle current M_1 arriving at particle 2:

$$M_1 = J_1 \cdot \pi R^2 = (D_1 + D_2)\frac{2\pi R^2 C_\infty}{\frac{L}{2} - R}. \tag{4.4}$$

which, assuming $L \gg R$, leads to:

$$M_1 = \frac{4\pi(D_1 + D_2)(R_1 + R_2)^2 C_\infty}{L} \tag{4.5}$$

where R has been replaced with the sum of the sizes of both particles and the minus sign in eq. (4.3) has been removed by disregarding for convenience the vectorial nature of the flux. Multiplying the above expression times C_2 gives the coagulation rate per unit volume of particles 1 and 2. Moreover, since in the present setting $C_\infty \equiv C_1$ and $C_2 = L^{-3}$, eq. (4.5) reduces to:

$$r_{\mathrm{par}} = 4\pi(R_1 + R_2)^2(D_1 + D_2)C_1 C_2^{\frac{4}{3}}. \tag{4.6}$$

The above solution is checked against numerical simulations using kMC in the geometry shown in Figure 4.2a. The results are shown in Figure 4.3, where, after a certain transient, the numerical simulations are seen to converge to the steady state analytical solution given in eq. (4.6) for a number of different domain sizes.

When there are two particles moving in perpendicular directions things get a little different but can also be solved by the same steps.

4.2.2 Reaction rate for one-dimensionally moving particles following perpendicular trajectories

Next we study the case of one-dimensionally diffusing particles following perpendicular trajectories. In this case we solve Fick's 2nd law in steady state conditions using cylindrical

56
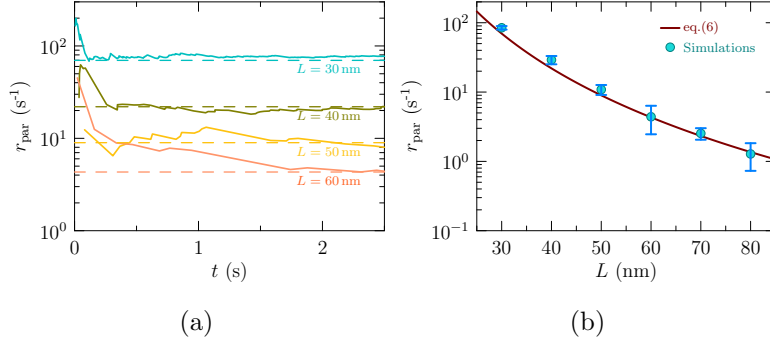
Figure 4.3: Comparison between kMC simulations and eq. (4.6) for 1D-diffusing particles moving on parallel trajectories. (a) Time evolution of the reaction rate for several domain sizes. (b) Time-converged reaction rates as a function of domain size.

coordinates with effective diffusivity $\frac{D_1 + D_2}{2}$ [2]:

$$\frac{D_1 + D_2}{2r} \frac{d}{dr}\left(r\frac{dC_1}{dr}\right) = 0 \tag{4.7}$$

The solution to the above expression is:

$$C_1(r) = a\ln r + b \tag{4.8}$$

subjected to identical boundary conditions as the parallel case:

At $r = R$, $C_1 = 0$

At $r = \frac{L}{2}$, $C_1 = C_\infty$

from which:

$$C_1(r) = \frac{C_\infty}{\ln\frac{L}{2R}}\left(\ln r - \ln R\right) \tag{4.9}$$

The corresponding net flux becomes:

$$J_1 = \frac{D_1 + D_2}{2}\frac{dC_1}{dr}\bigg|_{r=R} = \frac{D_1 + D_2}{2}\frac{C_\infty}{R\ln\frac{L}{2R}}. \tag{4.10}$$

---

[2]This is easy to show by considering the motion of one particle relative to the motion of the other, as proved in (see proof in Appendix 4.5).
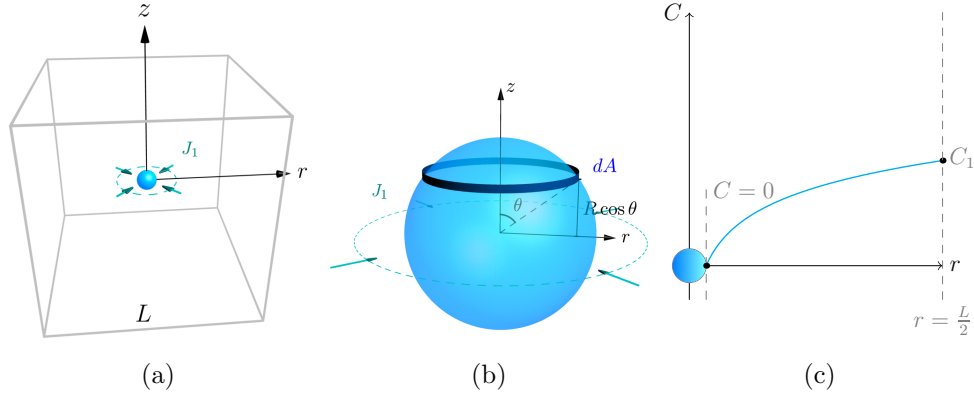
Figure 4.4: Model for particles with perpendicular trajectories. (a) Particle 2 is fixed at the center of box while particle 1 diffuses along the r direction. (b) Illustration of differential of area dA for integration of the particle flux. (c) Concentration profile of particle 1 in the box.

As above, we can write the expression for the particle current at particle 2 assuming that $R = R_1 + R_2$:

$$M_1 = \int_A J dA = \frac{D_1 + D_2}{2} \int_A \frac{C_\infty}{R' \ln \frac{L}{2R'}} dA \tag{4.11}$$

In this case the contact area dA is not constant, as it was for the case of parallel trajectories, but changes with the intersection plane conformed by particle 1's trajectory and the sphere representing particle 2 (cf. Figure 4.4b), i.e.:

$$dA = 2\pi R' d(R\cos\theta) = 2\pi R \sin\theta d(R\cos\theta)$$

with $R' = R\sin\theta$. Consequently, eq. (4.11) is written as:

$$M_1 = 2\pi R(D_1 + D_2)C_\infty \int_0^1 \frac{d(\cos\theta)}{\ln \frac{L}{2R\sin\theta}} \tag{4.12}$$

The above integral is challenging to solve analytically. However, the integrand in the equation can be simplified by assuming that the logarithmic term varies slowly compared to the numerator of the integral. This implies that $\ln(L/2R\sin\theta) \approx \ln(L/2R)$, and thus:

$$M_1 = \frac{2\pi R(D_1 + D_2)C_\infty}{\ln \frac{L}{2R}} \tag{4.13}$$

58
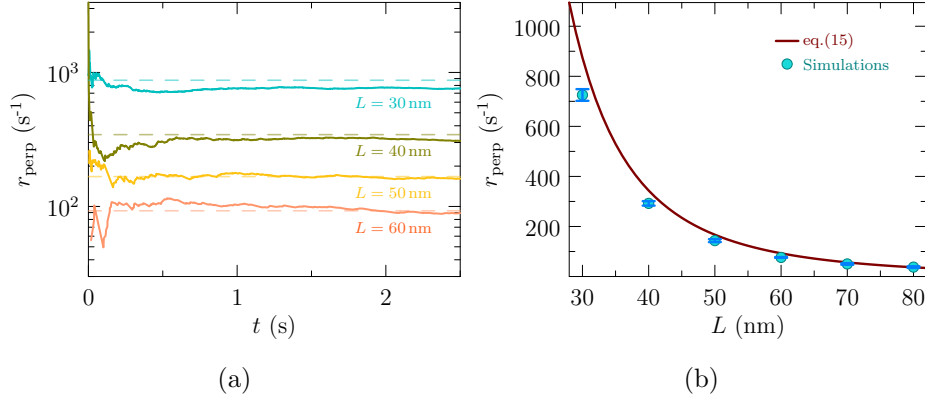
Figure 4.5: Comparison between kMC simulations of 1D-moving particles following perpendicular trajectories and eq. (4.15).(a)Simulations are approaching analytical results as time t goes by; (b)trend of eq. (4.15) with different simulation volume dimension L, consists with simulations

As for the parallel case, the coagulation rate is obtained by making $C_\infty \equiv C_1$ and multiplying the particle current times C_2:

$$r_{\text{perp}} = \frac{2\pi R(D_1 + D_2)C_1 C_2}{\ln \frac{L}{2R}} \tag{4.14}$$

and using $C_2 = L^{-3}$ we arrive at the final expression for the scale-free steady state coagulation rate of two particles moving one-dimensionally along perpendicular trajectories:

$$r_{\text{perp}} = \frac{2\pi R(D_1 + D_2)C_1 C_2}{\ln \frac{C_2^{-1/3}}{2(R_1 + R_2)}} \tag{4.15}$$

A comparison between the predictions from eq. (4.15) and the corresponding numerical simulations is given in Figure 4.5, where good convergence is shown after a short transient in the numerical simulations, therefore validating our analytical expression.

4.2.3 General reaction rate for one-dimensionally moving species with arbitrary trajectories

Obtaining the general expression for the reaction rate of two unidimensionally-moving species (in 3D space) with trajectories forming an angle ϕ and concentrations C_1 and C_2 is straightforwardly obtained from eqs. (4.6) and (4.15) as:

$$
\begin{aligned}
r_\phi &= r_{\mathrm{par}} \cos \phi + r_{\mathrm{perp}} \sin \phi = \\
&= 2\pi \left(R_1 + R_2\right) \left(D_1 + D_2\right) \left[2\left(R_1 + R_2\right) C_2^{1/3} \cos \phi + \frac{1}{\ln \frac{C_2^{-1/3}}{2(R_1+R_2)}} \sin \phi \right] C_1 C_2 (4.16)
\end{aligned}
$$

This expression has also been verified numerically using kMC simulations, as shown in Figure 4.6 Finally, to get a mean-field expression that can be directly used in rate theory calculations, independent of ϕ, we propose to use the angle-averaged version of eq. (4.16):

$$
\begin{aligned}
r_{\text{1D-1D}} &= \frac{1}{\pi/2} \int_0^{\pi/2} r_\phi d\phi = \\
&= 8\left(R_1 + R_2\right)\left(D_1 + D_2\right) \left[\left(R_1 + R_2\right) C_2^{1/3} + \frac{1}{2 \ln \frac{C_2^{-1/3}}{2(R_1+R_2)}} \right] C_1 C_2 \quad (4.17)
\end{aligned}
$$

where the term within the square brackets should be seen as a correction factor to the coagulation factor due to one-dimensional diffusion of both species involved.

4.3 Absorption rates of one-dimensionally moving particles at ideal sinks

As discussed in the introduction, the other element needed to characterize the kinetics of 1D-moving species is their interaction with ideal sinks. For this, one can follow the same approach as in the previous Section, i.e. the particle flux is determined by solving the diffusion equation along one dimension subjected to the boundary conditions prescribed by the

(a)
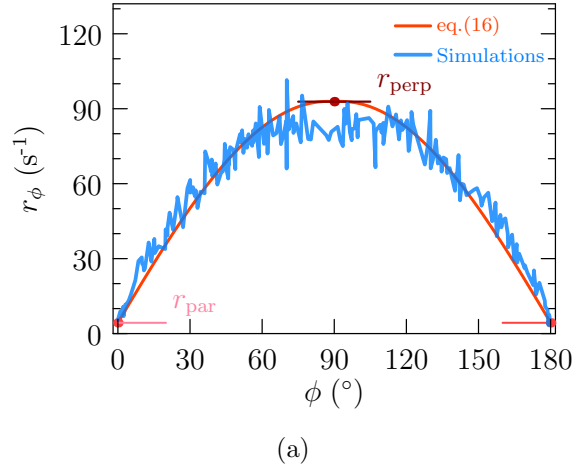
Figure 4.6: Comparison between kMC simulations of 1D-moving particles following trajectories forming an angle ϕ between them and eq. (4.16).

geometry of the particular sink type. Here we consider intrinsic and extrinsic spherical sinks, cylindrical sinks, and flat surfaces to represent grain boundaries, precipitates or inclusions, dislocations, and thin films, respectively. Images of the geometries considered in each case are shown in Figure 4.7.

4.3.1 Absorption rate at grain boundaries

A grain boundary is represented as a closed three dimensional surface, in the manner shown in Figure 4.7a. This implies solving the diffusion equation in one dimension:

$$\frac{\partial C}{\partial t} = D\frac{\partial^2 C}{\partial x^2}$$

with boundary conditions

$C = 0$ at $x = \pm\frac{L}{2}$

$C = C_\infty$ at $x = 0$

However, in this case, one must consider the continuity of the particle flux everywhere inside the sphere (the grain), which prevents us from solving the diffusion equation in steady state

61
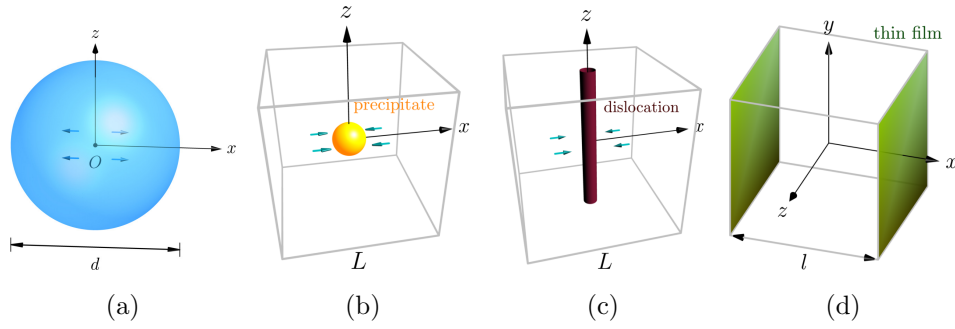
Figure 4.7: Geometries used to derive the absorption rate of 1D-moving particles at (a) grain boundaries, (b) precipitates, (c) dislocations, and (d) thin films.
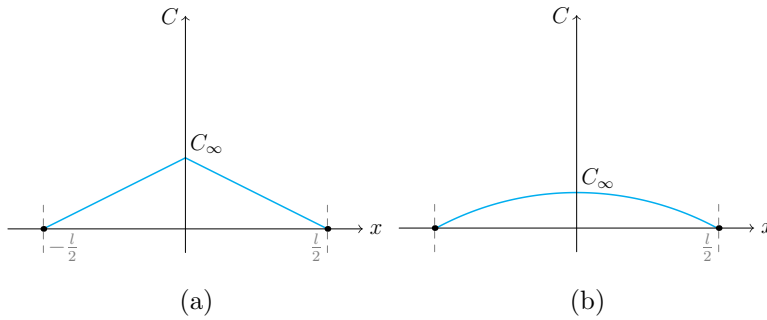
Figure 4.8: (a) Linear concentration profile inside a finite domain giving rise to a flux discontinuity at the origin. (b) The discontinuity is eliminated by considering an arc of constant curvature.

following the approach followed in Sec. 4.2.2 (corresponding to a linear concentration profile as shown in Figure 4.8a). A workaround is to solve:

$$D\frac{\partial^2 C}{\partial x^2} = \delta$$

with δ being an arbitrarily small constant ($\delta \to 0$). This, however, allows us to consider a concentration profile with constant curvature as Figure 4.8b shows.

Geometric inspection of this small arc of curvature, as shown in Figure 4.9a, reveals a series of equivalences that can be used to derive the particle flux. For example, assume that point A represents the concentration at the grain boundary, B is the concentration at the
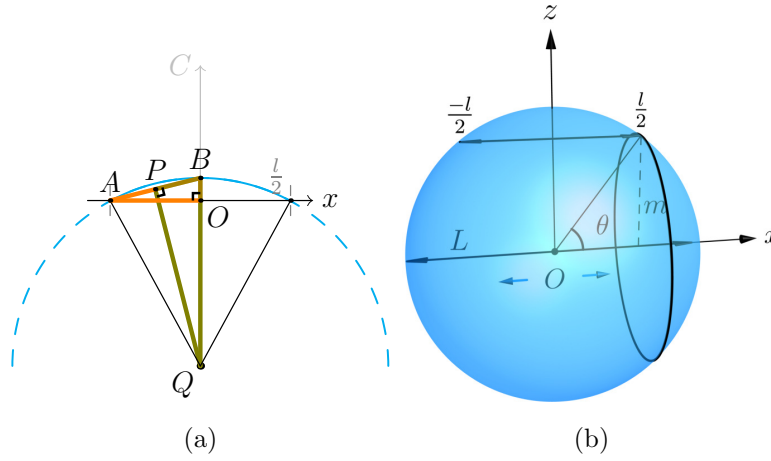
Figure 4.9: (a) Supporting geometry to determine the equation for the particle concentration from an arc of constant curvature. (b) Integration over the sphere's volume.

center, Q is the center of the circle containing the arc, and P is the midpoint of the segment $\overline{AB}$. From the figure, it can be seen that triangles $\triangle ABO$ and $\triangle QBP$ are similar triangles. From this, it can be readily seen that:

$$\frac{\overline{AB}}{\overline{BO}} = \frac{\overline{QB}}{\overline{BP}}$$

which can be rewritten as

$$\frac{\sqrt{\left(\frac{l}{2}\right)^2 + C_\infty^2}}{C_\infty} = \frac{R}{\frac{1}{2}\sqrt{\left(\frac{l}{2}\right)^2 + C_\infty^2}}$$

From this,

$$R = \frac{\left(\frac{l}{2}\right)^2 + C_\infty^2}{C_\infty^2}$$

and one arrives at the expression for the arc:

$$x^2 + [C + (R - C_\infty)]^2 = R^2$$

The flux can then be obtained as

$$J = -D\frac{dC}{dx} = -\frac{Dx}{C + (R - C_\infty)}$$

At endpoint A, $x = \pm\frac{l}{2}$, $C = 0$:

$$J_A = -\frac{Dl/2}{R - C_\infty} = -\frac{2D}{\frac{l/2}{C_\infty} - \frac{C_\infty}{l/2}} = -\frac{2D}{\frac{1}{\tan \angle ABO} - \tan \angle ABO}$$

Because the arc can have arbitrarily small curvature, $\tan \angle ABO \approx 0$, which results in:

$$J_A \approx -2D \tan \angle ABO = -\frac{4DC_\infty}{l} \tag{4.18}$$

The particle current is obtained by integrating J_A over the entire spherical surface S. This is done by considering parallel rings and sweeping along the Euler angle, as shown in Figure 4.9b:

$$
\begin{aligned}
M_{\text{gb}} &= \int_S J_A ds = \int_{-d/2}^{d/2} \frac{4DC_\infty}{l} 2\pi r dr = \int_0^\pi \frac{4DC_\infty}{2d\cos\theta}(2\pi d^2 \sin\theta \cos\theta)d\theta = \\
&= 4\pi DC_\infty d \int_0^\pi \sin\theta d\theta = 8\pi DC_\infty d \tag{4.19}
\end{aligned}
$$

where we have used $r = d\sin\theta$ and $l = 2d\cos\theta$. As above, the rate of absorption is obtained by making $C_1 \equiv C_\infty$ and multiplying M_{gb} times C_2:

$$r_{\text{gb}} = 8\pi DdC_1 C_2 = \frac{24D}{d^2}C_1 \tag{4.20}$$

where we have used $C_2 = \left(\frac{4\pi(d/2)^3}{3}\right)^{-1}$. This implies a sink strength $k_{\text{gb}}^2 = 24/d^2$. As Figure 4.10 shows, excellent agreement is found between this expression and kMC simulations of the equivalent spherical geometries.

4.3.2 Absorption by precipitates and dislocations

For absorption of one-dimensionally-moving particles at spherical precipitates, we refer this case back to the geometry displayed in Figure 4.11a, which shows that it is a particular case of the 1D-1D situation discussed in Sec. 4.2.1 with one of the particles being immobile. As above, the rate of absorption is obtained by making $C \equiv C_\infty$ and eliminating L in eq. (??) with the precipitate density as $L = \rho_{\text{ppt}}^{-3}$ with the flux given by eq. (4.18):

$$r_{\text{ppt}} = 8\pi DR_{\text{ppt}}^2 \rho_{\text{ppt}}^{4/3} C \tag{4.21}$$

64

(a)
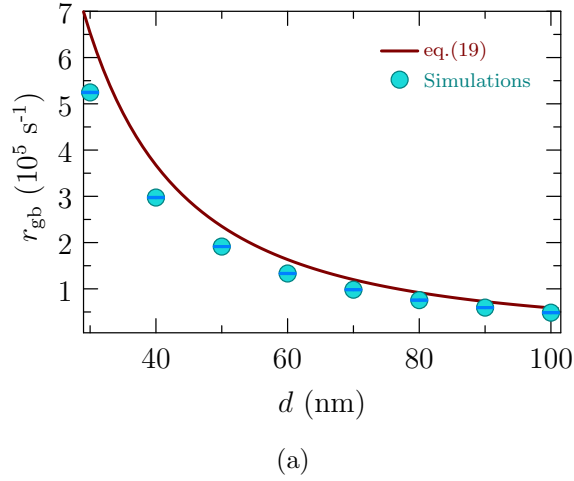
Figure 4.10: Comparison between eq. (4.20) and kMC simulations of one dimensionally diffusing particle absorption at grain boundaries. The error bars are shown within each data point due to the small value of the standard deviation for this case.

This implies a sink strength $k_{\mathrm{p}pt}^2 = 8\pi R_{\mathrm{p}pt}^2 \rho_{\mathrm{p}pt}^{4/3}$ for a density of precipitates $\rho_{\mathrm{p}pt}$ with radius $R_{\mathrm{p}pt}$.

Similarly, for a dislocation density of ρ_d, we use eq. (4.18) for the flux coming into an effective cross-sectional surface area of $A = 2RL$, where $L = \rho_d^{-1/2}$ which leads to:

$$r_{\mathrm{d}} = 8DR\rho_d^{3/2}C \tag{4.22}$$

This means that a sink strength of $k_d^2 = 8R\rho_d^{3/2}$ is defined for this case. In doing so, we have assumed that no interaction between 1D-moving particles and dislocations exists. Considering such effects requires solving a diffusion problem with a drift, which leads to the analytical derivation of the 'bias' factor [7]. Here we prefer to solve the homogeneous problem and use empirical bias factors as provided, e.g., by atomistic simulations [11, 36, 43]. Figures 4.11a and 4.11b show the results of the comparison between the numerical simulations and eqs. (4.21) and (4.22), with very good agreement found in both cases.
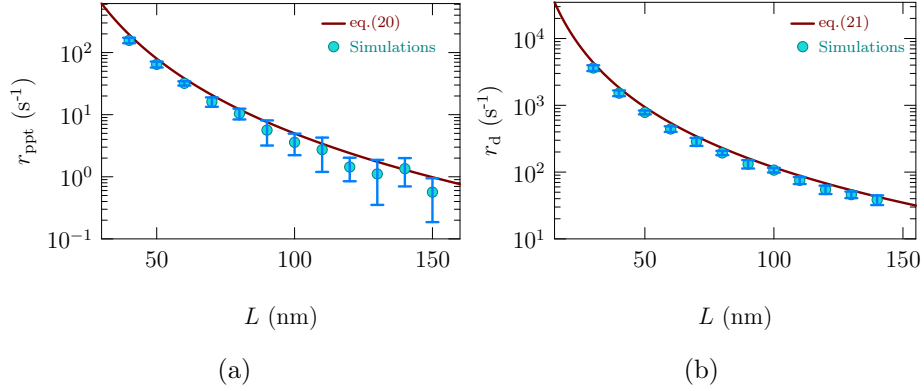
Figure 4.11: Comparison between numerical simulations and eqs. 4.21 (a), and 4.22 (b).

4.3.3 Particle absorption at free surfaces

The starting point for the geometry shown in Fig. 4.7d is also eq. (4.18). The distinction with respect to the grain boundary case is that the geometry used is a thin film of thickness l with periodic boundary conditions along the directions perpendicular to the free surfaces. Taking into account off-normal trajectories, the general expression for the flux at one of the surfaces is:

$$J_{\mathrm{f}s}(\phi) = \frac{8DC_\infty}{l} \cos^2 \phi \tag{4.23}$$

where ϕ is the angle between the particle trajectory and the surface normal. The current is defined in the usual way by multiplying times the free surface area $A = 2L^2$:

$$M_{\mathrm{f}s}(\phi) = J_{\mathrm{f}s}(\phi)A = \frac{8DC_\infty}{l} L^2 cos^2\phi$$

from which we obtain the rate after multiplying times C_1 with $C_\infty = (lL^2)^{-1}$:

$$r_{\mathrm{f}s}(\phi) = \frac{8D}{l^2} \cos^2 \phi C_1 \tag{4.24}$$

The predictions from this equation are compared with kMC simulations with random trajectory orientation (ϕ) in Figure 4.12.

Averaging expression (4.24) over the interval $[0, \pi/2]$, we arrive at the effective expression for the rate of absorption of one-dimensionally moving particles at free surfaces of a thin

66
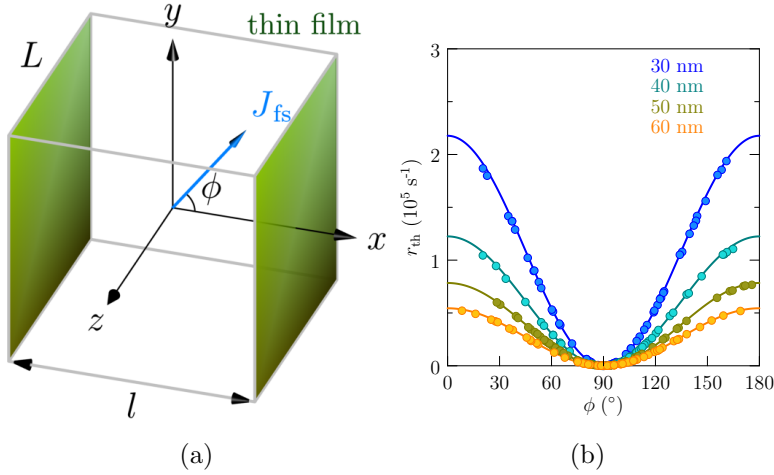
Figure 4.12: (a) Geometry of a particle trajectory in the thin film geometry. (b) Comparison between eq. (4.24) and different kMC simulations as function of ϕ.

film of thickness l:

$$r_{\mathrm{f}s} = \frac{4D}{l^2}C_1 \tag{4.25}$$

from which the corresponding sink strength is $\frac{4D}{l^2}$.

4.4   Discussion and summary

The asymmetry in diffusion dimensionality between self-interstitial atom (SIA) clusters and vacancies is a fundamental feature of irradiation damage in crystals, leading to a defect buildup imbalance that manifests itself as measurable dimensional and mechanical property changes. It is well known that, while vacancies and mobile vacancy clusters diffuse in a three-dimensional (3D) fashion, SIA clusters perform one-dimensional motion along mostly rectilinear trajectories. Despite this, a complete set of kinetic coefficients, including coagulation reaction rates and sink strengths, does not exist for 1D-moving objects. In this paper, we derive analytical expressions for these coefficients from continuum diffusion theory particularized to 1D motion. Moreover, we carry out kinetic Monte Carlo simulations of numerical replicas of the geometry of diffusing particles and sinks to validate the proposed

solutions. Our simulations, which are conducted entirely independently from the analytical derivations, reveal excellent agreement with the proposed expressions, adding confidence to their validity. We compare the 1D and 3D cases and discuss their relevance for kinetic codes for damage accumulation calculations.

A summary of the expressions derived and verified here for one-dimensionally diffusing particles is given in Table 4.1. Their 3D counterparts all also shown for reference. In general, it can be seen that sink strengths for 1D-moving species are higher for escribed absorbers (grain boundaries and free surfaces) and lower for inscribed absorbers (precipitates and dislocations) than in the 3D case. This is in principle not unexpected in view of the more direct nature of one-dimensional trajectories. Compounded with significantly higher diffusivities –particularly– at low temperatures, this is expected to make the absorption proclivity of SIA clusters at surface sinks even more pronounced compared to that of vacancies.

Table 4.1: Summary of expressions for 1D-moving particles and comparison with the 3D case (sink strengths for the 3D case taken from ref. [7]).

	Reaction rate	Sink strengths			
		Grain boundary (size d)	Precipitates (radius R, density ρ)	Dislocations (density ρ_d)	Thin film (thickness l)
1D	$8(R_1+R_2)(D_1+D_2)\left[(R_1+R_2)C_2^{1/3}+\dfrac{1}{2\ln\frac{C_2^{-1/3}}{2(R_1+R_2)}}\right]C_1C_2$	$24/d^2$	$8\pi R^2\rho^{4/3}$	$8R\rho_d^{3/2}$	$4/l^2$
3D	$4\pi(R_1+R_2)(D_1+D_2)C_1C_2$	$6/d^2$	$4\pi R\rho$	ρ_d	$2/l^2$

The coagulation rates are more complex to analyze, particularly for the 1D case due to the highly nonlinear terms in C_2. Figure 5.6 shows r_{1D} and r_{3D} as surface plots in a representative concentration interval. The figure clearly shows that the 1D rates are consistently lower than the 3D ones (as one intuitively would suspect), with the differences
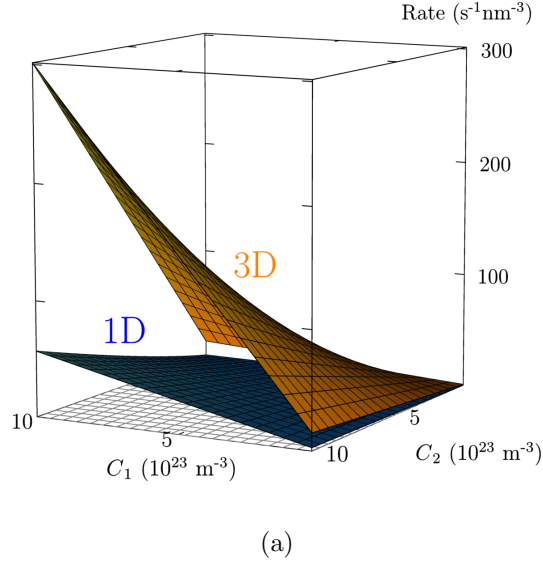
Figure 4.13: Comparison between r_{1D} and r_{3D} (see Table 4.1) in the concentration interval $[5 \times 10^{22}, 10^{24}]$ m^{-3}.

becoming more pronounced for high values of C_1 and C_2.

We note that the approach followed here to derive the analytical expressions shown in the table is slightly different than that on which the solutions proposed by Dunn et al. [14] is based. These build on Trinkaus' general expression for the sink strength, which is related to the defect mean free path λ_α [2, 42]:

$$r_i = k_\alpha^2 D_i C_i = \frac{1}{\lambda_\alpha^2} D_i C_i$$

where k_α^2 is expressed as an inverse cross section that depends on the sink concentration c and its capture radius R:

$$k_\alpha^2 = (\pi R^2 c)^2$$

Derivations using this formalism [2] have shown that in the case of 1D-moving species a periodic arrangement of absorbers should not be reduced to its minimum repeatable unit cell because the mean free path of these particles can well encompass several of these unit cells. This is generally neglected for 3D-moving particles because their sampling of the

69

configurational space is much more efficient, typically leading to reaction with the nearest neighbor absorber. In this sense, our results provide a lower bound (or first order estimation) to the general solutions for the sink strengths of the absorbers considered here. While based on these premises, the solutions used by Dunn et al. do not capture this long-range effect, in which case we believe our expressions are of more general applicability.

As well, it should also be mentioned that diffusion is the result of the collective behavior of particles following nonlinear trajectories in phase space[32, 33, 34]. As such, the diffusion coefficient is defined as the ensemble average of the particle displacement self-correlation function, which when considered in an isotropic infinite medium leads to the value of the diffusivity in the bulk. Here we assume that the scale of the simulation boxes exceeds the correlation lengths of particle motion, which allows us to consider a uniform diffusion coefficient in all the scenarios considered here.

To summarize, in this work we have derived analytical expressions for the reaction rates of one-dimensionally moving species by solving the diffusion equation along straight trajectories in a 3D setting. Our derivations include solutions for the coagulation rates and the absorption rates at sinks, including grain boundaries, precipitates, dislocations, and thin films. Our solutions have all been verified using specifically-tailored kMC simulations, which have confirmed in all cases the validity of the expressions. These are given in a format amenable for use in kinetic rate theory simulations, such as cluster dynamics models based on the mean-field approximation and classical nucleation theory. Work is currently underway to implement them in our codes to assess more precisely the effect of using the correct dimensionality in the kinetic coefficients.
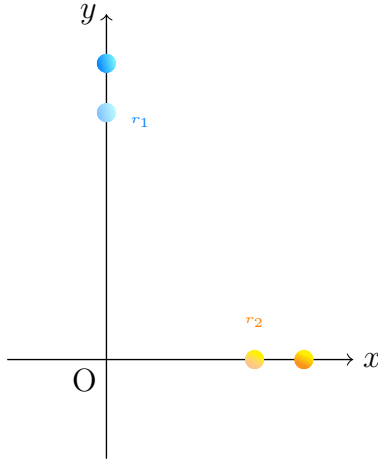
(a)

Figure 4.14: Representation of two particles moving along perpendicular trajectories.

4.5   Appendix

When two particles with diffusivities D_1 and D_2 move along perpendicular trajectories, the problem can be reduced to the motion of particle 1 with effective diffusivity $\frac{D_1+D_2}{2}$ keeping particle 2 stationary. The geometry is shown in Figure 4.14, with particle 1 moving along the positive y axis and particle 2 along positive x. At time t_n each particle's position can be described by:

$$\boldsymbol{r}_1^n = (x_n, 0); \tag{4.26}$$

$$\boldsymbol{r}_2^n = (0, y_n). \tag{4.27}$$

At time $t_{n+1} = t_n + \delta t$, the position of the particles is:

$$\boldsymbol{r}_1^{n+1} = \left(x_n + \sqrt{2D_1\delta t}, 0\right) \tag{4.28}$$

$$\boldsymbol{r}_2^{n+1} = \left(0, y_n + \sqrt{2D_2\delta t}\right) \tag{4.29}$$

The relative position of particle 1 with respect to particle 2 at times t_n and t_{n+a} can be written as:

$$\boldsymbol{r}_{1\text{-}2}^n = \boldsymbol{r}_1^n - \boldsymbol{r}_2^n = (x_n, y_n) \tag{4.30}$$

71

$$r_{1\text{-}2}^{n+1} = r_1^{n+1} - r_2^{n+1} = \left(x_n + \sqrt{2D_1 \delta t}, y_n + \sqrt{2D_2 \delta t} \right) \qquad (4.31)$$

and so the *m*ean displacement of particle 1 relative to particle 2 during the time interval δt

is:

$$\delta r_{1\text{-}2} = r_{1\text{-}2}^{n+1} - r_{1\text{-}2}^{n} = \left(\sqrt{2D_1 \delta t}, \sqrt{2D_2 \delta t} \right) \qquad (4.32)$$

Taking squares of the above expression, one can calculate the *mean square displacement* of

particle 1 relative to particle 2:

$$\delta r_{1\text{-}2}^2 = \left| r_{1\text{-}2}^{n+1} - r_{1\text{-}2}^{n} \right|^2 = 2\left(D_1 + D_2 \right) \delta t \qquad (4.33)$$

However, this mean square displacement must be the same as that of the *r*elative particle,

which has an effective diffusivity D and moves in the two-dimensional space (x, y). Because

of this, we can write:

$$D = \frac{\delta r_{1\text{-}2}^2}{4\delta t} = \frac{(D_1 + D_2)}{2} \qquad (4.34)$$

which is the expression for the diffusivity used in Sec. 4.2.2.

4.6 References

[1] David J Bacon and Tomas Diaz de la Rubia. Molecular dynamics computer simulations of displacement cascades in metals. *Journal of Nuclear Materials*, 216:275–290, 1994.

[2] AV Barashev, SI Golubov, and H Trinkaus. Reaction kinetics of glissile interstitial clusters in a crystal containing voids and dislocations. *Philosophical Magazine A*, 81 (10):2515–2532, 2001.

[3] AV Barashev, SI Golubov, and RE Stoller. Theoretical investigation of microstructure evolution and deformation of zirconium under neutron irradiation. *Journal of Nuclear Materials*, 461:85–94, 2015.

[4] Alain Barbu and Emmanuel Clouet. Cluster dynamics modeling of materials: advantages and limitations. In *Solid State Phenomena*, volume 129, pages 51–58. Trans Tech Publ, 2007.

[5] Richard Becker and Werner Döring. Kinetische behandlung der keimbildung in übersättigten dämpfen. *Annalen der Physik*, 416(8):719–752, 1935.

[6] V.A. Borodin. Rate theory for one-dimensional diffusion. *Physica A: Statistical Mechanics and its Applications*, 260(3):467 – 478, 1998. ISSN 0378-4371. doi: https://doi.org/10.1016/S0378-4371(98)00338-0. URL `http://www.sciencedirect.com/science/article/pii/S0378437198003380`.

[7] AD Brailsford and Ronald Bullough. The theory of sink strengths. *Phil. Trans. R. Soc. Lond. A*, 302(1465):87–137, 1981.

[8] AD Brailsford, R Bullough, and MR Hayns. Point defect sink strengths and void-swelling. *Journal of Nuclear Materials*, 60(3):246–256, 1976.

[9] R Bullough, MR Hayns, and MH Wood. Sink strengths for thin film surfaces and grain boundaries. *Journal of Nuclear Materials*, 90(1-3):44–59, 1980.

[10] C Cawthorne and EJ Fulton. Voids in irradiated stainless steel. *Nature*, 216(5115):575, 1967.

[11] Zhongwen Chang, Pär Olsson, Dmitry Terentyev, and Nils Sandberg. Dislocation bias factors in fcc copper derived from atomistic calculations. *Journal of Nuclear Materials*, 441(1-3):357–363, 2013.

[12] T Diaz De La Rubia and MW Guinan. New mechanism of defect production in metals: A molecular-dynamics study of interstitial-dislocation-loop formation in high-energy displacement cascades. *Physical review letters*, 66(21):2766, 1991.

[13] S. L. Dudarev. Inhomogeneous nucleation and growth of cavities in irradiated materials. *Phys. Rev. B*, 62:9325–9337, Oct 2000. doi: 10.1103/PhysRevB.62.9325. URL `https://link.aps.org/doi/10.1103/PhysRevB.62.9325`.

[14] Aaron Y. Dunn, Laurent Capolungo, Enrique Martinez, and Mohammed Cherkaoui. Spatially resolved stochastic cluster dynamics for radiation damage evolution in nanostructured metals. *Journal of Nuclear Materials*, 443(1):128 – 139, 2013. ISSN 0022-3115. doi: https://doi.org/10.1016/j.jnucmat.2013.07.009. URL `http://www.sciencedirect.com/science/article/pii/S0022311513008878`.

[15] Kevin G Field, Ryan Jacobs, Mingen Shen, Matthew Lynch, Priyam Patki, Christopher Field, and Dane Morgan. Development and deployment of automated machine learning detection in electron microcopy experiments. *Microscopy and Microanalysis*, 27(S1): 2136–2137, 2021.

[16] NM Ghoniem and G Kulcinski. A rate theory approach to time dependent microstructural development during irradiation. *Radiation Effects*, 39(1):47–56, 1978.

[17] NM Ghoniem and S Sharafat. A numerical solution to the fokker-planck equation describing the evolution of the interstitial loop microstructure during irradiation. *Journal of Nuclear Materials*, 92(1):121–135, 1980.

[18] U Gösele and W Frank. Extension of the unsaturable trap model to one-dimensional interstitial migration. *physica status solidi (b)*, 61(1):163–172, 1974.

[19] U Gösele and FA Huntley. Two-dimensional bimolecular diffusion limited reaction kinetics. *Physics Letters A*, 55(5):291–292, 1975.

[20] U Gösele and A Seeger. Theory of bimolecular reaction rates limited by anisotropic diffusion. *Philosophical Magazine*, 34(2):177–193, 1976.

[21] GW Greenwood, AJE Foreman, and DE Rimmer. The role of vacancies and dislocations in the nucleation and growth of gas bubbles in irradiated fissile material. *Journal of Nuclear Materials*, 1(4):305–324, 1959.

[22] SL Hardt. Rates of diffusion controlled reactions in one, two and three dimensions. *Biophysical chemistry*, 10(3-4):239–243, 1979.

[23] Mehrer Helmut. Diffusion in solids; fundamentals, methods, materials, diffusioncontrolled processes, 2007.

[24] Ryan Jacobs, Mingren Shen, Yuhan Liu, Wei Hao, Xiaoshan Li, Ruoyu He, Jacob RC Greaves, Donglin Wang, Zeming Xie, Zitong Huang, et al. Performance and limitations of deep learning semantic segmentation of multiple defects in transmission electron micrographs. *Cell Reports Physical Science*, 3(5):100876, 2022.

[25] T Jourdan, G Bencteux, and G Adjanor. Efficient simulation of kinetics of radiation induced defects: a cluster dynamics approach. *Journal of Nuclear Materials*, 444(1-3): 298–313, 2014.

[26] Aaron A. Kohnert and Brian D. Wirth. Cluster dynamics models of irradiation damage accumulation in ferritic iron. ii. effects of reaction dimensionality. *Journal of Applied Physics*, 117(15):154306, 2015. doi: 10.1063/1.4918316. URL `https://doi.org/10.1063/1.4918316`.

[27] Yu V Konobeev, AV Subbotin, and SI Golubov. The theory of void and interstitial dislocation loop growth in irradiated metals. *Radiation Effects*, 20(4):265–271, 1973.

[28] Eiichi Kuramoto, Kazuhito Ohsawa, Junichi Imai, Kiyokazu Obata, and Tetsuo Tsutsumi. Bias mechanism and its effects for fundamental process of irradiation damage. *Materials transactions*, 45(1):34–39, 2004.

[29] LK Mansur. Theory and experimental background on dimensional changes in irradiated alloys. *Journal of Nuclear Materials*, 216:97–123, 1994.

[30] Jaime Marian and Vasily V Bulatov. Stochastic cluster dynamics method for simulations of multispecies irradiation damage accumulation. *Journal of Nuclear Materials*, 415(1): 84–95, 2011.

[31] AA Semenov and CH Woo. Classical nucleation theory of microstructure development under cascade-damage irradiation. *Journal of nuclear materials*, 323(2-3):192–204, 2003.

[32] Ming-Ren Shen, Rui Liu, Mei-Ying Hou, Yang Ming-Cheng, and Chen Ke. Mesoscale simulation of self-diffusiophoretic microrotor. *Acta Physics Sinica*, 65(17):170201, 2016.

[33] Mingren Shen, Fangfu Ye, Rui Liu, Ke Chen, Mingcheng Yang, and Marisol Ripoll. Chemically driven fluid transport in long microchannels. *The journal of chemical physics*, 145(12):124119, 2016.

[34] Mingren Shen, Rui Liu, Ke Chen, and Mingcheng Yang. Diffusive-flux-driven microturbines by fore-and-aft asymmetric phoresis. *Physical Review Applied*, 12(3):034051, 2019.

[35] Mingren Shen, Guanzhao Li, Dongxia Wu, Yuhan Liu, Jacob RC Greaves, Wei Hao, Nathaniel J Krakauer, Leah Krudy, Jacob Perez, Varun Sreenivasan, et al. Multi defect detection and analysis of electron microscopy images with deep learning. *Computational Materials Science*, 199:110576, 2021.

[36] AB Sivak, VM Chernov, VA Romanov, and PA Sivak. Kinetic monte-carlo simulation of self-point defect diffusion in dislocation elastic fields in bcc iron and vanadium. *Journal of Nuclear Materials*, 417(1-3):1067–1070, 2011.

[37] M v Smoluchowski. Versuch einer mathematischen theorie der koagulationskinetik kolloider lösungen. *Zeitschrift für physikalische Chemie*, 92(1):129–168, 1918.

[38] N Soneda and T Diaz De La Rubia. Defect production, annealing kinetics and damage evolution in α-fe: an atomic-scale computer simulation. *Philosophical Magazine A*, 78 (5):995–1019, 1998.

[39] Roger E Stoller, Stanislav I Golubov, C Domain, and CS Becquart. Mean field rate theory and object kinetic monte carlo: A comparison of kinetic models. *Journal of Nuclear Materials*, 382(2-3):77–90, 2008.

[40] Michael P Surh, JB Sturgeon, and WG Wolfer. Master equation and fokker–planck methods for void nucleation and growth in irradiation swelling. *Journal of nuclear materials*, 325(1):44–52, 2004.

[41] H Trinkaus, BN Singh, and CH Woo. Defect accumulation under cascade damage conditions. *Journal of nuclear materials*, 212:18–28, 1994.

[42] H Trinkaus, BN Singh, and SI Golubov. Progress in modelling the microstructural evolution in metals under cascade damage conditions. *Journal of nuclear materials*, 283:89–98, 2000.

[43] WG Wolfer. The dislocation bias. *Journal of Computer-Aided Materials Design*, 14(3): 403–417, 2007.

[44] CH Woo and BN Singh. The concept of production bias and its possible role in defect accumulation under cascade damage conditions. *physica status solidi (b)*, 159(2):609–616, 1990.

[45] CH Woo and BN Singh. Production bias due to clustering of point defects in irradiation-induced cascades. *Philosophical Magazine A*, 65(4):889–912, 1992.

CHAPTER 5

Strain response of nanoporous multiferroic composites under electric field

5.1 Introduction

Multiferroic composites have attracted a considerable amount of research in recent years as functional materials that exhibit the *magnetoelectric* (ME) effect. These materials transfer the strain induced by an external electric field in the ferroelectric component to the ferromagnetic component through elastic coupling. The application of multiferroic materials can drastically reduce power consumption in small-scale devices compared to standard electromagnetic devices. Advances in chemical synthesis and device fabrication have resulted in a renewed interest in composite ME materials thanks to superior ability to couple their magnetic and electric response. Compared with single phase ME materials, multiferroic composites have obvious advantages. For example, they display a significant ME effect at room temperature, whereas single-phase materials only show a simultaneous piezoelectric and magnetic response at low temperatures (below the transition temperature) [23, 30]. This makes them attractive for a number of potential applications such as sensors, switches, data storage elements, and other novel electronic devices [].

Multiferroic composites were originally synthesized in the early 1990s [28] using unidirectional eutectic mixtures of $BaTiO_3$ and $CoFe_2O_4$. Several other designs have been proposed since, such as particulate composites, thin laminate composites, and fiber/rod composites [3, 14, 21, 22, 25, 26, 29, 34]. Despite these improvements, multiferroic devices composed

79

of dissimilar materials arranged in alternating geometries are often limited by poor mechanical coupling, thermal expansion coefficient mismatch, or irregular interfacial bonding. In many instances, these issues appear during synthesis and can all contribute to a weakened ME effect. By way of example, multiferroic thin film composites with ceramic components have been widely reported to develop microcracks during fabrication by solution deposition [8, 18, 19].

Alternatively, nanoscale synthesis and device operation can result in substantial quality improvements in device morphology and coupling response. In recent years, research on nanoscale multiferroic heterostructures [17, 33], organic multiferroics [23], thin films [6], among others, has demonstrated the feasibility of nanosynthesis techniques. As well, theory and simulation are being used to establish the suitability of downscaling different multiferroic designs as well as assessing their potential response [1, 31]. In this work, we present finite element simulations of a novel multiferroic structure generated by infiltrating a ferroelectric phase, lead zirconate titanate, onwards referred to as 'PZT' ($PbZr_xTi_{1-x}O_3$, where $x=0.52$ in this work) via atomic layer deposition (ALD) into a nanoporous ferromagnetic template made of cobalt ferrite ($CoFe_2O_4$, referred to as 'CFO'). Such structures have been seen to yield an enhanced ME response and be free of many of the issues limiting other multiferroic devices. We focus on the dependence of the deformation behavior of the device on the thickness of the ALD film coating the interior of the pores. In particular, we model the non-monotonic strain response of the structure as a function of PZT thickness and analyze the physical causes behind such response.

The paper is organized as follows. We begin with a brief description of the synthesis procedure and magnetic measurements of the nanostructure (5.2.1). This is followed by a detailed description of the finite element model and parameterizations used in the simulations (5.2.2 and 5.2.2.2). We then show the results of the modeling approach, including a geometric analysis and the impact of nonlinear piezoelectricity (5.3). We finalize with a discussion and the main conclusions (5.4).

5.2 Methods

5.2.1 Sample preparation

Nanostructured PZT/CFO composites were created in two parts: first making the porous CFO architecture, then conformally coating the inside of the pores using ALD. First, porous CFO structures were synthesized by block copolymer templating of sol gel films, as reported elsewhere [5, 24]. In brief, metal precursors were dissolved, and over time, condensation reactions form a metal oxide polymer known as a 'gel'. An amphiphilic di-block copolymer is added, which forms micelles in solution. As the solution is deposited onto the conductive silicon substrate, micelles self-assemble into ordered, periodic structures. Once pyrolyzed, the polymer is removed, leaving behind a porous, metal oxide framework. ALD was then used to conformally coat the inside of the pores with PZT, the details for which are discussed elsewhere [4]. Since ALD is a gas phase deposition process, the ALD precursors uniformly bind to available surface sites throughout the porous network. The thickness of the PZT coating is precisely controlled by the ALD process, and The ALD layers were then crystallized through rapid thermal annealing, or RTA, at 700°C for 60 seconds under oxygen. To observe the magnetoelectric coupling of the PZT/CFO composite structure, samples were electrically poled ex situ with the electric field being applied perpendicular to the sample. Samples were cut down to be approximately 5×5 mm^2, then sandwiched between aluminum electrodes with a 13 μm thick dielectric spacer above the film side to prevent shorting. The electric fields utilized in this work ranged between 0 to 1.42 MV/m. Importantly, since the films were poled ex situ, with measurements being performed in the absence of an electric field, the remnant (not saturation) changes are discussed in this work. Once poled, high resolution diffraction measurements were performed at Stanford Synchrotron Light Source (SSRL), experimental station 7-2, with an x-ray energy of 0.9919 Å and 1.0332 Å. The d-spacing of the composites was determined by peak fitting the CFO (311) diffraction peaks to a Voigt function (through `PeakFit v4.11` [32]). Measurements shown in this work were performed

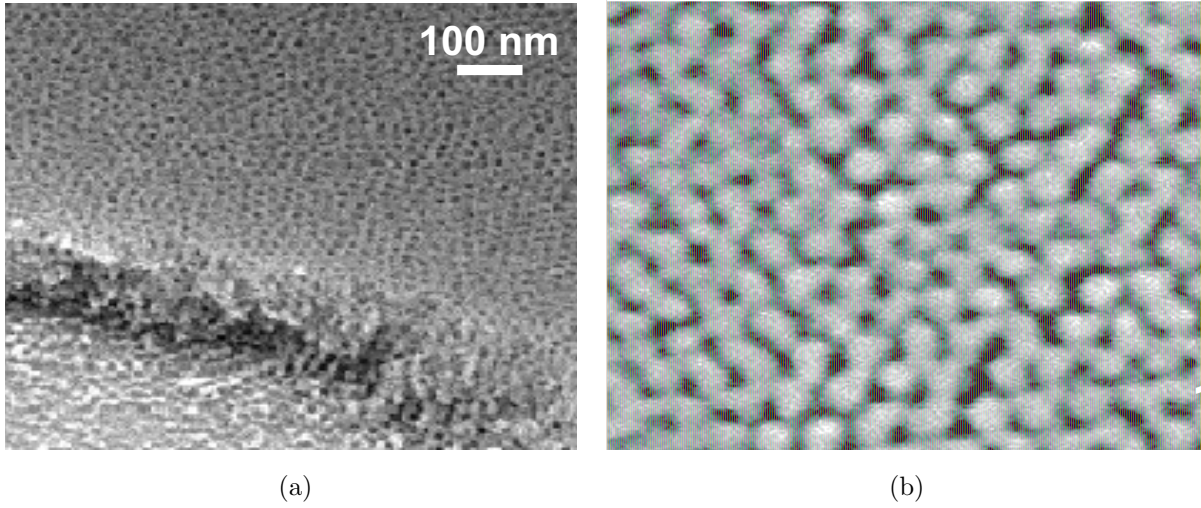out of the plane of the sample, showing out-of-plane tension.

Figure 5.1: (a) Top down and (b) cross sectional view of bare, unfilled CFO, demonstrating pore symmetry. For the composites, bare CFO was filled with atomic layer deposition grown PZT, which is described in refs. [2, 4].

5.2.2 Geometry construction and FEM simulations

5.2.2.1 Simulation structure and geometric details

Finite element (FE) simulations of a nanoporous network of CFO internally coated with PZT are carried out using `COMSOL Multiphysics` [7]. The CFO network functions as the ferromagnetic substructure while the PZT filling provides the ferroelectric response. The pores of the CFO substructure are arranged into a close-packed three dimensional lattice (i.e., a face-centered cubic lattice, or FCC). The pores are coated with a PZT layer of varying thickness (3, 6, and 10 nm), as shown in Figure 5.2b. The CFO and the PZT are assumed to be ideally bonded (no gaps or cracks) with the displacements being continuous across their interface (Dirichlet boundary condition).

The size of the 'unit' FCC cell for the CFO structure was $\approx$42 nm, while the pore

diameters were in the 15∼20-nm range. The radius of the ligaments connecting the pores (only along the *first nearest-neighbor* distance of the underlying FCC cell) was 8 nm. Figure 5.2 shows images of the unfilled CFO substructure (5.2a), and the coated structures with 3, 6, and 10 nm-thick PZT (5.2b, 5.2c, and 5.2d, respectively). With 10-nm PZT layers, the ligaments become fully infiltrated and the pores are no longer interconnected. The porosity of the entire structure for each ALD-coating thickness is 15.3, 6.6, and 0.03%, respectively.

5.2.2.2 Physical modeling

Application of an external electric field, $\boldsymbol{E}$, results in a piezoelectric coupling with the ferroelectric component of the device, i.e., the PZT coating. The PZT deforms, transferring part of the deformation to the ferromagnetic component CFO, which itself triggers a magnetic response. The governing equations for the piezoelectric effect can be expressed in stress-charge form as:

$$\boldsymbol{T} = \mathbb{C}_E \boldsymbol{S} - \mathfrak{e}^t \boldsymbol{E} \tag{5.1}$$

$$\boldsymbol{D} = \mathfrak{e}\boldsymbol{S} + \varepsilon_0 \boldsymbol{\varepsilon}_S \boldsymbol{E} \tag{5.2}$$

or in strain-charge form:

$$\boldsymbol{S} = \mathbb{S}_E \boldsymbol{T} - \mathfrak{d}^t \boldsymbol{E} \tag{5.3}$$

$$\boldsymbol{D} = \mathfrak{d}\boldsymbol{T} + \varepsilon_0 \boldsymbol{\varepsilon}_T \boldsymbol{E} \tag{5.4}$$

where $\boldsymbol{T}$ and $\boldsymbol{S}$ are the stress and strain tensors, respectively, $\boldsymbol{E}$ is the electric field (vector), $\boldsymbol{D}$ is the electric displacement vector, $\mathbb{C}_E = \mathbb{S}_E^{-1}$ is the elasticity matrix, $\mathfrak{e}$ and $\mathfrak{d}$ are the *converse* and *direct* piezoelectric coefficient matrices, ε_0 is the permittivity in free space, and $\boldsymbol{\varepsilon}_S$ and $\boldsymbol{\varepsilon}_T$ are the material permittivity matrices at constant strain and stress, respectively. $\mathbb{C}_E$ ($\mathbb{S}_E$), $\mathfrak{e}$ ($\mathfrak{d}$), and $\boldsymbol{\varepsilon}_S$ ($\boldsymbol{\varepsilon}_T$) are tensors of rank four, three, and two, respectively. These tensors, however, are highly symmetric for physical reasons and they can generally be represented as sparse matrices using Voigt notation, which makes their algebraic treatment

more convenient. `COMSOL` includes a standard piezoelectric constitutive model such as this one in its `Multiphysics` release [1]. The values used in the present work for PZT are listed in Appendix 5.5.1. CFO is simply treated as a compatible material with cubic structure. Its elastic properties are given in Appendix 5.5.2.

Closure of the system of eqs. (5.3) and (5.4) is achieved by adding the equilibrium conditions $\nabla \cdot \boldsymbol{D} = 0$, $\nabla \times \boldsymbol{E} = 0$, $\nabla \cdot \boldsymbol{T} = 0$, and the definition of the strain tensor from the displacement vector $\boldsymbol{u}$: $\boldsymbol{S} = \frac{1}{2} \left(\nabla \boldsymbol{u} + \boldsymbol{u} \nabla \right)$. The system is assumed to be constrained by the device geometry along the x and y directions and thus no displacements are allowed on those boundaries, i.e. $\boldsymbol{u} = (0, 0, u_z)$. Along the z direction, displacements are uniform across the entire top surface, with u_z equal to the displacement of the center of mass of that surface.

By way of example, the mesh for the 3 nm-thick PZT layer consists of over 100,000 elements and is shown in Figure 5.3.

5.3   Results

First, we simulate the strain response of the structures shown in Fig. 5.2 as a function of the applied external electric field assuming perfectly linear piezoelectric behavior and ideal CFO/PZT interface bonding. Demonstrative examples are given in Figure5.4 for the displacement (5.4a) and stress (5.4b) fields for the 3-nm PZT layer case when $E_z = 1.2$ MV·m^{-1}.

The results as a function of E_z are shown in Figure 5.5, where the experimental measurements have also been included. While based on these results it may appear that the relationship between PZT-coating thickness and applied voltage is monotonically decreasing, next we map the response of thicknesses from 1 nm to full infiltration (zero porosity, around 11 nm) to get a clearer picture of the dependence on PZT layer thickness. A surface plot showing the calculations of the strain as a function of these two variables is shown in

---

[1]https://www.comsol.com/blogs/piezoelectric-materials-understanding-standards.

Figure 5.6. As the data show, the peak piezoelectric effect is reached for a coating thickness of 3 nm, increasing sharply from zero, and decreasing smoothly thereafter.

To understand this behavior, and also to explain the differences with the experimental data, in the following sections we explore the effect of non-ideal conditions on device response.

5.3.1 Nonlinear piezolectricity of PZT

We start by considering the effect of nonlinear piezoelectricity on the current design response. Recall from App. 5.5.1 the expression for the direct piezoelectric coefficient matrix used in eqs. (5.3) and (5.4):

$$\mathfrak{d} = \begin{bmatrix} 0 & 0 & 0 & 0 & d_{15} & 0 \\ 0 & 0 & 0 & d_{24} & 0 & 0 \\ d_{31} & d_{32} & d_{33} & 0 & 0 & 0 \end{bmatrix}$$

In piezoelectricity, the polarization of a crystal under the application of an electric field or a mechanical stress consists of intrinsic and extrinsic contributions [12, 13]. The intrinsic contribution is associated with the atomic structure of the crystal lattice, and it is strictly speaking the only one that can be considered linearly coupled to the electric field. The extrinsic response results principally from 90° domain wall movements [12], which naturally exist in ferroelectric materials like PZT [15]. Poling of PZT prior to electrical stimulation enhances this nonlinear effect by aligning like-domains and enhancing the polarization response. Indeed, domain wall movement increases with the intensity of the electric field and thus the extrinsic part of the polarization is seen to couple more strongly to $\boldsymbol{E}$.

The standard model that captures this nonlinearity is the Rayleigh law [9, 11, 27], which for d_{zz} [2] under a constant applied electric field takes the simple form:.

$$d_{33} = d_{\mathrm{int}} + \alpha E_3 \tag{5.5}$$

where $d_{int} = 593$ fC N^{-1} (cf. Appendix 5.5.1) represents the intrinsic part of the coefficients

---

[2]Only 'axial' components of $\mathfrak{d}$ are subjected to extrinsic polarization.

and α is the Rayleigh constant. For tetragonal PZT, $\alpha = 6.02 \times 10^{-18}$ m^2 C N^{-2} [10]. Consistent with *ex* situ poling of our multiferroic structure, we carry out computer simulations with the updated Rayleigh model. The results are shown in Figure 5.7. The calculated data points show a larger deviation of the device strain with PZT-coating thickness as the electric field increases, more in line with the experimental results.

While the magnitude of the results is different between the results in Figs. 5.5 and 5.7, the S_{zz}-E_z trend remains. In the next subsection we carry out extra analysis to understand the reasons behind this.

5.3.2 CFO/PZT interface coupling

As indicated in Sec. 5.2.2.2, the FE simulations are carried out using Dirichlet boundary conditions (continuity in the displacement field). This leads to a discontinuous stress distribution across a dissimilar material interface, as illustrated in Fig. 5.4b. Due to the axial nature of the deformation (along the z direction) and the spherical nature of the internal cavity, the stresses that develop on elements of PZT near the equatorial plane of the pore are of tangential character, while those on elements aligned with z (near the spherical caps of the pore) are of tensile character. The relative magnitude of these two types of stresses depends on the value of E_z and on the geometry changes of the material due to deformation. It is thus important to understand the effect that these stresses have on the device response. To that end, we perform a series of simulated tests aimed at isolating the stress component in each case and analyze its impact on the material.

5.3.2.1 Shear coupling

First we set up a simple test where a layer of PZT of varying thickness is attached to a CFO solid block 10-nm in size in the manner shown in Figure 5.8a. Then a voltage differential of 0.05 V is applied to the PZT layer so as to induce piezoelectric expansion and the deformation

and stress of the system are obtained. This resembles the conditions in the region of the PZT layer under tangential stress. However, because CFO is not directly mechanically deformed, the elements adjacent or near the PZT/CFO interface are under shear stresses, as shown in Figure 5.8b. Interestingly, while the region of CFO near the interface deforms in the same manner as the PZT, at a distance away from it the trend inverses and the CFO contracts along the direction of the applied field. Thus, shear stresses in CFO created by tangential stresses in PZT can partially induce an inverse displacement-voltage correlation, which is more pronounced the farther away from the interface.

The results as a function of PZT-layer thickness (at a fixed value of $E_z = 5.0$ MV m^{-1}) are shown in Figure 5.9, where we plot the strain S_{zz} on the edge of CFO block farthest from the interface. As the graph illustrates, this strain is negative under shear conditions at the interface, with a maximum value of -0.80 % for a PZT thickness of 6 nm.

5.3.2.2 Tensile coupling

By contrast, application of a constant electric field to the geometry shown in Figure 5.10a results in positive monotonically increasing strains as the PZT layer thickness increases, as seen in Fig. 5.9. These computational tests thus reveal a mixed picture whereby (i) a diminishing strain response of the system with PZT thickness to an external electric field is observed when the CFO/PZT interface is oriented tangentially to the loading direction, and (ii) an increasing strain response when oriented along the field direction. Note that these tests in Secs. 5.3.2.1 and 5.3.2.2 only capture the effect of the interface coupling, but not the effect of porosity. We study this in the next section.

5.3.3 Effect porosity on structure response

To understand the effect of porosity, we carry out simulations of a simplified geometry consisting of a simple cubic cell with a single central internal pore, as depicted in Figure

5.11a. First, we study the deformation of the isolated PZT material relative to the combined structure. For this, the central pore is then infiltrated with PZT forming a coating layer of varying thickness and the resulting PZT material is extracted and studied separately (Figure 5.11b). We then apply a constant voltage to both geometries and simulate the deformation with and without CFO. The results are shown in Figure 5.12 where a clear gap (with a factor of 3∼4) in strain can be appreciated between the CFO+PZT structure versus just having PZT. Moreover, the PZT substructure differs from the combined one in that the S_{xx} vs. thickness relation is not monotonically decreasing. The PZT strain does not vary much as a function of thickness. This means that the increased stiffness due to reduced porosity as the coating thickness grows is matched almost exactly by the tensile driving force created by the extra volume pf PZT. For the combined CFO-PZT structure in Fig. 5.11a, in addition to the 3∼4 scale reduction in strain compared to the pure PZT case, a non-monotonic (albeit decreasing after 3-nm thickness) dependence is again observed. This implies that the the extra stiffness added by the CFO substructure is sufficient to contain the extra tensile driving force of a thicker PZT (lower porosity)

The slightly increasing part of the curve below 3-nm thickness suggests that the overall stiffness increase of the structure as the porosity is reduced is not sufficient to compensate for the extra tensile driving force.

5.4   Discussion and conclusions

Reduced to its simplest expression, the deformation behavior of a CFO porous nanostructure partially filled with PZT can be understood as a competition between two phenomena. First, an open cell structure is always softer than a solid one. As the thickness of the internal PZT layer increases, one expects the stiffness of the structure to grow, leading to a reduction in overall strain. On the other hand, PZT is the electro-mechanical sensitive material that transforms an electric signal into deformation, and so having more of it contributes

88

to increasing the strain. As the experimental and FE results show, such competition does not result in a monotonic response. Above a critical thickness of 3 nm, the strain decreases, indicating that the reduction in porosity dominates over the extra piezoelectric driving force. Below 3 nm, the strain grows with PZT thickness, indicating that the piezoelectric driving force overcomes the extra stiffness that results from the decrease in porosity.

While this balance between porosity and piezoelectricity has not been reported before for multiferroic structures, studies have shown that the relative fraction of ferromagnetic and ferroelectric phases does impact the system's magnetic response. In a recent work, it has been shown that CFO/PZT composites with molar ratios of 1:4 and 1:6 were seen to exhibit better ferroelectricity and magnetic properties, with the overall magnetization decreasing with increasing PZT content [16].

Another point worth discussing is the need to include nonlinear piezoelectricty in the ferroelectric material due to extrinsic poling of PZT. The comparison of the results in Figs. 5.5 and 5.7 with the experimental data confirms this by a much improved agreement with the measurements.

We conclude the paper with a summary of our most important points:

1. We have developed a computational finite-element model of a nanoporous multiferroic composite consisting a CFO template coated in the interior of the pores with PZT of various thicknesses. The scale of the model mimics that of the experimentally synthesized structures, with the model subjected to nominally identical boundary conditions as in experimental tests.

2. The model has been run parametrically as a function of PZT layer thickness and electric field in an attempt to reproduce the observed experimental response of a non-monotonic strain response of the nanoporous structure with ALD thickness. We have considered both linear and nonlinear piezoelectric responses to infer the degree of poling of PZT prior to the application of an electric field.

3. We find that the observed non-monotonic response stems from two competing processes. First, increased porosity works towards increasing the strain due to a reduced system stiffness. Second, decreased porosity involves a larger mass fraction of PZT, which drives the electro-mechanical response of the structure, thus leading to a larger strain.

4. The balance between these two driving forces is controlled by the shear coupling at the CFO/PZT interface and the effective PZT cross section along the direction of the applied electric field.

5.5 appendix

5.5.1 PZT elastic properties

List of parameters for PZT employed in the present analysis. For the components of $\mathbb{C}_E$ ($\mathbb{S}_E$), $\mathfrak{e}$ and $\mathfrak{d}$ we assume trigonal symmetry.

$$\mathfrak{d} = \begin{bmatrix} 0 & 0 & 0 & 0 & 741 & 0 \\ 0 & 0 & 0 & 741 & 0 & 0 \\ -274 & -274 & 593 & 0 & 0 & 0 \end{bmatrix} \; [\times 10^{-15} \; \mathrm{C} \; \mathrm{N}^{-1}]$$

$$\mathfrak{e} = \begin{bmatrix} 0 & 0 & 0 & 0 & 17.03 & 0 \\ 0 & 0 & 0 & 17.03 & 0 & 0 \\ -6.62 & -6.62 & 23.24 & 0 & 0 & 0 \end{bmatrix} \; [\mathrm{C} \; \mathrm{m}^{-2}]$$

$$\varepsilon_S = \begin{bmatrix} 1704.4 & 0 & 0 \\ 0 & 1704.4 & 0 \\ 0 & 0 & 1433.6 \end{bmatrix} \; [\varepsilon_0]$$

90

$$\varepsilon_T = \begin{bmatrix} 3130 & 0 & 0 \\ 0 & 3130 & 0 \\ 0 & 0 & 3400 \end{bmatrix} [\varepsilon_0]$$

with $\varepsilon_0 = 8.8541878128 \times 10^{-12}$ [F m^{-1}].

$$\mathbb{S}_E = \begin{bmatrix} 16.5 & -4.78 & -8.45 & 0 & 0 & 0 \\ -4.78 & 16.5 & -8.45 & 0 & 0 & 0 \\ -8.45 & -8.45 & 20.7 & 0 & 0 & 0 \\ 0 & 0 & 0 & 43.5 & 0 & 0 \\ 0 & 0 & 0 & 0 & 43.5 & 0 \\ 0 & 0 & 0 & 0 & 0 & 42.6 \end{bmatrix} [TPa]^{-1}$$

$$\mathbb{C}_E = \begin{bmatrix} 127.21 & 80.21 & 84.67 & 0 & 0 & 0 \\ 80.21 & 127.21 & 84.67 & 0 & 0 & 0 \\ 84.67 & 84.67 & 117.43 & 0 & 0 & 0 \\ 0 & 0 & 0 & 23.0 & 0 & 0 \\ 0 & 0 & 0 & 0 & 23.0 & 0 \\ 0 & 0 & 0 & 0 & 0 & 23.5 \end{bmatrix} [GPa]$$

5.5.2 CFO elastic properties

The elasticity matrix for cubic CFO is given below (all values from ref. [20]). From these values, the bulk, Young's, and shear moduli, B, E and G, are 81.1, 178.5 and 60.2 GPa,

respectively. Poisson's ratio is $\nu = 0.13$.

$$\mathbb{C}_E = \begin{bmatrix} 186.0 & 28.6 & 28.6 & 0 & 0 & 0 \\ 28.6 & 186.0 & 28.6 & 0 & 0 & 0 \\ 28.6 & 28.6 & 186.0 & 0 & 0 & 0 \\ 0 & 0 & 0 & 50.3 & 0 & 0 \\ 0 & 0 & 0 & 0 & 50.3 & 0 \\ 0 & 0 & 0 & 0 & 0 & 50.3 \end{bmatrix} [GPa]$$

(a)

(b)

(c)

(d)
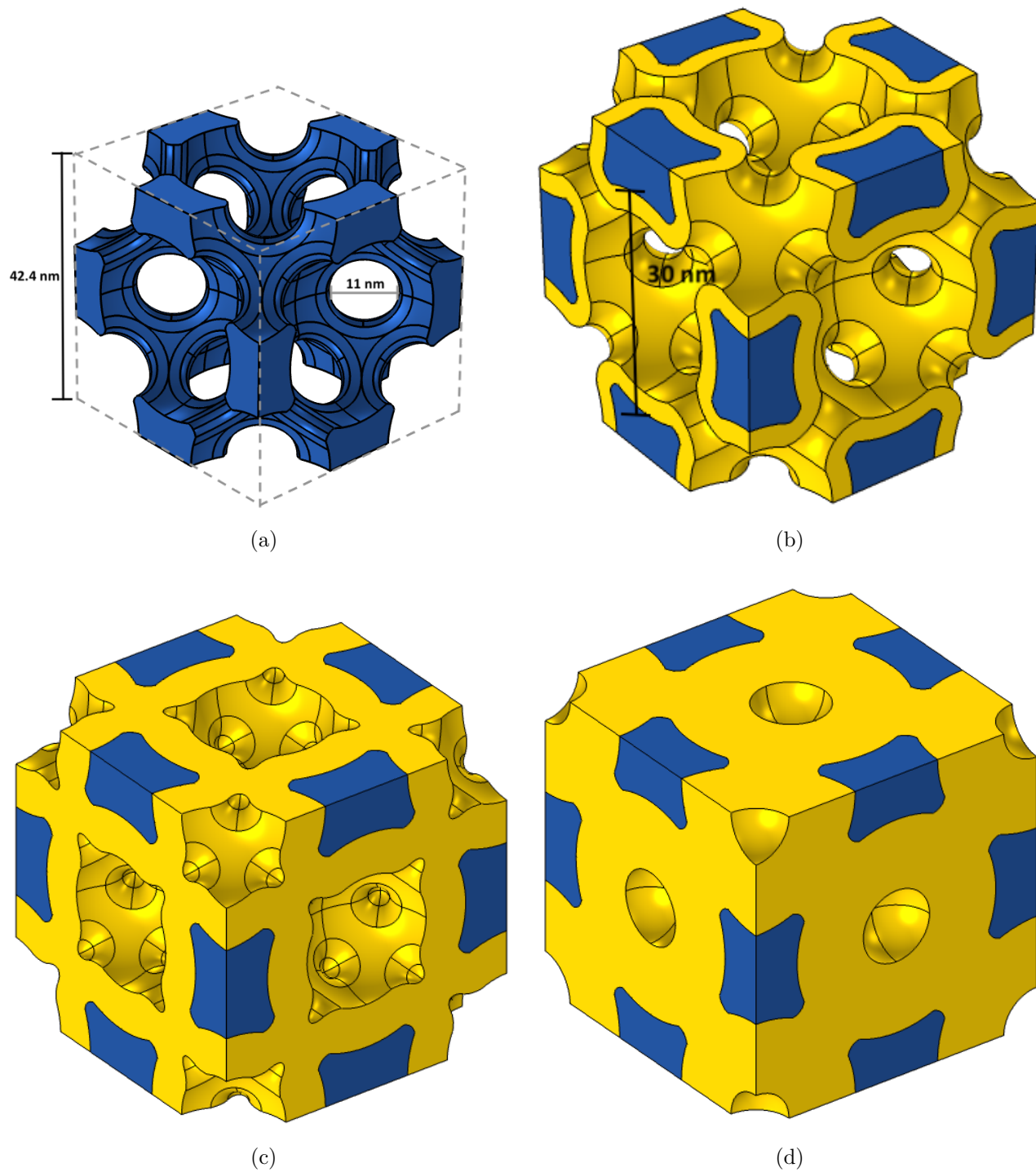
Figure 5.2: (a) CFO building block showing the substructure's pores and ligaments. The PZT-infiltrated structure is shown for (b) 3.0, (c) 6.0, and (d) 10.0 nm thickness.
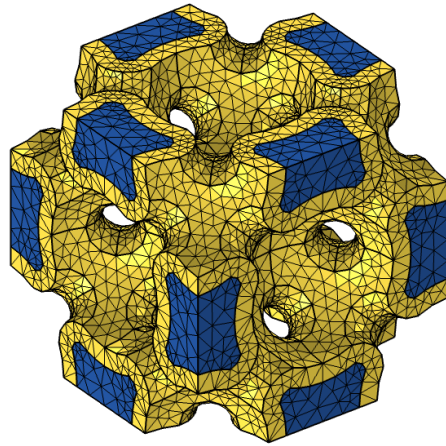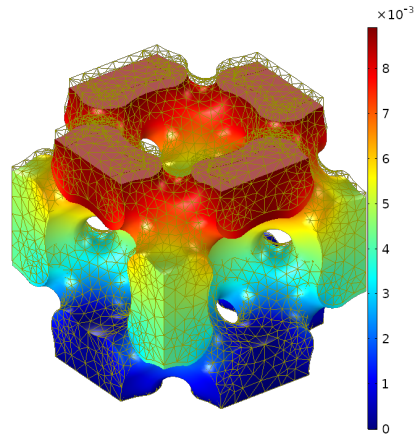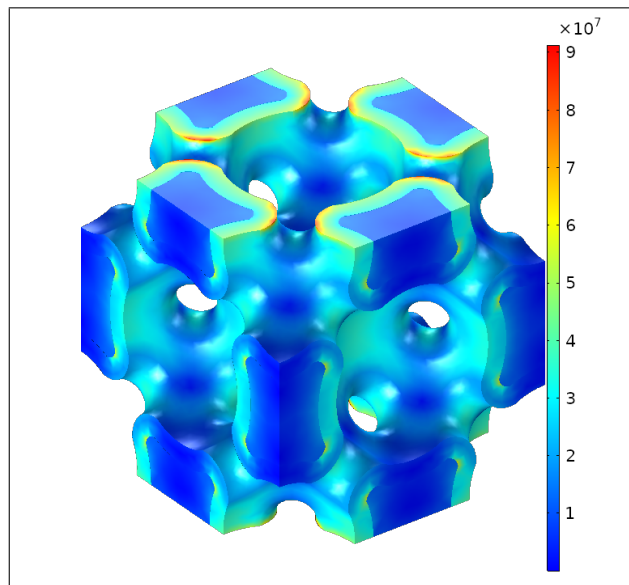
Figure 5.3: View of the undeformed finite element mesh for the 3 nm-thick PZT layer case.

(a)

(b)

Figure 5.4: (a) Deformation (per unit length) and (b) stress fields (in Pa) of the system for $E_z = 1.2\ \text{MV·m}^{-1}$. Color maps are plotted on the undeformed configuration. The wireframe in (a) represents the mesh after deformation.
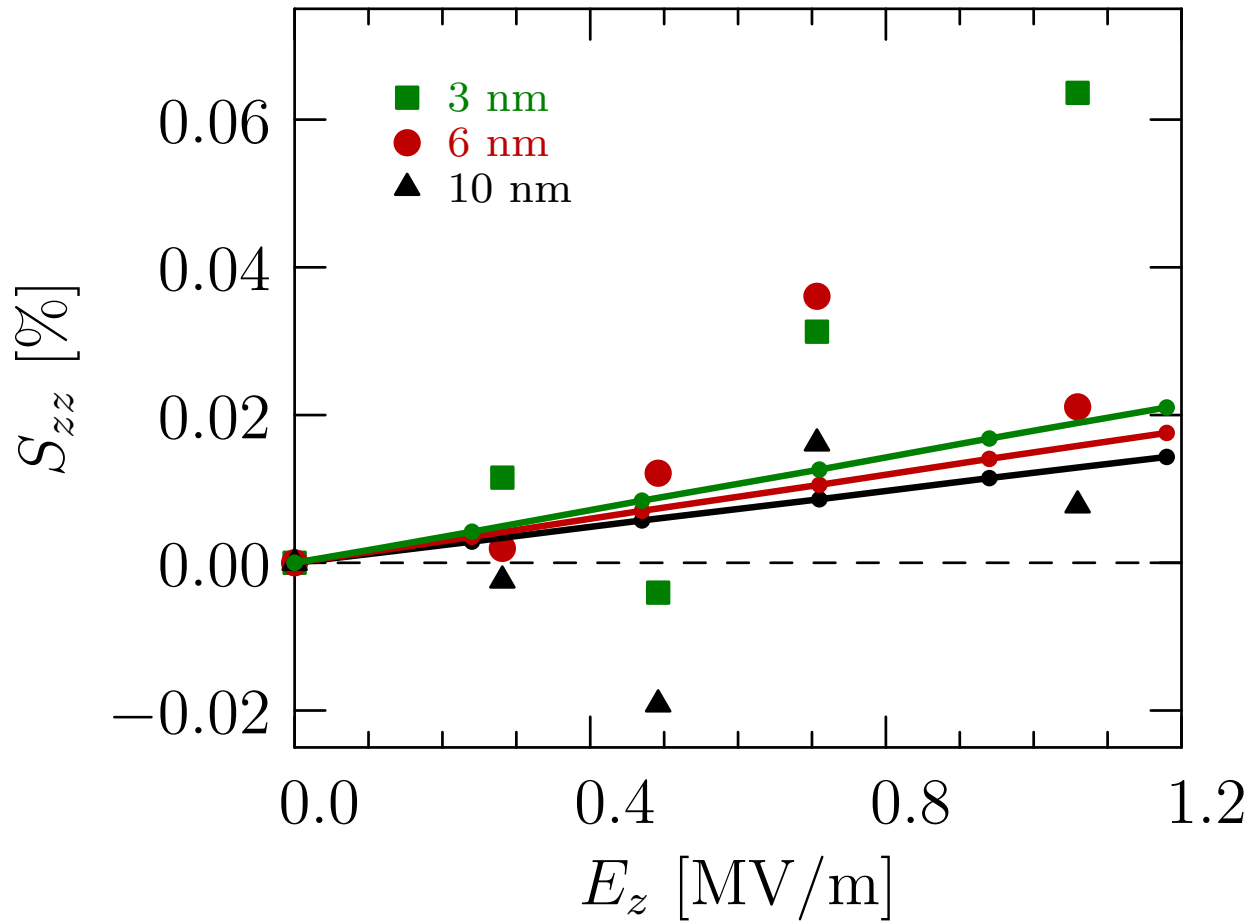
Figure 5.5: Simulation results and experiment data of the relationship between strain (S_{zz} component of $\boldsymbol{S}$) and electric field (E_z component) for the three geometries considered in this work. These results assume perfect linear piezoelectric behavior and ideal CFO/PZT interface bonding.
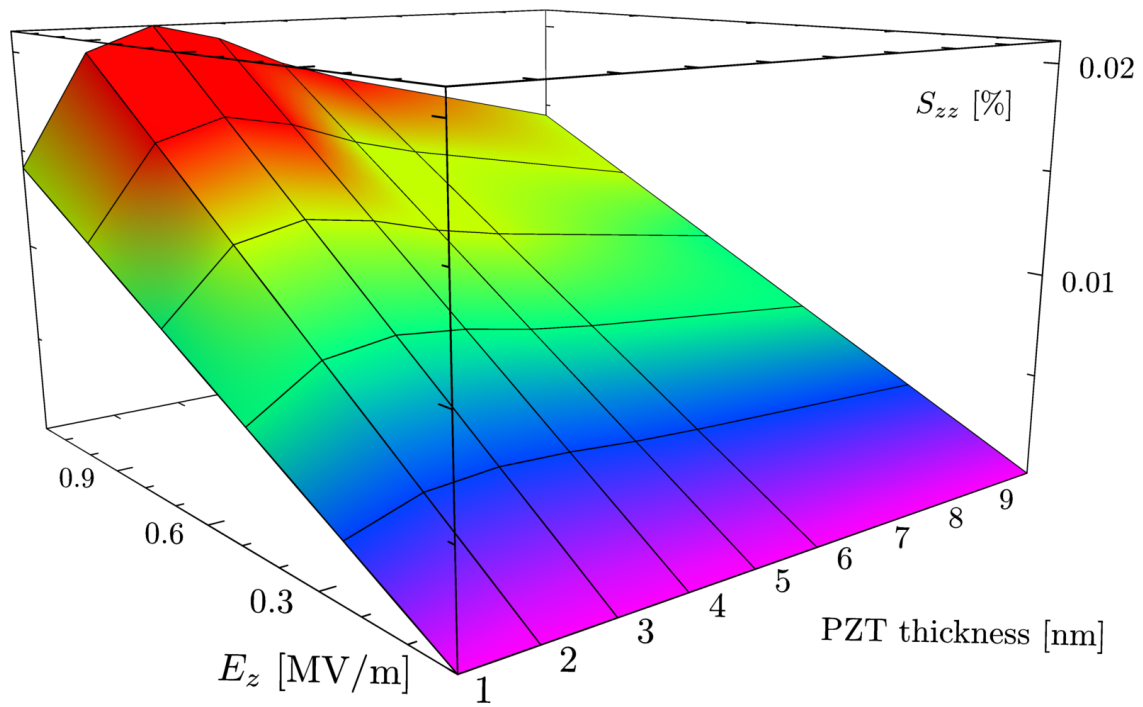
Figure 5.6: Surface plot of the dependence of the device strain on applied electric field and PZT-coating thickness.
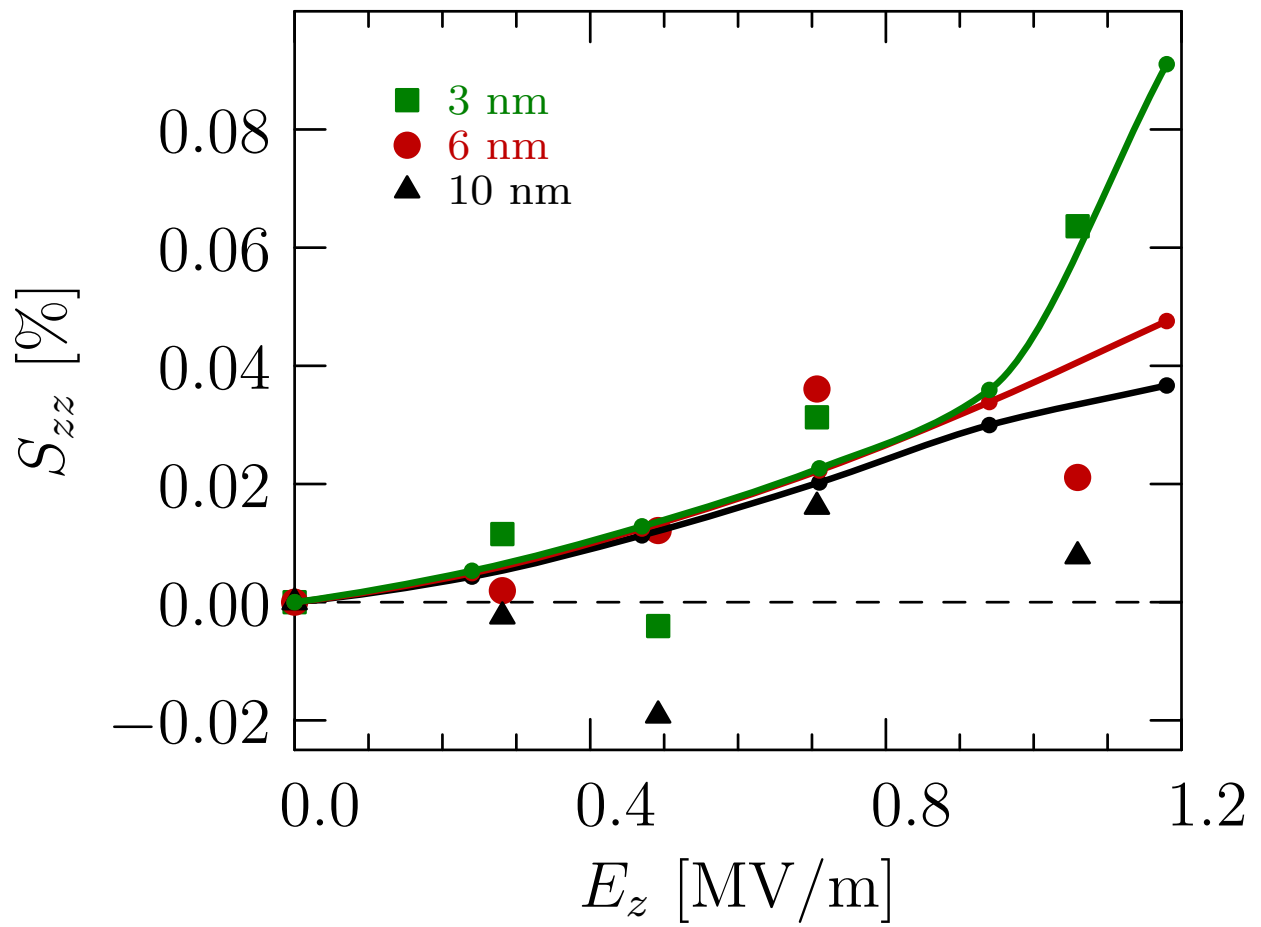
Figure 5.7: Deformation response assuming nonlinear piezoelectric coefficients. Compare these results to Fig. 5.5.
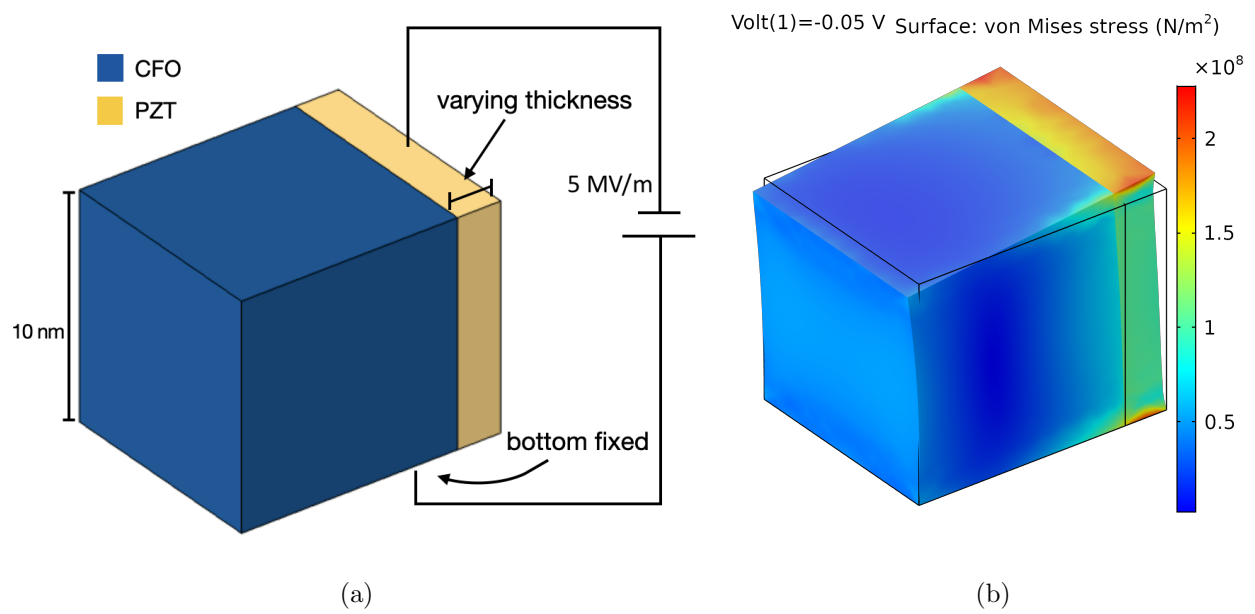
Figure 5.8: (a) Simulation setup for quantifying the effect of shear stresses on the CFO/PZT interface. (b) Deformed geometry and distribution of the Mises stress. The applied voltage differential is 0.5 V ($E_z = 5.0$ MV m^{-1}).
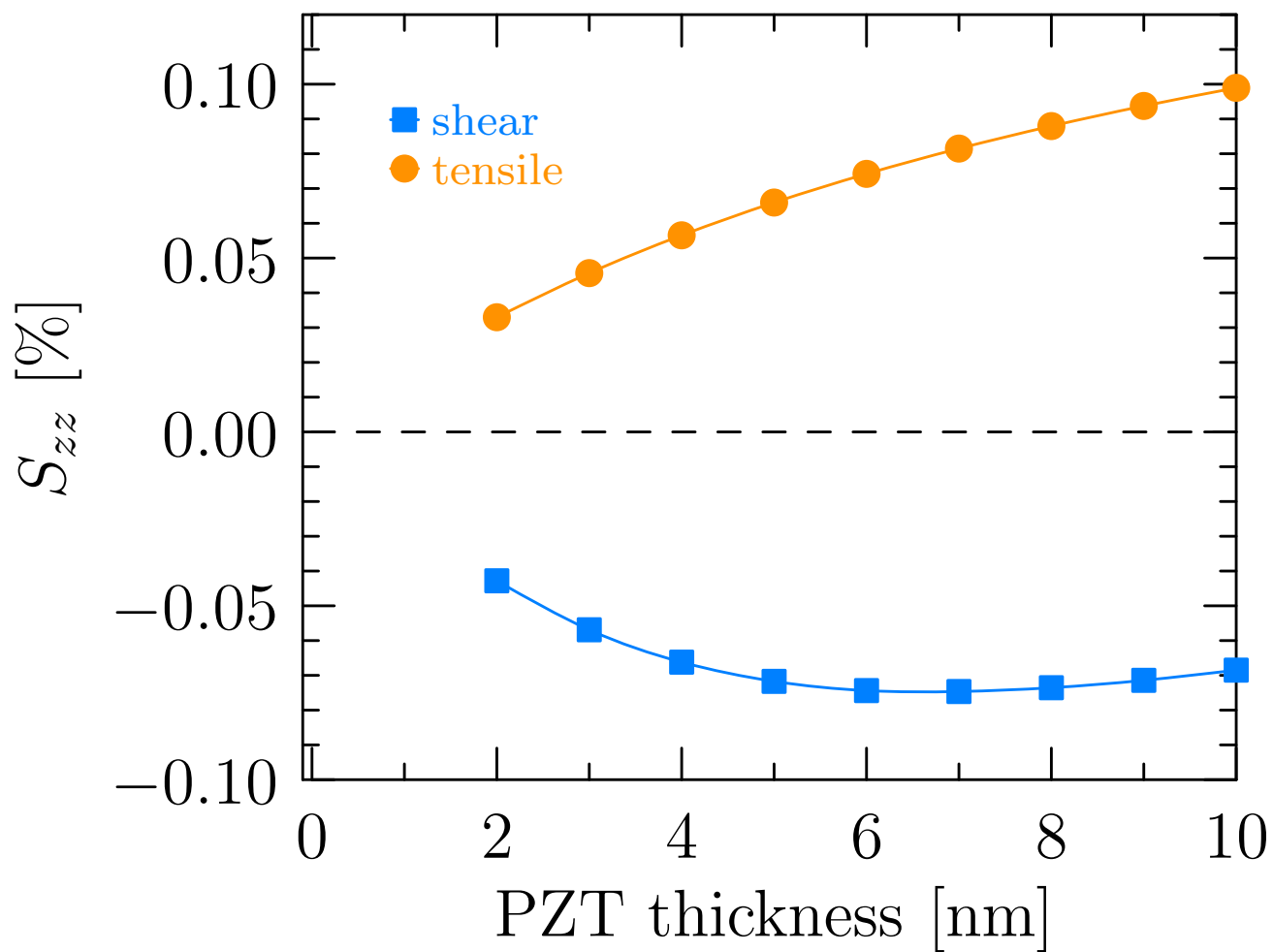
Figure 5.9: Axial strain in the CFO block shown in Figs. 5.8a and 5.10a due to the piezo-electric stimulation of a slab of PZT with varying thickness.
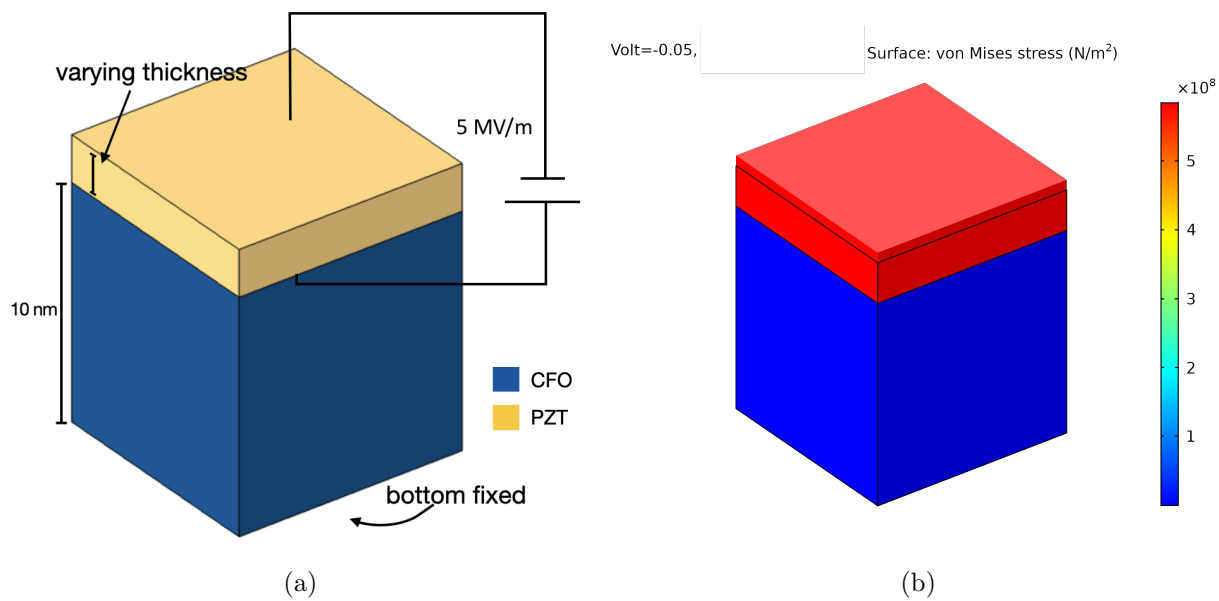
Surface: von Mises stress (N/m²)

Figure 5.10: (a) Simulation setup for quantifying the effect of tensile stresses on the CFO/PZT interface. (b) Deformed geometry and distribution of the Mises stress. $E_z = 5.0$ MV m^{-1}.
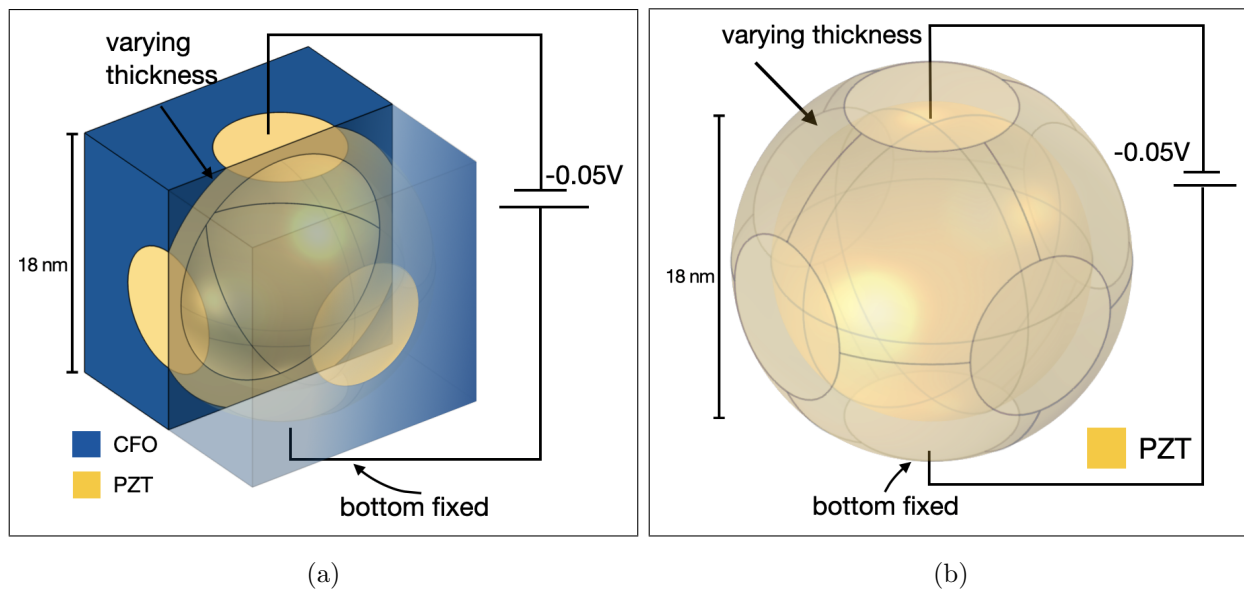

Figure 5.11: (a) A simple CFO+PZO cubic configuration with single pore in the center. (b) Extracted PZT coating.
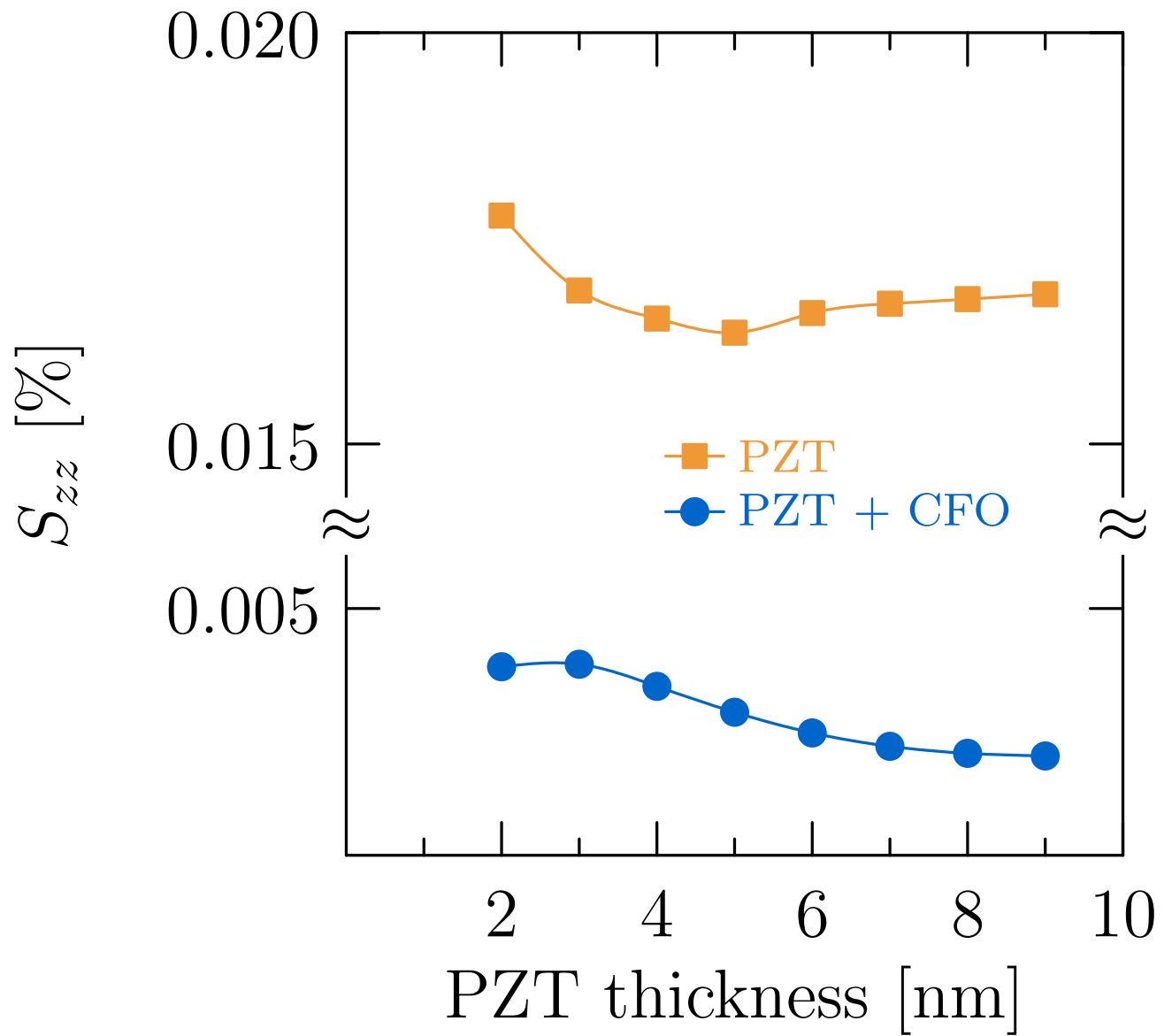
101

Figure 5.12: Axial strain for the geometries in Figs. 5.11a and 5.11b under a 0.05 V voltage differential.

5.6   References

[1] John F Blackburn, Marian Vopsaroiu, and Markys G Cain. Verified finite element simulation of multiferroic structures: Solutions for conducting and insulating systems. *Journal of Applied Physics*, 104(7):074104, 2008.

[2] Abraham N Buditama, Kevin Fitzell, Diana Chien, Christopher Ty Karaba, Shreya K Patel, Hye Yeon Kang, Jane P Chang, and Sarah H Tolbert. Strain transfer in porous multiferroic composites of cofe2o4 and pbzr x ti1- x o3. *Applied Physics Letters*, 120 (19):192902, 2022.

[3] N Cai, J Zhai, C-W Nan, Y Lin, and Z Shi. Dielectric, ferroelectric, magnetic, and magnetoelectric properties of multiferroic laminated composites. *Physical Review B*, 68 (22):224103, 2003.

[4] Diana Chien, Abraham N Buditama, Laura T Schelhas, Hye Yeon Kang, Shauna Robbennolt, Jane P Chang, and Sarah H Tolbert. Tuning magnetoelectric coupling using porosity in multiferroic nanocomposites of ald-grown pb (zr, ti) o3 and templated mesoporous cofe2o4. *Applied Physics Letters*, 109(11):112904, 2016.

[5] Ju H Choi, Feng Zhang, Ya-Chuan Perng, and Jane P Chang. Tailoring the composition of lead zirconate titanate by atomic layer deposition. *Journal of Vacuum Science & Technology B, Nanotechnology and Microelectronics: Materials, Processing, Measurement, and Phenomena*, 31(1):012207, 2013.

[6] Y.-H. Chu, Q. Zhan, L.?W. Martin, M.?P. Cruz, P.-L. Yang, G.?W. Pabst, F. Zavaliche, S.-Y. Yang, J.-X. Zhang, L.-Q. Chen, D.?G. Schlom, I.-N. Lin, T.-B. Wu, and R. Ramesh. Nanoscale domain control in multiferroic bifeo3 thin films. *Advanced Materials*, 18(17):2307–2311, 2006.

[7] Sweden COMSOL AB, Stockholm. Comsol multiphysics. URL `http://www.comsol.com`.

[8] YQ Dai, JM Dai, XW Tang, KJ Zhang, XB Zhu, J Yang, and YP Sun. Thickness effect on the properties of batio3–cofe2o4 multilayer thin films prepared by chemical solution deposition. *Journal of alloys and compounds*, 587:681–687, 2014.

[9] Dragan Damjanovic. Ferroelectric, dielectric and piezoelectric properties of ferroelectric thin films and ceramics. *Reports on Progress in Physics*, 61(9):1267, 1998.

[10] Dragan Damjanovic and Marlyse Demartin. The rayleigh law in piezoelectric ceramics. *Journal of Physics D: Applied Physics*, 29(7):2057, 1996.

[11] DA Hall. Review nonlinearity in piezoelectric ceramics. *Journal of materials science*, 36(19):4575–4601, 2001.

[12] G Helke and Karl Lubitz. Piezoelectric pzt ceramics. In *Piezoelectricity*, pages 89–130. Springer, 2008.

[13] Jacob L Jones, Mark Hoffman, John E Daniels, and Andrew J Studer. Direct measurement of the domain switching contribution to the dynamic piezoelectric response in ferroelectric ceramics. *Applied physics letters*, 89(9):092901, 2006.

[14] Rahul C Kambale, Dae-Yong Jeong, and Jungho Ryu. Current status of magnetoelectric composite thin/thick films. *Advances in Condensed Matter Physics*, 2012, 2012.

[15] Talal M Kamel and G de With. Poling of hard ferroelectric pzt ceramics. *Journal of the European Ceramic Society*, 28(9):1827–1838, 2008.

[16] Chunyue Li, Ruicheng Xu, Rongli Gao, Zhenhua Wang, Gang Chen, Xiaoling Deng, Wei Cai, Chunlin Fu, and Qingting Li. Structure, dielectric, piezoelectric, antiferroelectric and magnetic properties of cofe2o4–pbzr0.52ti0.48o3 composite ceramics. *Materials Chemistry and Physics*, 249:123144, 2020. ISSN 0254-0584. doi: https://doi.org/10.

1016/j.matchemphys.2020.123144. URL `http://www.sciencedirect.com/science/article/pii/S0254058420305174`.

[17] Ahmed R Mahbub, Ariful Haque, and Kartik Ghosh. Fabrication and magnetic characterization of cfo/nio and cfo/nis heterostructures. *Journal of Superconductivity and Novel Magnetism*, 32(9):2857–2864, 2019.

[18] Leszek Malkinski. *Advanced magnetic materials*. BoD–Books on Demand, 2012.

[19] Hengyang Mao, Jiawei Bu, Minghui Qiu, Dong Ding, Xianfu Chen, Hendrik Verweij, and Yiqun Fan. Pzt/ti composite piezoceramic membranes for liquid filtration: Fabrication and self-cleaning properties. *Journal of membrane science*, 581:28–37, 2019.

[20] Fatemeh Mostaghni and Yasaman Abed. Al and peg effect on structural and physico-chemical properties of cofe2o4. *Materials Research*, 20(3):569–575, 2017.

[21] C-W Nan, N Cai, L Liu, J Zhai, Y Ye, and Y Lin. Coupled magnetic–electric properties and critical behavior in multiferroic particulate composites. *Journal of applied physics*, 94(9):5930–5936, 2003.

[22] CW Nan, L Liu, N Cai, and J Zhai. Ye y., yh lin, lj dong, and cx xiong. *Applied Physics Letters*, 81:3831, 2002.

[23] Wei Qin, Beibei Xu, and Shenqiang Ren. An organic approach for nanostructured multiferroics. *Nanoscale*, 7:9122–9132, 2015.

[24] Thomas E Quickel, Van H Le, Torsten Brezesinski, and Sarah H Tolbert. On the correlation between nanoscale structure and magnetic properties in ordered mesoporous cobalt ferrite (cofe2o4) thin films. *Nano letters*, 10(8):2982–2988, 2010.

[25] Z Shi, CW Nan, Jie Zhang, N Cai, and J-F Li. Magnetoelectric effect of pb (zr, ti) o 3 rod arrays in a (tb, dy) fe 2/ epoxy medium. *Applied Physics Letters*, 87(1):012503, 2005.

[26] Zhan Shi, Jing Ma, Yuanhua Lin, and Ce-Wen Nan. Magnetoelectric resonance behavior of simple bilayered pb (zr, ti) o 3–(tb, dy) fe 2/ epoxy composites. *Journal of applied physics*, 101(4):043902, 2007.

[27] Susan Trolier-McKinstry, Nazanin Bassiri Gharb, and Dragan Damjanovic. Piezoelectric nonlinearity due to motion of 180 domain walls in ferroelectric materials at subcoercive fields: a dynamic poling model. *Applied physics letters*, 88(20):202901, 2006.

[28] J Van Suchtelen. Product properties: a new application of composite materials. *Philips Res. Rep*, 27(1):28–37, 1972.

[29] JG Wan, J-M Liu, HLW Chand, CL Choy, GH Wang, and CW Nan. Giant magneto-electric effect of a hybrid of magnetostrictive and piezoelectric composites. *Journal of applied physics*, 93(12):9916–9919, 2003.

[30] KF Wang, J-M Liu, and ZF Ren. Multiferroicity: the coupling between magnetic and polarization orders. *Advances in Physics*, 58(4):321–448, 2009.

[31] Ruifeng Wang and Ernian Pan. Three-dimensional modeling of functionally graded multiferroic composites. *Mechanics of Advanced Materials and Structures*, 18(1):68–76, 2011.

[32] Leland Wilkinson. Systat. *Wiley Interdisciplinary Reviews: Computational Statistics*, 2(2):256–257, 2010.

[33] Junxiang Yao, Xiao Song, Xingsen Gao, Guo Tian, Peilian Li, Hua Fan, Zhifeng Huang, Wenda Yang, Deyang Chen, Zhen Fan, et al. Electrically driven reversible magnetic rotation in nanoscale multiferroic heterostructures. *ACS nano*, 12(7):6767–6776, 2018.

[34] Haimei Zheng, J Wang, SE Lofland, Z Ma, Ly Mohaddes-Ardabili, T Zhao, L Salamanca-Riba, SR Shinde, SB Ogale, Feiming Bai, et al. Multiferroic batio3-cofe2o4 nanostructures. *Science*, 303(5658):661–663, 2004.